STUDYING THE EVOLUTION OF POLYDISPERSE DROPLET SIZE DISTRIBUTIONS USING LARGE EDDY SIMULATIONS

by

Aditya Kandaswamy Aiyer

A dissertation submitted to The Johns Hopkins University in conformity with the requirements for the degree of Doctor of Philosophy

Baltimore, Maryland

August 2020

Abstract

We develop a Large Eddy Simulation (LES) model that can predict the turbulent transport and evolution of droplet size distributions, for a specific subset of applications in which the dispersed phase can be assumed to consist of spherical droplets, at low volume fraction. We use a population dynamics model for polydisperse droplets specifically adapted to a LES framework including a model for droplet breakup due to turbulence, neglecting coalescence consistent with the assumed small dispersed phase volume fractions. Existing breakup models assume the scale of droplet–eddy collision to be in the inertial range of turbulence. In order to also model smaller droplets comparable to or smaller than the Kolmogorov scale we extend the breakup kernels using a structure function model that smoothly transitions from the inertial to the viscous range. The model includes a dimensionless coefficient that is fitted by comparing predictions in a one-dimensional version of the model with a laboratory experiment of oil droplet breakup below breaking waves. The LES model is applied to a three-dimensional turbulent jet subjected to a uniform cross-

ABSTRACT

flow and droplet size distributions downstream of the injection are compared with experimental data with good agreement. The LES results also enable us to quantify size distribution variability. We find that the probability distribution functions of key quantities such as the total surface area and the Sauter mean diameter of oil droplets are highly variable, some displaying strong non-Gaussian intermittent behaviour. Further applications with smaller nozzles require an inlet conditions for coarse LES. We develop a hybrid approach where the inlet condition is prescribed using a one dimensional (1D) parcel model that accounts for the evolution of the dispersed phase along the jet centerline due to the combined effects of advection, radial turbulent transport and droplet breakup. We examine the statistics of the velocity field and the concentration profiles of the polydisperse oil droplet plumes for two droplet Weber numbers. We find that the centerline decay rate of the droplet concentration is modified in the breakup dominated zone. Additionally due to trajectory crossing effects the dispersion of larger droplets is suppressed.

Primary Reader and Advisor: Charles Meneveau

Secondary Readers: Rui Ni and Harihar Rajaram

Acknowledgments

I am deeply indebted to innumerable people who have extended their support throughout my doctoral journey. The successful completion of my dissertation would not have been possible without the help and support of my advisor, Professor Charles Meneveau. I am grateful for his guidance throughout this project and encouragement to develop independent critical thinking. Thank you to Professors Di Yang and Marcelo Chamecki for their kindness and technical guidance during our weekly Skype meetings. Many thanks to Professors Dennice Gayme and Rui Ni for enriching my Ph.D. experience with many engaging technical discussions and to many wonderful faculty who have enhanced my time at Hopkins, to name a few, Professors Joseph Katz, Gretar Tryggvasson, Yannis Kevrekides, Rajat Mittal, and others. I must also thank Professor Harihar Rajaram for serving on my dissertation and GBO committees and Professors Ananad Gnanadesikan and Thomas Haine for serving on my GBO committee

I am grateful for the never ending supply of love and support from my

ACKNOWLEDGMENTS

parents, Gayathri and Kandaswamy, my sister Isha, and my brother-in-law Ananth. To my friends and colleagues at Hopkins, Ben, Carl, Gen, Ghanesh, Karthik, Mitchell, Perry, , Srivaths, Samvit, Xiaowei, Kristofer, Jibu, Chang, Mengze, Shantanu, Subhra, Karuna, Jose and Harsh for engaging lunch conversations and unnecessarily long coffee hours. Special thanks to Soham, Ayush, Ikbal, Prashant, Likitha, Ankitha, Saurov, Disha, Sapna, Shriniket, Gaurav, Raunak, Nikita, Kanika, Jeh and numerous others for their constant support and friendship during my stay in Baltimore.

Contents

Abstract ii

Acknowledgments iv

List of Tables x

List of Figures xi

1 Introduction 1

1.1 Population Balance Equation 4

1.2 Droplet Breakup Models 7

1.3 Numerical Modelling of Turbulent Polydisperse Systems 10

1.4 Experimental Data for Model Validation 14

1.5 Outline 15

2 Droplet Breakup Model 18

2.1 Breakup Model Formulation 20

2.1.1 Model for the Breakup Probability. 21

2.1.2 Model for Breakup Frequency 24

2.2 Determining the Model Constant 32

2.2.1 Wave Breaking Experiment 32

2.2.2 A Column Model for Droplet Size Distributions 33

2.3 Droplet Breakup Model Validation 41

2.4 Conclusions 46

3 Large Eddy Simulations : Methods **47**

3.1 LES Governing Equations 48

3.1.1 Filtered Navier-Stokes Equations 48

3.1.2 Filtered Concentration Equation 50

3.2 Numerical Treatment 54

3.3 Generating a Turbulent Jet via Body Forcing 60

3.4 Conclusions 66

4 LES of Polydisperse Droplets in a Jet-in-crossflow **68**

4.1 Simulation Setup 69

4.2 Instantaneous and Mean Concentration Distributions 75

4.3 Relative Droplet Size Distributions 77

4.4 Variability of Droplet Size Distribution 88

4.5 Conclusions 94

5 Hybrid ODE-LES Approach : Model Development **96**

5.1 Introduction 96

5.2 One-Dimensional ODE Model 98

5.2.1 Model Development 99

5.2.2 Model Validation 105

5.2.3 Inlet Condition for Large Eddy Simulations 111

5.3 Conclusions 113

6 Hybrid ODE-LES Approach Applied to a Turbulent Round Jet **115**

6.1 Introduction 115

6.2 Simulation Setup 116

6.3 Results 119

6.3.1 Jet Velocity and Total Concentration Field 119

6.3.2 Droplet Size Distribution 123

6.3.3 Temporal Variability of Size Distribution 128

6.4 Conclusions 134

7 Size Based Differential Droplet Dispersion **136**

7.1 Particle Trajectory Crossing Effect 137

7.2 Results 139

7.3 Conclusions 143

8 Summary and Future Work **145**

8.1 Directions for Future Work 148

A Empirical Modelling of the Breakup Frequency Integral **151**

Vita **181**

List of Tables

2.1 Dispersed fluid properties. 43

4.1 Physical properties of fluids used in the simulation. 75
4.2 Simulation parameters. 75

5.1 Summary of Experimental conditions for the different cases. . . . 111

6.1 Simulation parameters. 117

A.1 $\Gamma = 10.5$. 154
A.2 $\Gamma = 5.45$. 155

List of Figures

1.1 Fate and transport of oil from an underwater blowout 4

2.1 Normalized eddy fluctuation velocity calculated using inertial range scaling (- - -) and using a scaling valid for the viscous and inertial range of scales (—). LES filter scale is denoted by the blue dashed line. 26

2.2 Left: Sketch of the wave breaking experiment of Li et al.[60]. Right: schematic dependence of $\overline{n}_i(z,t)$ on time and height for a particular droplet size, starting from a step-function initial condition that is assumed to be well mixed initially down to a depth of 13 cm below the surface and having zero concentration below. At increasing times, turbulent diffusion smooths the step and droplets rise towards the surface at different speeds depending on their size. The dotted horizontal line at $z = -11.1$ cm is where the experimental data is available. 33

2.3 Time evolution of the droplet size distribution for two values of K^*, at the measurement location. The symbols correspond to the experimental data, $t = 5$ s (–●–) represents the initial condition where experiment and column model are matched, $t = 15$ s (∗), $t = 35$ s (□), $t = 55$ s (◆), while the lines correspond to the column model, $t = 15$ s (- - -), $t = 35$ s (-·-·-) and $t = 55$ s (· · ·). The green stars (★) in (a) correspond to the size distribution at $t = 55$ s using $N_d = 15$ bins 36

2.4 Average square error between predicted and measured logarithms of number densities averaged over 3 times during the evolution, at the measurement position, as a function of the breakup constant K^* assumed in the model. 38

2.5 Time evolution of the droplet size distribution for $K^* = 0.2$. (*a*) uses an inertial scaling of u_e. In (*b*) we plot the effect of using a normal distribution proposed by Coulaloglou and Tavlarides[23]. The symbols correspond to the experimental data, $t = 5$ s (–●–) represents the initial condition where experiment and column model are matched, $t = 15$ s (∗) , $t = 35$ s (□), $t = 55$ s (◆), while the lines correspond to the column model, $t = 15$ s (- - -), $t = 35$ s (-·-·-) and $t = 55$ s (· · ·). 41

2.6 We depict the effect of changing the maximum diameter size on the size distribution and breakage frequency. In (*a*) the symbols correspond to the experimental data, $t = 5$ s (–●–) represents the initial condition where experiment and column model are matched, $t = 15$ s (∗) , $t = 35$ s (□), $t = 55$ s (◆), while the lines correspond to the column model using $K^* = 0.2$, $t = 15$ s (- - -), $t = 35$ s (-·-·-) and $t = 55$ s (· · ·). The green dashed line (- - -) corresponds to the case where $d_{e,max} = 1.2d_i$ and $K^* = 0.1$ was used to calculate $g(d_i)$. In (*b*) we compare the resulting breakup frequency for the two cases, $d_{e,max} = 1.2d_i$(- - -) and $d_{e,max} = d_i$(—). 42

2.7 Evolution of the $N(d_{max})$ with downstream distance for the four different oils in 2.1. The symbols correspond to the experimental data of the different oils, 50 cSt Silicone oil (○), Olive oil (◇), 10 cSt Silicone oil (▫) and Heptane (∗). The different lines correspond to the model, 50 cSt Silicone oil (—), Olive oil (-·-·-), 10 cSt Silicone oil (· · ·) and Heptane (- - -) with $K^* = 0.2$. Also shown are the model for Heptane (–○–) with $K^* = 0.1$ and 10 cSt Silicone Oil (·○·) with $K^* = 0.15$. 45

3.1 Primitive variables with respect to staggered mesh. Left : Variables on the pseudo-specral grid. Right : Finite volume grid. (Adapted from Chamecki et al.[14]. 55

3.2 Downstream variation of half width of the jet (○, right axis) and the evolution of the inverse of the averaged centerline velocity (□, left axis) from LES. The linear fit to the data is depicted by the black dashed line (- - -). 64

3.3 Downstream variation of half width of the jet (○, right axis) and the evolution of the inverse of the averaged centerline velocity (□, left axis) from LES. The linear fit to the data is depicted by the black dashed line (- - -). 64

3.4 Downstream variation of half width of the jet (○, right axis) and the evolution of the inverse of the averaged centerline velocity (□, left axis) from LES. The linear fit to the data is depicted by the black dashed line (- - -). 66

4.1 Sketch of the simulation domain and dimensions. 71
4.2 Sketch depicting the nozzle placement in LES (at vertical position $z_m = 54$ mm downstream of the experimental nozzle), the virtual origin of the experiment (assumed to be at $z_0 = 16$ mm $= 4d_{expt}$ downstream of the nozzle), and the measurement location (at a height of $z_{ML} = 470$ mm above the experimental nozzle position - in the experiment with cross-flow, there is additional displacement in the horizontal direction). 72
4.3 Volume rendering of an instantaneous snapshot of the $20\mu\ m$ droplet plume with the $1\ mm$ droplets shown as solid spheres. . . 76
4.4 Contour plots of instantaneous concentration fields at the midplane of the jet. The concentration is plotted in logarithmic scale. (a) is the concentration of the droplet of size $1000\ \mu$m, (b) for $d = 432\ \mu$m, (c) for $d = 107\ \mu$m, and (d) for $d = 20\ \mu$m. 76
4.5 Time averaged concentration fields at the midplane of the jet plotted in logarithmic scale. Panel (a) is the concentration of droplets of size $1000\ \mu$m, (b) shows the concentration field for $d = 432\ \mu$m, (c) shows the concentration field for $d = 107\ \mu$m, and (d) shows the concentration field for $d = 20\ \mu$m. 78
4.6 Contour plot of the logarithm of the averaged total volume concentration of oil showing the measurement location at $x = 0.76$ m and $x = 1.3$ m. 82
4.7 Comparison of LES model at $x = 0.76$ m for mono-dispersed injection (-o-) and bi-dispersed injection (-o·), and experimental data from[72] measured at the corresponding time ($*$). Left panel: Relative size distribution from LES, Right panel: Relative volume distribution. 82
4.8 Comparison of LES model at $x = 1.3$ m (-o-) , and experimental data from[72] measured at the corresponding time ($*$). Left panel: Relative size distribution from LES, Right panel: Relative volume distribution. 83
4.9 Comparison of LES model averaged over a spatial window of $x = 0.76$–1.66 m (-o-) , and total averaged experimental data from[72] ($*$). Left panel: Relative size distribution from LES, Right panel: Relative volume distribution. 83
4.10 Left panel: evolution of centroid of various droplet plumes. Right panel: logarithm of the concentration profile as function of height at a downstream distance, $x = 1$ m and transverse position $y = 0.385$ m. The lines are $d = 1000\ \mu$m(—o—), $d = 432\ \mu$m(-·-), $d = 107\ \mu$m(- - -) and $d = 20\ \mu$m(——). 85

4.11 Average d_{32} diameter as function of downstream distance x at various plume heights. The lines correspond to $z = 0.55$ m (—), $z = 0.50$ m(- - -) and $z = 0.45$ m(· · ·) 87
4.12 Representative time signals (left panels) and histograms (right panels) for the Sauter mean diameter, d_{32} at two downstream locations on the centerline. Dotted lines denote mean values. 88
4.13 Representative time signals (left panels) and histograms (right panels) of $\log_{10}(\epsilon)$ at two downstream locations on the centerline. ϵ is in m^2/s^3. Dotted lines denote mean value. 90
4.14 Representative time signals (left panels) and histograms (right panels) of total surface area of the oil per cubic meter of fluid at two downstream locations on the centerline. A_{tot} is in m^2/m^3. Dotted lines denote mean values. 91
4.15 Representative time signals (left panels) and histograms (right panels) of $\log_{10}(\tilde{S}_{b,i}/\tilde{n}_i)$ for $d = 20$ μm plotted at two downstream locations of the plume at a fixed height. The values of $\tilde{S}_{b,i}/\tilde{n}_i$ are given in $1/s$. Dotted lines denote mean values. 92
4.16 Time history of $\tilde{S}_{b,i}$ normalized by concentration for different droplet sizes at $z = 0.56$ m on the centerline. (a) and (b) represent the droplet of size 1000 μm at two different x locations, (c) is the time history for $d = 432$ μm and (d) is for $d = 20$ μm. Dotted lines denote mean values. 93

5.1 Schematic diagram of the hybrid ODE-LES modeling approach: Between the nozzle and the end of the 1D ODE model region, the size distribution is obtained by integrating a 1D ordinary differential equation for the centerline concentrations. The results are used as inflow concentrations for the Eulerian-Eulerian LES further downstream. 98
5.2 (a) Relative number density distribution of Expt. 1 (□) and Expt. 2 (○) at $z = 2m$. The y-axis is scaled differently for visualization purposes. The right axis depicts the size distribution from Expt. 1 while the left axis depicts the size distribution from Expt. 2. The dashed line (- - -) denotes the fit of the tail of the distribution with $F_1(d) = A_2 d^{-4}$ and $F_2(d) = A_1 d^{-6}$. The fitted constants are $A_1 = 1.28 \times 10^{-6}$ and $A_2 = 6.76 \times 10^{-14}$, (b) Comparison of number density distribution from the 1D ODE model for Expt 1. (–□–) and Expt. 2 (–●–) and corresponding experimental data (□, ○) at measurement location. 109

5.3 a Parameterized jet centerline velocity (- - -) and dissipation (—), used as an input to the 1D ODE model. b Scaled centerline number concentration, n_2 ; $d = 18.5$ μm (—), $5 \times n_7$; $d = 76$ μm (- - -), $10 \times n_9$; $d = 134$ μm(—) and $10 \times n_{12}$; $d = 313$ μm(- - -) as a function of downstream distance. The initial conditions for LES are determined by the concentration values at $z = 10D_J$ depicted by the dashed line (- - -). 113

6.1 (a) Sketch of the simulation setup. Volume rendering of the instantaneous 14 μm diameter droplet concentration with the 1000 μm droplets visualized as dots placed randomly with density proportional to its concentration field. (b) Inlet distribution, n_i (number of droplets per m^3 of fluid) for LES determined by the one-dimensional model, ... 116

6.2 a Averaged axial velocity profiles as function of normalized radial distance, b Averaged concentration profiles at $z/D_J = 135$ (△), $z/D_J = 168$ (○), $z/D_J = 211$ (□) and $z/D_J = 243$ (▷) as a function of self similarity variable $r/r_{1/2}$. The dashed line (- -) denotes the DNS data[64] and the solid line (—) represents the analytical constant eddy-viscosity solution. 120

6.3 Radial distributions of concentration fluctuation root-mean-square at $z/D_J = 135$ (△), $z/D_J = 168$ (○), $z/D_J = 211$ (□) and $z/D_J = 243$ (▷)), normalized by centerline mean concentration, as a function of $r/r_{1/2}$. 122

6.4 Instantaneous snapshots of concentration fields at the midplane of the jet plotted in logarithmic scale for different droplet sizes. The domain has been cropped at $z/D_J = 500$ for visualization purposes. 122

6.5 Evolution of Sauter mean diameter, D_{32} as a function of downstream distance from the nozzle for SIM 1 (□) and SIM 2 (○). The D_{32} curves from the ODE model for both cases are depicted by a solid line. 123

6.6 (a) Comparison of centerline droplet size distribution from experimental data (□, right axis) at $z/D_J = 666$ with extended LES results (also right axis, - - -). The latter is obtained by solving Eq. (5.15) using the LES data as inlet condition at $z/D_J = 333$ (left axis) as initial condition (these LES data at $z/D_J = 333$ are shown by the top - - -line). Error bars display the r.m.s. at $z/D_J = 333$ due to turbulence. The 1D ODE model applied between $z/D_J = 2$ to 333 is depicted by (○, left axis). (b) Comparison of droplet size distribution from SIM 2 (····) with 1D ODE model (○) and SIM 1 size distribution (- - -) at $z/D_J = 333$. 126

6.7 Decay of centerline concentration of different droplet sizes as a function of downstream distance from the nozzle. The symbols represent the LES evolution and the corresponding color coded dashed lines are the results from the 1D ODE model model for (a) SIM 1 and (b) SIM 2. The symbols are $d = 14$ μm (△), $d = 100$ μm (○), $d = 550$ μm (□) and $d = 3$ mm (▷). The total concentration from SIM 1 and SIM 2 is represented by the black dashed line. . 126

6.8 Evolution of the inverse centerline concentration for SIM 1(open symbols) and SIM 2 (closed symbols). The symbols are $d = 14$ μm (△), $d = 100$ μm (○), $d = 550$ μm (□) and $d = 3$ mm (▷). 127

6.9 The top panel depicts the radial distribution of the averaged Sauter mean diameter, D_{32} normalized by its centerline value while the bottom panel depicts the normalized standard deviation at $z/D_J = 135$ (- - -), $z/D_J = 168m$ (- - -), $z/D_J = 211$ (····), $z/D_J = 243$ (-·-) for (a) SIM 1 and (b) SIM 2. 129

6.10 The top panel depicts the radial distribution of the averaged total surface area, $\widetilde{A}$ normalized by its centerline value while the bottom panel depicts the normalized standard deviation at $z/D_J = 135$ (—), $z/D_J = 168m$ (- - -), $z/D_J = 211$ (····), $z/D_J = 243$ (-·-) for (a) SIM 1 and (b) SIM 2.. 130

6.11 Evolution of the inverse breakup time scale with downstream distance for (a) SIM 1 and (b) SIM 2. The lines are $d = 14$ μm (—), $d = 100$ μm (- - -), $d = 550$ μm (····) and $d = 2261$ μm (-·-) and $d = 3000$ μm (- -). 131

6.12 The top panel depicts the radial distribution of the averaged inverse breakup timescale, $\tilde{t}_i = \widetilde{S}_{b,i}/\tilde{n}_i$ normalized by its centerline value while the bottom panel depicts the normalized standard deviation for (a) SIM 1 and (b) SIM 2.The lines are $d = 14$ μm (—), $d = 100$ μm (- - -), $d = 550$ μm (-·-) and $d = 3000$ μm (-··-) at $z/D_J = 70$. 132

7.1 Normalized radial concentration profiles for different droplet sizes at $z/D_J = 160$. The symbols are $d = 14$ μm (△), $d = 236$ μm (○), $d = 730$ μm (□) and $d = 3$ mm (▷). 139

7.2 (a) Evolution of concentration half width as a function of downstream distance from the nozzle. The symbols are $d = 14$ μm (△), $d = 236$ μm (○), $d = 730$ μm (□) and $d = 3$ mm (▷), (*b*) Spread rate of different droplet plumes as a function of diameter. 141

7.3 Ratio of transverse particle to fluid dispersion coefficient calculated using equation (7.3). The symbols are $d = 14$ μm (△), $d = 236$ μm (○), $d = 730$ μm (□) and $d = 3$ mm (▷). 141

7.4 Spread rate calculated using LES concentration field (□) and using modified Schmidt number (○) defined by equation (7.3). . . . 143

A.1 Scaled breakup frequency as a function of Reynolds number for different Ohnesorge numbers. The fit is represented by the dashed lines whereas the numerically computed integral are the various symbols for $\Gamma = 10.5$. 153

A.2 Scaled breakup frequency as a function of Reynolds number for different Ohnesorge numbers. The fit is represented by the dashed lines whereas the numerically computed integral are the various symbols for $\Gamma = 5.45$. 154

A.3 Scaled breakup frequency as a function of droplet Reynolds number for different Ohnesorge numbers. The fit is represented by the dashed lines computed by interpolating between $\Gamma_1 = 5.45$ and $\Gamma_2 = 10.5$. The symbols represent the numerically computed integral for $\Gamma = 8$. 155

Chapter 1

Introduction

A globally increasing demand for energy has led to increased offshore deep-sea extraction of oil and gas. According to the U.S energy information administration (EIA) offshore production accounts for about 30% of the global crude oil output. This increased demand comes with the associated risk of an accidental deep-sea blowout. A recent example of such a blowout is the BP Gulf of Mexico Oil spill, considered to be the largest marine oil spill in the history of the petroleum industry. The oil flowed from the bottom of the sea for 87 days, releasing 800 million litres of oil and forming an oil slick which covered an area of up to 175,000 km^2[77]. The spill had a devastating environmental and ecological impact affecting more than 2100km of shoreline[8]. Although preventing a spill is the primary goal, in the event of a blowout strategies for remediation that address both the surface and subsurface conditions are essential. Accurate

modelling and prediction of the transport of the oil considering factors such as breakup, coalescence, dissolution and turbulent dispersion is necessary.

The ejected oil jet undergoes breakup into polydisperse droplet plumes as it flows towards the ocean surface (see Figure 1.1). On ejection from the well head, oil and gas rises through the ocean with the initial momentum generated by the pressure at blowout location. The further rise of the droplets towards the surface is governed by buoyancy. The droplet plume grows due to entrainment of ambient water. The subsurface stable stratification results in a reduction in buoyancy forming horizontal intrusion layers (shown in Figure 1.1). Only oil droplets with large enough buoyancy continue to rise. In the Gulf of Mexico oil spill, it was found that droplets with diameter $60 - 80\ \mu m$ rose slowly to the surface while being dispersed by the subsurface flow. Larger droplets ($d > 300\ \mu m$) directly reached the surface with minimal dispersion[76]. After the initial jet ejection phase the subsequent fate of the oil is governed by the generated polydisperse oil plumes. Understanding the evolution of the droplet size distribution is critical in predicting the subsequent transport of oil necessary in developing remedial strategies[77,75]. The size of oil droplets affects their rise velocity and can influence the entire plume's transport characteristics in the ocean[18]. Moreover, smaller droplets are influenced by the ocean turbulence and are more horizontally dispersed. A particular remedial strategy that has been used is to apply dispersants to the oil at the well head and at the surface to

break larger droplets into small ones. Dispersants reduce the surface tension of the oil thereby increasing the frequency of droplet breakup. Understanding mechanisms such as breakup and coalescence is critical in characterizing the complete evolution of the droplets.

Information regarding size distributions of droplets is needed in many other applications. In engineering systems, such as atomization, detailed information of the droplet size is of great importance in the design and application of spray systems[71]. Of much interest during the Covid-19 epidemic, the size distribution of drops generated by coughing affects their residence time in the air as well as the ability of masks to prevent their transmission[70]. The particle size distribution also plays a significant role in environmental systems. In clouds, the particle size distribution affects cloud dynamics and the thermodynamic characteristics of the system[63][41]. Bubbles in the open ocean play an important role in upper ocean physical processes including marine aerosol production, optical scattering and air-sea heat and moisture transfer[25]. Accurate characterization of the dispersed phase size distribution is thus crucial in the context of numerous natural and engineering multiphase flow processes.

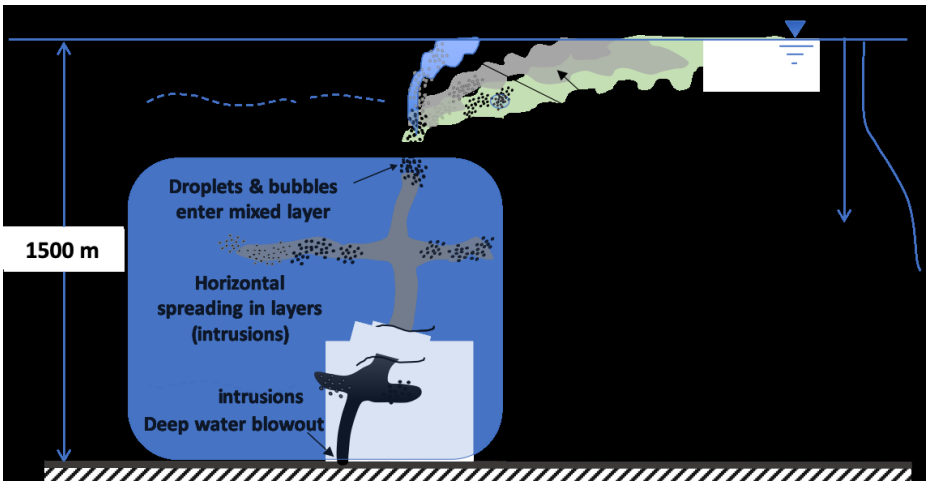

Figure 1.1: Fate and transport of oil from an underwater blowout

1.1 Population Balance Equation

Population balances can be regarded as a subject with a very rich literature that has its origins in the Boltzmann equation presented more than a century ago[98]. Initially formulated to study aggregation processes[95], Population balance equations (PBE's) have been extended by numerous researchers[39,85,83] to include additional phenomena such as breakup, coalescence, nucleation and condensation. PBE's have been used to model a wide range applications including aerobic fermentation, combustion, crystallization, chemical reactors and oil spill modelling. The population balance equation is a transport equation that describes the temporal and spatial rate of change of the number density in a dispersed two-phase flow. The number density function $f(d, \boldsymbol{x}, t)\mathrm{d}(d)\mathrm{d}\boldsymbol{x}\mathrm{d}t$ represents the number of particles of diameter d, about an interval $\mathrm{d}d$, located at a spatial position x at time t about intervals $\mathrm{d}x$ and $\mathrm{d}t$ respectively.

For a discrete system the number density $n(d_i, \boldsymbol{x}, t)$ can be related to the more general continuous number density distribution function f according to

$$n(d_i, \boldsymbol{x}, t) = \int_{d_{i-1/2}}^{d_{i+1/2}} f(d, \boldsymbol{x}, t)\mathrm{d}(d), \tag{1.1}$$

where $[d_{i+1/2} - d_{i-1/2}]$ is the ith bin width. The population balance equation considering only the effects of droplet breakup and coalescence can be written as :

$$\frac{\partial n(d_i, \boldsymbol{x}, t)}{\partial t} + \nabla_{\boldsymbol{x}} \cdot [\boldsymbol{v}(d_i, \boldsymbol{x}, t) n(d_i, \boldsymbol{x}, t)] = S_{b,i} + S_{c,i}, \tag{1.2}$$

where $n(d_i, \boldsymbol{x}, t)$ is the number density of droplets of diameter d_i, $\boldsymbol{v}(d_i, \boldsymbol{x}, t)$ is the droplet velocity, $S_{b,i}$ and $S_{c,i}$ are source terms for droplet breakup and coalescence affecting droplets of diameter d_i (within bin i), respectively. The divergence is calculated with respect to the spatial coordinate $\boldsymbol{x}$. In order to close the equation, one needs reliable models for the breakup and coalescence source terms. In systems with small dispersed phase volume fractions, droplet coalescence can be neglected ($S_{c,i} = 0$). The complex nature of the PBE precludes analytical solutions for all but simple breakage and aggregation kernels[26,121]. Numerical solution methods have been developed to obtain solutions for equation (1.2). The most extensively used methods include the method of moments[39,69,66,65,115], multi-class method[66,53,105,52], method of weighted residu-

als[110] and Monte-Carlo methods[57,117].

The method of moments aim to solve the PBE by approximating the moments of the number density function by an n-point quadrature and is popular for growth problems[69]. Another approach developed was the direct quadrature method of moments (DQMOM)[66] that transported the primitive variables (weights and abscissas) instead of the moments. The major limitation of these methods was the difficulty of coupling them with Computational fluid dynamics (CFD). For instance, DQMOM method is known to fail for purely hyperbolic transport equations with velocity as the internal co-ordinate. The coupling of methods of moments with CFD is still an important research topic. In particular, capturing effects like particle trajectory crossing in Large Eddy Simulations (LES) requires a large number of moments to capture both the effects of the subgrid-scale on the dispersed phase as well as trajectory crossing due to large-scale eddies[55].

The multi-class formulation allows us to study the evolution of polydisperse liquid droplets with high accuracy while preserving important moments of the distribution. In this method the internal co-ordinate (droplet size, velocity etc.) is divided into a number of small contiguous subclasses, and the PBE is converted into a number of discretized transport equations for each class (bin)[86,51]. These methods are relatively easier to couple with large-eddy simulations and has found success in applications studying oil plume transport in the

ocean[112,113,19]. The major limitation of such a method is it becomes computationally expensive for a large number of classes. Therefore, there is a trade-off between accuracy (requiring large number of classes) and computational costs. There is a need to formulate a model that can accurately capture the size distribution using a relatively smaller number of classes (10-20) to discretize the size range.

1.2 Droplet Breakup Models

In order to solve the population balance equation described in equation (1.2), one needs a model for the breakup source term S_b. The source term can be written as,

$$S_b(d,t) = \int_d^\infty m(d_0)\beta(d;d_0)g(d_0,t)n(d_0,t)\mathrm{d}(d_0) - g(d,t)n(d,t) \tag{1.3}$$

The first term on the right-hand side of equation (1.3) represents the birth of droplets of diameter d due to the total contribution from breakups of larger droplets. The second term accounts for death of droplets of size d due to breakup. The factor $\beta(d;d_0)$ is the probability density function associated with the formation of a droplet of size d due to the breakup of a parent droplet of size d_0 and $m(d_0)$ is the number of daughter droplets formed. In order to solve equation (1.2), models are needed for the probability density function $\beta(d;d_0)$ and the

breakup frequency $g(d)$.

For a turbulent flow, breakup due to shearing-off processes and due to interfacial instabilities are often neglected[61]. A number of models for the breakup frequency have been developed for breakup due to turbulent fluctuations. The turbulent fluctuations need to overcome the main resistive forces in the droplet, namely surface tension and viscosity. Existing models are typically based on four breakup criteria[61] : (1) turbulent kinetic energy of droplets E_d greater than a critical energy E_c[23,17]; (2) Velocity fluctuation around the particle surface Δu greater than a critical value[73,4]; (3) Turbulent kinetic energy of bombarding eddies E_e greater than a critical value E_c[81,104,62,67] and; (4) inertial force of the bombarding turbulent eddy being greater than the interfacial force of the smallest daughter particle[58,59].

Eddy-collision models are among the most popular models where the interaction between eddies and droplets are treated similar to collisions between molecules in the kinetic theory of gases[81,104]. A collision frequency is defined based on the size of the eddy and droplet, and their typical relative velocity at that scale. The relative velocity is generally calculated by assuming Kolmogorov scaling. The requirement for breakup in such a model follows criteria (3) where the turbulent kinetic energy of the colliding eddy is greater than the potential energy associated with the resistive forces of the droplet. The resistive forces include the droplet surface energy and viscous resistive

stresses[93,119]. In most formulations, the scales of the colliding droplets and eddies were assumed to be in the inertial range of turbulence. Hence a Kolmogorov scaling valid for the inertial subrange was used to estimate the magnitude of eddy-velocity fluctuations at a particular scale. This precludes these models from being able to calculate the breakup frequency for droplets that fall in or near the viscous range, e.g. below η up to approximately 15η, where η is the Kolmogorov length scale. For instance, consider the stirred tank experiment[74] with an average energy dissipation $\epsilon = 9\ m^2 s^{-3}$, has a viscous range of approximately $13\eta = 260\ \mu m$ where $\eta = (\nu^3/\epsilon)^{1/4}$ is the Kolmogorov microscale. The size range of droplets observed in the experiment ranged from $40 - 500\ \mu m$ having a significant portion of the size distribution in the viscous range. Moreover, the overestimation in eddy fluctuation velocities (see Figure 2.1) for viscous range droplets result in existing models needing system dependent model constants to fit the data. There is a need to develop breakup models that is valid for the entire spectrum of turbulence. Recently, there has been progress in including the entire turbulence spectrum while modelling the breakup frequency[99]. Breakup frequencies obtained by incorporating the structure function valid for the viscous range, has shown promise when compared to single droplet breakup experiments[44,45].

In addition to the breakup frequency, a model for the breakup probability density function $\beta(d; d_0)$ is required. Numerous empirical[37], phenomenolog-

ical[104,62,67,58,107] and statistical[73,81] models have been presented in the literature. There is little agreement over the correct form of the probability density function. Most models either espouse a $\bigcup$-shaped or $\bigcap$-shaped distribution. Phenomenological or statistical distributions only depend on the size of the droplets and ignore the turbulence properties of the fluid. Models taking into account turbulence properties of the system have been developed either from phenomenological arguments or directly from the breakup frequency[67,106]. Recently, Qi et al.[82] developed a breakup probability model based on experimental constraints that sought to reproduce the bubble size distribution spectrum. They found that the correct form of the probability density function was critical in determining sub-Hinze scale droplet size distribution, whereas the breakup frequency determined the super-Hinze scale scalings.

1.3 Numerical Modelling of Turbulent Polydisperse Systems

There have been numerous models developed to predict the mean diameter or the steady state droplet size distribution[6,11,42,118,119] in two-phase turbulent systems. One of the earliest applications of modelling a polydisperse system using population balance equations in a turbulent fluid was in agitated liquid–liquid dispersions (stirred tank reactors)[23,73,12,104,81,106].

In turbulent particle-laden simulations the evolution of the carrier (fluid) and the dispersed phase (bubbles/droplets) are often coupled with dynamics of one phase affecting the other. Large-eddy simulations (LES) are effective in resolving the large and intermediate scale structures of a turbulent flow, and only require modeling of the unresolved subgrid turbulent effects. Pedel et al.[79] used large eddy simulation (LES) coupled with an Eulerian solver for the droplet phase to predict droplet concentrations using the direct quadrature methods of moment (DQMOM). Further work combining LES for the carrier flow with PBE for droplets can be found in Seubert et al.[91], Sewerin and Rigopoulos[92] and Salehi et al.[87], the latter of which used LES for the carrier phase coupled with a statistical Lagrangian approach for the droplets. LES for modelling two phase systems are broadly classified into either Eulerian-Eulerian models where the distribution of droplets in the entire size range is described by a continuous number density field[114,87] or Eulerian-Lagrangian, where individual droplets or droplet clusters are tracked in a Lagrangian fashion[15,5]. Introducing breakup or coalescence in the Lagrangian framework leads to an uncontrollable computational load due to change in number of numerical particles. Moreover the Lagrangian approach requires a subgrid scale model to represent the small scale features, (thin films, micro bubbles etc.[16]). Eulerian methods, although limited to applications with relatively low volume fractions, can be advantageous since they are not limited by the number of droplets, as

the distribution of droplets in each size range is described by a continuous concentration field. The fast-Eulerian method[31] models the droplet velocity as a function of the droplet time scale, instead of having to solve separate transport equations (as is done in the two-fluid model). The limitation of this method is that it assumes the particle stokes number to be small.

Many important systems can be idealized to the case of droplet formation and breakup processes in turbulent jets and plumes. The turbulence properties of these flows can be well characterized in both experiments and simulations. It is therefore the ideal flow configuration to study droplet breakup and transport. Many dispersed phase systems such as spray combustion, spray coating and oil spill modelling rely on understanding particle-turbulence interaction for mixing and dispersion[47]. Polydispersity adds an additional layer of complexity in modelling particle dispersion. Preferential concentration of particles could result from inertial effects (lift forces on different sized particles), clustering (either strain or vorticity dominated) or buoyancy effects (modified diffusion due to crossing of trajectories)[24,108] . These effects have been studied extensively for mono-dispersed systems[30,9,28]. There have been recent efforts in coupling LES flow solvers, with a probability density function (PDF) formulation of the population balance equation in order to study particle dispersion[88,89]. Moreover, Eulerian–Eulerian LES has been used to successfully model monodisperse bubble plumes in a quiescent fluid[114]. This thesis works

towards developing an Eulerian-Eulerian LES model for polydisperse droplet plumes.

In most applications, two-phase jet flows are characterized by a large separation of scales ranging from a few hundred microns (droplet scale), to the order of millimeters (nozzle scale), and up to meters (jet far field or plume). In environmental applications this separation of scales can be even larger. Direct numerical simulations of such systems becomes intractable due to the high computational cost involved in attempting to capture all relevant scales. Modeling approaches are needed, and focus on providing averaged or 'coarse-grained' solutions. Such approaches must make judicious choices weighing computational cost with accuracy and considering how much details about the simulated phenomena are needed. While simulating smaller nozzle sizes, a coarse Eulerian LES-PBE approach requires an inlet boundary condition for the droplet size distribution that is generated in the primary breakup zone. Typically, a monodisperse size distribution is used as inflow in such cases, but this is not sufficiently realistic. In the case of atomization, integral models have been developed to predict the mean diameter generated in the near nozzle region. The characteristic diameter in conjunction with an assumed distribution such as a "Rossin-Rammler"[35,29] or "lognormal"[96] can be used for the inlet cumulative volume fraction. However, an approach based on physical mechanisms would be more robust rather than statistical descriptions.

1.4 Experimental Data for Model Validation

There is an extensive body of literature studying droplet breakup in turbulent liquid-liquid dispersions. Numerical modelling needs to be supplemented by suitable experimental data for validation. It is essential that the turbulence is well characterized in the experiments and the measurement techniques be non-intrusive in order to accurately characterize the droplet distribution in the flow. Turbulent systems exhibiting high levels of anisotropy and spatial heterogeneity are difficult to characterize. For instance, stirred tank systems contain highly localized high shear regions near the surface of the impeller blades and strong tip vortices shed by the blades. Experiments of liquid jets or oil droplets injected in a turbulent jet or plume are ideal candidates for model validation.

Martínez-Bazán et al.[67] designed and carried out a series of experiments where air bubbles were injected into a fully developed turbulent water jet. This ensured that the turbulence was well characterized and size distributions could be measured using non-intrusive optical techniques. Eastwood et al.[27] injected droplets of varying density, viscosity and interfacial tension into a fully developed water jet and tracked particle size distributions using digital image processing techniques. Brandvik et al.[11] performed oil jet experiments in a very large cylindrical tank. They measured droplet size distributions using

an *in situ* laser diffractometer. Murphy et al.[72] used an oil jet in cross-flow to study the droplet breakup and resulting size distributions. Their experiment consisted of a nozzle supported by a carriage that was moved at a constant speed thus setting up a cross-flow. The size distribution was measured non-intrusively using in-line holographic techniques. Zhao et al.[120] conducted a large scale experiment of underwater oil release through a 25.4 mm pipe. They measured size distributions using two LISSTs (laser *in situ* scattering and transmissometry) in the range of 2.5–500 μm. Recently there have been advances in using ultra-small angle x-ray scattering[46] and refractive index matching with planar laser-induced fluorescence[111] in order to probe the near nozzle region of the jet.

1.5 Outline

This thesis works towards coupling population balance equations with large-eddy simulations in order to study the evolution and transport of polydisperse liquid droplets in a turbulent flow. Furthermore, we seek to improve the state of the art in breakup modelling by formulating a droplet breakup kernel valid for the entire turbulent spectrum. In this project we (1) develop and validate a droplet breakup model based on eddy-droplet collisions valid for the inertial and viscous range of turbulence; (2) predict the droplet size distribution

of liquid droplets in a turbulent jet by coupling a population balance equation with large-eddy simulations; (3) develop a hybrid ODE-LES approach based on turbulent jet theory to determine the inlet size distribution for coarse large-eddy simulations of turbulent round jets; and (4) quantify the variability of key quantities derived from the size distribution. The rest of the thesis is organized into the following chapters.

In Chapter 2, we formulate a droplet breakup model valid for inertial and viscous range of turbulence and validate it with experimental data. We discuss in Chapter 3 the numerical methods (LES) and tools used to study the evolution of polydisperse droplets in a turbulent flow. We discuss the method of generating coarse turbulent jets in LES and include validations with experiments. In Chapter 4 we present results from LES of a lab scale oil spill using a jet in crossflow as a surrogate for the experimental configuration. Additionally, we explore the variability of key quantities of the size distribution. Chapter 5 presents a hybrid ODE-LES approach to generate realistic inlet conditions for coarse LES of turbulent oil jets using turbulent jet theory. Chapter 6 presents simulations of a turbulent round jet at two different Weber numbers, quantifying statistics of the velocity and concentration fields. Additionally, we quantify the radial profiles of the mean and variability of the Sauter diameter, total surface area breakup source terms. Chapter 7 explores the size based differential droplet dispersion due to trajectory crossing effects. Conclusions and future

work are discussed in Chapter 8.

Chapter 2

Droplet Breakup Model

The mechanisms governing droplet or bubble breakup in turbulent dispersions has been the subject of significant theoretical and experimental study[54,61]. As discussed in Chapter 1 there are numerous models proposed for the droplet breakup frequency $g(d)$ and the droplet breakup probability density $\beta(d; d_0)$.

Coulaloglou and Tavlarides[23] were among the first to introduce a simple macroscopic formulation to study breakup and coalescence in an agitated liquid–liquid dispersion. Over the years, a considerable number of studies have been performed for steady-state size distributions in stirred vessels[23,104,81,106]. In most of the previous formulations, the scales of the colliding droplets and eddies were assumed to be in the inertial range of turbulence. Hence a Kolmogorov scaling valid for the inertial subrange was used to estimate the magnitude of eddy-velocity fluctuations at a particular scale. This precludes these

models from being able to calculate the breakup frequency for droplets that fall in or near the viscous range, e.g. below η up to approximately 15η, where η is the Kolmogorov length scale. In Figure 2.1 we compare the (square) eddy fluctuation velocity (or second order structure function) assuming Kolmogorov scaling (black dashed line) to the expression valid for both inertial and Kolmogorov scale. We can see that considering only an inertial scaling for the fluctuation velocity can lead to an overestimation for viscous range interactions. Moreover, the LES grid scale (examples shown as blue vertical dashed lines in equation (2.9)) can lie in either the inertial or the viscous range. A model for the subgrid velocity fluctuations that can encompass both the inertial and viscous range is essential.

A unified treatment is needed to extend these models to the entire spectrum of turbulence. One approach is to consider a model energy spectrum[80] for the complete range of scales. Using a Fourier series transform, an expression for the second-order structure function can be derived, that includes the viscous range[99]. The resulting expressions are quite complicated, owing to the particular functional form of the viscous cutoff in spectral space. However, a more direct approach and simpler expressions can already be found in the literature, based on the Batchelor blending function[7] written directly for the structure function in physical space to model the eddy-velocity fluctuations (equation (2.9)

The Chapter is organized as follows. We discuss the breakup probability model and the formulation of the breakup frequency model in section 2.1. We then determine the model constant in section 2.2 using a wave-breaking experiment[60] and present the model validation using an experiment studying the breakup of oil droplets injected at the centerline of a turbulent jet[27]. We present conclusions in section 2.4. The content in this chapter is published in Aiyer et al.[1].

2.1 Breakup Model Formulation

The population balance equation, neglecting the effect of coalescence and written using the droplet size (diameter d_i) as the internal coordinate, is given by

$$\frac{\partial n(d_i, \boldsymbol{x}, t)}{\partial t} + \nabla \cdot [\boldsymbol{v}(d_i, \boldsymbol{x}, t) n(d_i, \boldsymbol{x}, t)] = S_b(d_i, \boldsymbol{x}, t), \tag{2.1}$$

where $n(d_i, \boldsymbol{x}, t)$ is the number density of droplets in the ith bin representing droplets of diameter around d_i, at location $\boldsymbol{x}$ at time t. The divergence is calculated with respect to the spatial coordinate $\boldsymbol{x}$. The source term due to breakup is written according to Zhao et al.[119],

$$S_b(d_i, \boldsymbol{x}, t) = \sum_{j=i+1}^{n} P(d_i, d_j) g(d_j, \boldsymbol{x}, t) n(d_j, \boldsymbol{x}, t) - g(d_i, \boldsymbol{x}, t) n(d_i, \boldsymbol{x}, t). \tag{2.2}$$

The first term on the right-hand side of equation (2.2) represents the birth of droplets of size d_i due to the total contribution from breakups of larger droplets of diameter d_j. The second term accounts for death of droplets of size d_i due to breakup. The factor $P(d_i, d_j)$ is the probability of formation of a droplet of size d_i due to the breakup of a parent droplet of size d_j, and $g(d_i, \boldsymbol{x}, t)$ is the breakup frequency of a droplet of size d_i (in bin i). The breakup probability can be related to the probability density function $\beta(d_i, d_j)$, i.e. $P(d_i, d_j) = \beta(d_i, d_j)\delta(d_i)$, where $\delta(d_i)$ is the width of the bin centred at d_i.

2.1.1 Model for the Breakup Probability.

Models for the breakup probability function $P(d_i, d_j)$ (or $\beta(d_i, d_j)$), can broadly be classified as statistical, phenomenological or empirical[54,61]. In this study we use the phenomenological model proposed by Tsouris and Tavlarides[104] that leads to a "U-shaped" distribution. We keep in mind, however, that experiments for bubble breakup[67] have led to other possible shapes for $P(d_i, d_j)$ and that there remains considerable uncertainty about the best model to use. Here we proceed with the model of Tsouris and Tavlarides[104] because it is based on a relatively simple physical reasoning as shown below.

The breakup is considered to be binary, and $P(d_i, d_j)$ is formulated based on the formation energy required to form the daughter droplets of size d_i and a complementary droplet to ensure volume conservation[104]. The formation en-

ergy is proportional to the difference in initial and final surface areas according to

$$E_f(d_i, d_j) = \pi\sigma \left[(d_j^3 - d_i^3)^{2/3} + d_i^2 - d_j^2\right], \tag{2.3}$$

where σ is the interfacial tension between the dispersed and continuous phase. It can be shown using equation (2.3) that the breakup of a parent droplet into two equal size daughter droplets is a maximum energy process. Substituting $d_i = d_j/2^{1/3}$ in equation (2.3) we get a maximum formation energy equal to

$$E_{f,max} = \pi\sigma d_j^2(2^{1/3} - 1). \tag{2.4}$$

Equation (2.3) is minimized when $d_i = 0$, that is no breakup of the parent droplet. To allow for breakup, a minimum diameter d_{min} is specified and the corresponding surface formation energy is

$$E_{f,min} = \pi\sigma \left[(d_j^3 - d_{min}^3)^{2/3} + d_{min}^2 - d_j^2\right], \tag{2.5}$$

where $d_{min} = 1$ μm in this study. Making the crucial assumption that the probability of breakup of a drop of size d_j leading to a droplet of size such that it falls in a bin around d_i decreases linearly with the required formation energy and remains within the bounds specified above, the discrete breakup

probability $P(d_i, d_j)$ can be written as

$$P(d_i, d_j) = \frac{[E_{f,min} + (E_{f,max} - E_f(d_i, d_j))]}{\sum_{k=1}^{j-1} [E_{f,min} + (E_{f,max} - E_f(d_k, d_j))]}. \tag{2.6}$$

where $E_f(d_i, d_j)$ is the surface formation energy defined in equation (2.3). Also, we assume that the bin sizes are logarithmically distributed. Thus equation (2.6) is meant to model the discrete probability that a particle of size d_j breaks up into a particle inside a bin centred at d_i with a width of $\delta(\log(d_i))$, and its complement d_c (to conserve volume). This distribution is U-shaped, with a minimum probability for the formation of two equally sized daughter droplets (when $E_f(d_i, d_j) = E_{f,max}$ which leads to a maximum of required energy), and probability maxima at the two ends (which have formation energy minima).

Martínez-Bazán et al.[68] derived constraints that apply to the droplet size probability density function $\beta(d_i, d_j)$ for the breakup process to be volume conserving. The discrete probability of forming a droplet in bin d_i must be equal to the probability of formation of the complement in bin d_c (for binary breakup). The discrete breakup probability in equation (2.6) conserves volume, since $P(d_i, d_j) = P(d_c, d_j)$. We note that expressing this probability in terms of a universal density $\beta(d_i, d_j)$ presents further challenges[68] that are left for future analysis (see Chapter 8), while here we use the discrete version.

2.1.2 Model for Breakup Frequency

Modelling breakup based on encounter rates of turbulent eddies and their characteristic fluctuations with droplets of a certain size has been a popular method in the literature. The phenomenological model by Coulaloglou and Tavlarides[23] postulates that a droplet in a liquid–liquid dispersion breaks up when the kinetic energy transmitted from droplet–eddy collisions exceeds the surface energy. Many other papers have pursued this approach, mostly in the RANS context e.g[73][17]. Here we follow the approach of Prince and Blanch[81] and Tsouris and Tavlarides[104], where the droplet–eddy collisions are treated akin to the of collisions between molecules in kinetic theory of gases. The breakup frequency is computed as an integral over the product of a collision frequency and a breakup efficiency according to

$$g(d_i) = K \int_0^{d_i} \frac{\pi}{4}(d_i + d_e)^2 \, u_e(d_e) \, \Omega(d_i, d_e) \, \mathrm{d}n_e(d_e). \tag{2.7}$$

Here d_i is the diameter of the droplet, d_e is the eddy size, $n_e(d_e)$ is the number density of eddies of size d_e, $u_e(d_e)$ is the characteristic fluctuation velocity of eddies of size d_e (in a frame moving with the advection velocity caused by larger eddies), $\Omega(d_i, d_e)$ is a breakup efficiency and the integral is evaluated over all eddies, up to the size of the droplet (i.e. for d_e up to $d_e = d_i$). A crucial assumption of the model is that eddies larger than the scale of the droplet are

assumed to be only responsible for advection of the droplet, not contributing to collisions with the droplet that require relative velocity. One could develop a "smoother" model in which the lack of deformation due to eddies larger than d_i is included as an additional cutoff behaviour in the function $\Omega(d_i, d_e)$. Here we choose to include that cutoff behaviour by following earlier work[104,62] as a sharp cutoff, while lumping any possible dependencies on the exact cutoff scale into the unknown model parameter K, expected to be of order unity.

The number density of eddies, $n_e(d_e)$, can be estimated from the energy spectrum[104,34,100,97], or more simply by assuming the eddies to be space filling, i.e, $n_e(d_e) \propto d_e^{-3}$. The latter argument leads to $\mathrm{d}n_e(d_e) = C_1 d_e^{-4}\mathrm{d}(d_e)$, where C_1 is a constant of order 1.

The eddy fluctuation velocity $u_e(r)$ written in terms of the two-point separation distance, r, is assumed to be expressed based on the second-order longitudinal structure function $S_2(r)$ as $u_e(r) \sim [S_2(r)]^{1/2}$. The structure function is defined according to[80]:

$$S_2(r) =< \left[u_L(\mathbf{x} + r\mathbf{e}_L) - u_L(\mathbf{x})\right]^2 >, \tag{2.8}$$

where u_L is the fluid velocity component in the direction of unit vector $\mathbf{e}_L$ and the angular brackets represent statistical averaging. In previous models[104,6,119] a Kolmogorov scaling valid in the inertial range of turbulence was used for

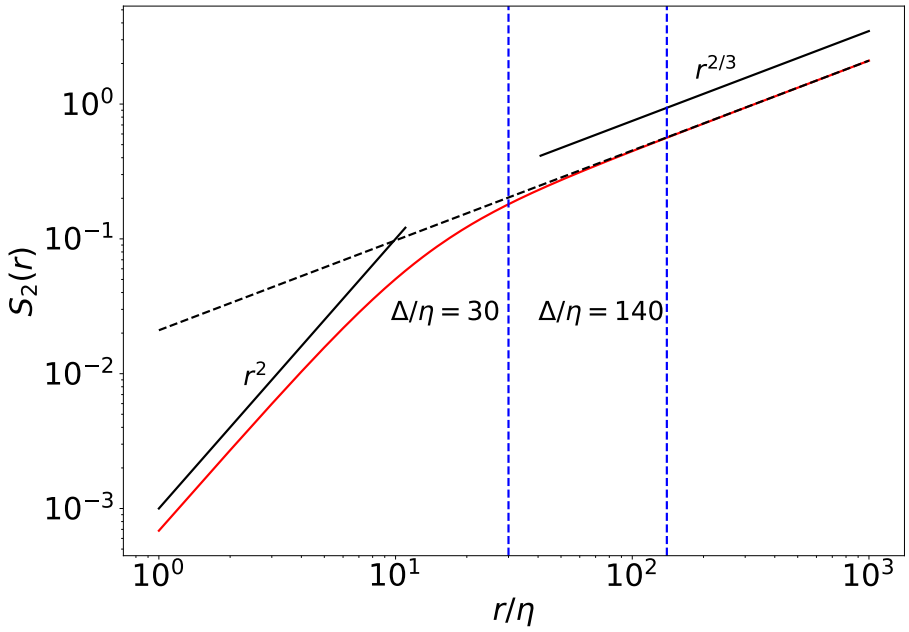

Figure 2.1: Normalized eddy fluctuation velocity calculated using inertial range scaling (- - -) and using a scaling valid for the viscous and inertial range of scales (—). LES filter scale is denoted by the blue dashed line.

$S_2(r)$, leading to $u_e(r) \sim (\epsilon r)^{1/3}$. However, this expression cannot be used if the size of the droplet is near the viscous range of turbulence. In order to capture both inertial and viscous ranges, as well as a smooth transition between the two ranges, we use the approach of Batchelor[7] with a blending function. In this approach, the structure function is given by

$$S_2(r) = C_2 \epsilon^{2/3} r^{2/3} \left[1 + \left(\frac{r}{\gamma_2 \eta} \right)^{-2} \right]^{-2/3}, \tag{2.9}$$

where η is the Kolmogorov length scale. We choose the usual value for the Kolmogorov coefficient $C_2 \approx 2.1$[80]. The parameter $\gamma_2 = (15C_2)^{3/4} \approx 13$ sets the

cross-over scale between the inertial and viscous range. As can be seen from Figure 2.1, the eddy fluctuation velocity is proportional to r^2 in the viscous range and $r^{2/3}$ in the inertial range with equation (2.9) providing a smooth transition between the two. We note that while most prior models are for use in a RANS framework using the average energy dissipation, ϵ, in LES we can use a local value of the instantaneous rate of dissipation averaged over the grid scale, modelled as the subgrid-scale (SGS) dissipation rate. As a result, even though equation (2.9) is based on K41 theory, in LES we only assume K41 scaling for the scales below the grid scale while intermittency in the resolved range of scales can be explicitly computed, and its effects on breakup rates taken into account in the LES model.

The breakup efficiency $\Omega(d_i, d_e)$ in equation (2.7) is the probability that a given eddy interacting with the droplet has sufficient energy to overcome the resistive forces in the system, namely surface tension and viscosity. It is assumed to be given by the usual formation potential in terms of an exponential[23,81]

$$\Omega(d_i, d_e) = \exp\left(-\frac{E_\sigma(d_i) + E_\nu(d_i)}{E_e(d_e)}\right), \tag{2.10}$$

where $E_\sigma(d_i)$ is resistive energy associated with a droplet of size d_i due to surface tension, $E_\nu(d_i)$ is the viscous resistive energy and $E_e(d_e)$ is the kinetic energy of the turbulent eddy at scale d_e. The resistive surface tension energy E_σ is defined as the integral of the formation energy $E_f(d', d_i)$ multiplied by a

measure of the breakup probability (see equation (2.6)):

$$E_\sigma(d_i) = \int_0^{d_i} c\left[E_{f,min} + (E_{f,max} - E_f(d', d_i))\right] E_f(d', d_i)\mathrm{d}(d'), \tag{2.11}$$

where c is a normalization constant so that the integral of the probability between 0 and d_i is unity. Using equation (2.3), changing the integration to $\xi' = d'/d_i$ and evaluating the integral numerically, we obtain

$$E_\sigma(d_i) = 0.0702\ \pi\sigma d_i^2, \tag{2.12}$$

where σ is the surface tension of the droplet. The viscous resistive energy of the droplet at steady state can be expressed as[12,93,119]

$$E_\nu(d_i) = \alpha\frac{\pi}{6}\epsilon^{1/3}d_i^{7/3}\mu_d\sqrt{\frac{\rho_c}{\rho_d}}, \tag{2.13}$$

where $\alpha \approx 2$, ρ_c and ρ_d are the carrier and droplet phase density, and μ_d is the dynamic viscosity of the dispersed droplet phase. For $E_e(d_e)$, the kinetic energy of the turbulent eddy, we use the longitudinal structure function S_2, defined in equation (2.9) applied to all three coordinate directions for the eddy fluctuation velocity, u_e. Assuming the volume of the eddy to be equal to that of a sphere, with density equal to the carrier phase density, the total energy contained in

an eddy can be written as

$$E_e(d_e) = \frac{3}{2}\left(\frac{\pi}{6}\rho_c d_e^3\right) S_2(d_e). \tag{2.14}$$

In order to formulate a parameterization for the breakup frequency, here we identify the important nondimensional numbers of the system. The breakup frequency can be re-written as a function of the Reynolds number (Re_i) based on droplet diameter and a velocity scale defined as $u_{d_i} = (\epsilon d_i)^{1/3}$, the Ohnesorge number ($Oh_i$) of the dispersed phase controlling the relative importance of viscosity to surface tension of the droplet, and the density and viscosity ratio of droplet to carrier flow fluid. These nondimensional numbers are defined below,

$$Re_i = \frac{\epsilon^{1/3} d_i^{4/3}}{\nu} \quad ; \quad Oh_i = \frac{\mu_d}{\sqrt{\rho_d \sigma d_i}} \quad ; \quad \Gamma = \frac{\mu_d}{\mu_c}\left(\frac{\rho_c}{\rho_d}\right)^{1/2} \tag{2.15}$$

After some manipulation, equation (2.7) can be rewritten as

$$g_i = K^* \frac{1}{\tau_{b,i}} \int_0^1 r_e^{-11/3}(r_e+1)^2 \left(1 + \left(\frac{r_e Re_i^{3/4}}{\gamma_2}\right)^{-2}\right)^{-1/3} \Omega(Oh_i, Re_i, \Gamma; r_e)\, \mathrm{d}r_e, \tag{2.16}$$

where, $r_e = d_e/d_i$ is the eddy size normalized by the droplet diameter, $\tau_{b,i} = \epsilon^{-1/3} d_i^{2/3}$ is the breakup time scale for an eddy of size equal to that of the droplet as if it were in the inertial range (it does not have to be), and $\Omega(Oh, Re, \Gamma; r_e)$ is

the nondimensional breakup probability,

$$\Omega(Oh, Re, \Gamma; r_e) = \exp\left(-\frac{\Gamma f_2}{Re}\left[1+\left(\frac{r_e Re^{3/4}}{\gamma_2}\right)^{-2}\right]^{2/3} r_e^{-11/3}\right), \tag{2.17}$$

where

$$f_2 = 0.14\frac{\Gamma}{Re\,Oh^2} + 0.583. \tag{2.18}$$

All the nondimensional prefactors appearing when rewriting equation (2.7) have been absorbed into K^*. Equation (2.16) provides a frequency for droplet breakup that depends on Re_i, Oh_i and Γ. Note that if we had only considered an inertial range scaling for the eddy fluctuation velocity, we can combine Re and Oh into a Weber number, defined as $We = Re^2\ Oh^2$. The breakup frequency would then only depend on We and Γ. The integral represents a correction to the frequency calculated by solely considering an eddy equal to the size of the droplet, by evaluating the effect of collisions of eddies smaller than the droplet. If d_i falls in the viscous range, the integral cancels the inertial range scaling assumed by the prefactor $\tau_{b,i} = \epsilon^{-1/3} d_i^{2/3}$ so that this situation is also accounted for. We note that the value of the integral $g_i \tau_{b,i}/K^*$ in equation (2.16) will inevitably depend on the assumed maximum eddy size interacting with the droplet, which is currently taken to be exactly the droplet size d_i. However, if one were to take a different upper integration limit (still of order d_i but not exactly d_i), the breakup frequency may not change much since the modified

value of the integral will be largely (but not exactly) canceled when fitting the prefactor K^* to data. This behaviour is demonstrated in the next section.

In LES, g_i needs to be evaluated on every grid point and timestep, depending on the local Reynolds number Re_i and the local rate of dissipation. Evaluating numerically the integral in equation (2.16) at every timestep and grid point would be prohibitive in practice. Hence, we develop an empirical fit to prior numerical integrations. The speedup obtained from the fits is discussed in Appendix A. We develop the parameterization for a wide range of Reynolds and Ohnesorge numbers, for a fixed value of Γ. We define $g_f(Re, Oh, \Gamma)$ as the integral in equation (2.16), i.e. $g_f(Re, Oh, \Gamma) = g_i(Re_i, Oh_i, \Gamma)\,\tau_{b,i}/K^*$, and evaluate it numerically for a range of Re and Oh values for a fixed Γ. Then, a fit can be developed in the following form,

$$\log_{10}(g_f) = ax^b + cx^d - e, \tag{2.19}$$

where $x = \log_{10} Re$, and a, b, c, d, e are functions of Oh. Further details of the functional form of the coefficients are provided in appendix A. The final model for the breakup frequency (for a given value of Γ) thus has the form

$$\begin{aligned} g_i(Re_i, Oh_i; \Gamma) &= \frac{K^*}{\tau_{b,i}}\, 10^{G(Re_i, Oh_i)}, \\ G(Re_i, Oh_i) &= a\,[\log_{10}(Re_i)]^b + c\,[\log_{10}(Re_i)]^d - e, \end{aligned} \tag{2.20}$$

where the fits for parameters a–e as functions of Oh are provided in appendix A for a few representative values of Γ.

The breakup frequency model is thus complete except for the prefactor K^* appearing in equation (2.16). Its value is obtained by fitting results from an experiment (see next section), and the fitted value will then be used subsequently for comparisons with other data and for future applications.

2.2 Determining the Model Constant

2.2.1 Wave Breaking Experiment

In order to fit a specific value for the parameter K^* we use the data of a breaking wave experiment from Li et al.[60]. The experiments were performed in an acrylic tank 6 m long, 0.6 m deep and 0.3 m wide. Breaking waves were generated mechanically using a piston-type wave maker consisting of a vertical plate that extends over the entire tank cross section. The tank was filled with water up to a height of 0.25 m. The wave height and characteristics were controlled by varying the frequency and stroke of the vertical plate. Oil was placed on a patch at the surface. The wave impingement and subsequent breakup processes were recorded using 3 high-speed cameras. The droplet size distribution was measured using digital inline holography. A sketch of the setup is de-

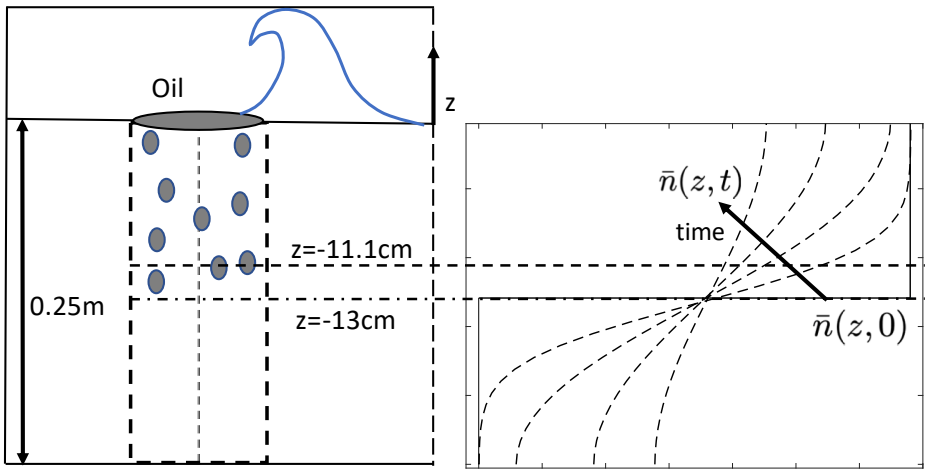

Figure 2.2: Left: Sketch of the wave breaking experiment of Li et al.[60]. Right: schematic dependence of $\overline{n}_i(z,t)$ on time and height for a particular droplet size, starting from a step-function initial condition that is assumed to be well mixed initially down to a depth of 13 cm below the surface and having zero concentration below. At increasing times, turbulent diffusion smooths the step and droplets rise towards the surface at different speeds depending on their size. The dotted horizontal line at $z = -11.1$ cm is where the experimental data is available.

picted in Figure 2.2. The oil patch on the surface was broken up into droplets by the plunging wave. The size distribution generated due to this process was recorded at a depth of 11.1 cm from the free surface. A simplified sketch of the evolution of the concentration of a particular droplet size is shown in the right panel of Figure 2.2.

2.2.2 A Column Model for Droplet Size Distributions

As shown by Li et al.[60], the time evolution of the droplet size distribution at the measurement location could be represented well by a simple model that

includes the effects of turbulent diffusion and droplet buoyancy only. Since the dissipation rate was quite low at the measurement location, Li et al.[60] neglected the effect of droplet breakup in their model. Consequently, for the case of crude oil with dispersants, the model under-predicted the number of smaller size droplets generated. This is due to the fact that with the effect of dispersants, the surface tension of the oil droplets was significantly lowered, resulting in droplet breakup despite of the weak turbulent dissipation rate. The Weber number ($We = 2\rho(\epsilon d)^{2/3}d/\sigma$) based on the droplet diameter for the case with dispersants is approximately $We = 3$, confirming that the effects of droplet breakup are important. Our goal is to expand the model of Li et al.[60] by including breakup and select a value of K^* that can achieve improved agreement with their experimental data.

Adding the effect of breakup and following Li et al.[60] in considering only vertical diffusion and droplet rise velocity, the ensemble averaged number density $\bar{n}_i(z,t)$ for a droplet of size d_i obeys

$$\frac{\partial \bar{n}_i(z,t)}{\partial t} + w_r(d_i)\frac{\partial \bar{n}_i(z,t)}{\partial z} = \mathcal{D}(t)\frac{\partial^2 \bar{n}_i}{\partial z^2} + \sum_{j=i+1}^{n} P(d_i,d_j)g(d_j)\bar{n}_j(z,t) - g(d_i)\bar{n}_i(z,t), \tag{2.21}$$

where z is the vertical coordinate, $w_r(d_i)$ is the buoyancy-induced rise velocity of droplets of size d_i and $\mathcal{D}(t)$ is the turbulent diffusion coefficient. The daughter droplet probability function $P(d_i,d_j)$ and the breakup frequency g are evaluated

following the model presented in §2.1. The droplet rise velocity is calculated as a balance between the drag and buoyancy force acting on a droplet.

$$w_r(d) = \begin{cases} w_{r,S}, & \text{if } Re_d < 0.2, \\ w_{r,S}(1 + 0.15Re_d^{0.687})^{-1}, & 0.2 < Re_d < 750, \end{cases} \tag{2.22}$$

where

$$w_{r,S} = \frac{(\rho_0 - \rho_d) g\, d^2}{18\mu_f}, \tag{2.23}$$

and $Re_d = \rho_0 w_r d/\mu_f$ is the droplet rise velocity Reynolds number (not to be confused with the eddy Reynolds number Re_i used to express the breakup frequency). The time-dependent diffusion coefficient can be estimated using $\mathcal{D}(t) = k_D u'(t) L(t)$, where $u'(t)$ is the time-dependent turbulent fluctuation (root-mean-square) velocity as measured in the experiment and $L(t)$ is the corresponding integral length scale, also measured. The constant k_D is known to be between 0.23 and 0.6 for diffusion of droplets in isotropic turbulence[90,36]. We chose a value of $k_D = 0.3$ in accordance with Li et al.[60] for this study. Li et al.[60] fit the values of $u'(t)$ (in m/s) and ϵ (in $\mathrm{m^2 s^{-3}}$) with a power law in time. The data can be represented as $(\epsilon/\epsilon_0) = (t/t_0)^p$ and $(u'/u'_0) = (t/t_0)^q$ where $\epsilon_0 \approx 0.2$ $m^2 s^{-3}$, $u'_0 \approx 0.2$ m/s and $t_0 \approx 7$ s. The exponents p and q can be related by $p = 2q - 1$, and the data were fitted with $q = -0.89$[60]. The integral length scale $L(t)$ is then calculated as $u'(t)^3/\epsilon(t)$.

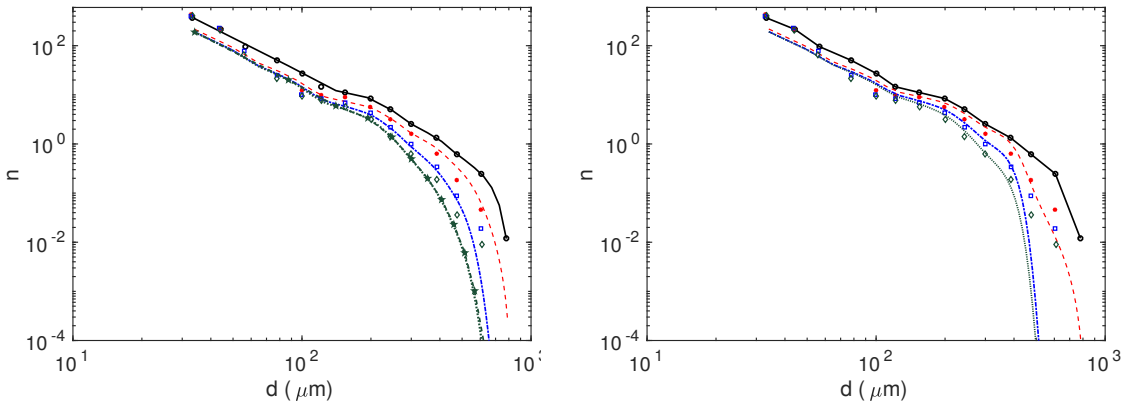

(a) $K^* = 0.2$. **(b)** $K^* = 1$.

Figure 2.3: Time evolution of the droplet size distribution for two values of K^*, at the measurement location. The symbols correspond to the experimental data, $t = 5$ s (–●–) represents the initial condition where experiment and column model are matched, $t = 15$ s (∗), $t = 35$ s (□), $t = 55$ s (◆), while the lines correspond to the column model, $t = 15$ s (- - -), $t = 35$ s (-·-·-) and $t = 55$ s (· · ·). The green stars (★) in (a) correspond to the size distribution at $t = 55$ s using $N_d = 15$ bins .

We solve equation (2.21) numerically for the number density of the oil droplets. We discretize the size range into $N_d = 70$ bins and assume that at the initial time all the concentrations are spatially homogeneous in the z direction down to an initial intrusion depth of $z = 13$ cm (see Figure (2.2)). The concentration equations are solved for each droplet size using a second-order Crank–Nicholson temporal discretization method. The boundary condition at the bottom of the domain, at $z = -25$ cm is that of no flux, i.e. $\bar{n}_i w_r - \mathcal{D}\frac{\partial \bar{n}_i}{\partial z} = 0$. A Neumann boundary condition is applied at the top surface, i.e. $\frac{\partial \bar{n}_i}{\partial z} = 0$. We initialize the concentration of each diameter bin with the measured concentration at $z = -11.1$ cm which was recorded after 5 s of impingement in the experiment. We integrate the model using different values of K^* ranging from

0 to 1.

In Figure 2.3 we compare the modelled size distributions (lines) to the experimental data (symbols) at various times, for $K^* = 0.2$ and $K^* = 1$, at the measurement location $z = -11.1$ cm. Since the initial condition (black circles in Figure 2.3) already includes the effects of significant initial breakup of the oil, a size distribution is already formed. Since the energy dissipation at the point of measurement, $z = -11.1$ cm is relatively low, the rate of further breakup is not very large and thus the effect of K^* in the model is subtle. Nevertheless, close inspection shows that there is too much breakup effect for the large droplets for $K^* = 1$, as we can see that the number density of the larger droplets is lower than the experimental data, especially for later times. Qualitatively, it appears that $K^* = 0.2$ captures the distribution slightly better, for both small and large droplets at the various time instants. We also calculate the size distribution in (2.21) using a coarser discretization of $N_d = 15$ bins. The resulting number density $\bar{n}$ is shown in Figure 2.3(a) at $t = 55$ s using green stars. We see that for this coarser resolution there is a good agreement with the $N_d = 70$ case.

In order to make a quantitative comparison we define an error measure $\mathcal{E}$ as the integrated squared difference between the logarithmic experimental and modelled size distributions. The error is calculated for each droplet size, and

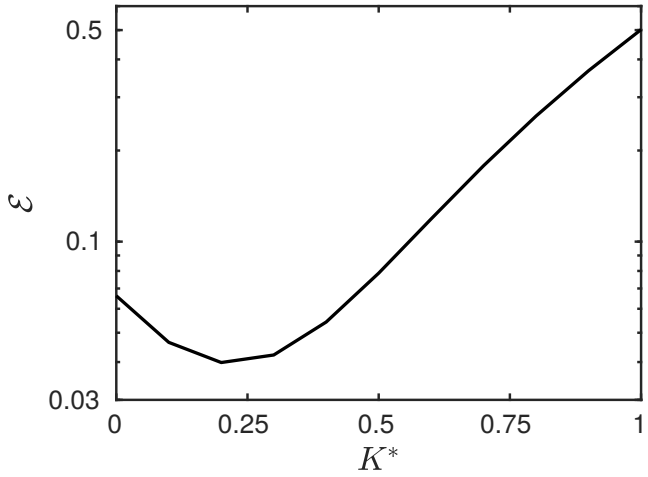

Figure 2.4: Average square error between predicted and measured logarithms of number densities averaged over 3 times during the evolution, at the measurement position, as a function of the breakup constant K^* assumed in the model.

integrated over all bins (the bin size varies logarithmically):

$$\mathcal{E} = \langle \sum_{i_{min}}^{i_{max}} [\log_{10}(\bar{n}_{expt}(d_i)) - \log_{10}(\bar{n}_{mod}(d_i))]^2 \ \frac{\delta d_i}{d_i} \ \rangle_t, \tag{2.24}$$

where δd_i is the bin width, n_{expt} refers to the experimental size distribution, and n_{mod} is the modelled one. The maximum diameter at which the experimental data are reported is $d \approx 500$ μm. Therefore, we select $i_{max} = 52$ corresponding to $d = 505$ μm. And we use $i_{min} = 4$ corresponding to $d = 86$ μm. The error is averaged over the three available times, $t = 15$ s, 35 s and 55 s.

As can be seen from Figure 2.4, the absolute value of the error is smallest at $K^* \approx 0.2$ and hence this value is chosen as the fitted parameter for future applications of the model. Note that $K^* = 0$ corresponds to the case without

breakup. We can see from Figure 2.4 that the error is larger, showing the improved agreement when including the breakup term in the model.

As stated earlier in the text, previous breakup models use an inertial-range scaling for the eddy fluctuation velocity for the entire range of scales,

$$u_e^2 = 2.1(\epsilon d_e)^{2/3}. \tag{2.25}$$

This approach results in overestimated velocities of eddies in the viscous range. In order to illustrate the net effects of this overestimation of turbulence at small scales in the overall model predictions, we can use equation 2.25 in (2.7) to compute the breakup frequency using $K^* = 0.2$ for this scaling of eddy velocity (through numerical integration). We solve equation (2.21) and plot the resulting size distributions in Figure 2.5. The left panel, Figure 2.5*a* compares the computed size distributions with the experimental data. We see that there is too much breakup effect resulting in too few of the larger droplets and an increase in the concentration of the intermediate-size droplets. In order to obtain a better agreement with the experiment we would need to set $K^* \sim O(10^{-2})$. Thus, we conclude that in order to maintain reasonable range of value for the parameter K^* (which is expected to be of order unity), it is important to capture both the inertial and viscous range scalings as in equation (2.9) for the eddy fluctuation velocity.

We can also study the effect of using a different breakup probability model $\beta(d_i, d_j)$. We use a truncated normal distribution of Coulaloglou and Tavlarides[23] for simplicity. In this case it is assumed that the daughter droplet sizes for a parent drop of diameter d_j are normally distributed about a mean value, $\bar{d} = d_j/2^{1/3}$, i.e.

$$\beta(d_i, d_j) = \frac{1}{s\sqrt{2\pi}} \exp\left[-\frac{(d_i - \bar{d})^2}{2s^2}\right], \tag{2.26}$$

where $s = d_j/(3 \times 2^{1/3})$. This gives us a maximum probability for equal volume breakup. We plot the resulting size distributions for $K^* = 0.2$ in Figure 2.5*b*. We observe a bump in the size distribution at $d \approx 300$ μm and a more rapid cutoff of the large droplets as compared to Figure 2.3(*a*). Additionally, we do not find an optimum value of K^* that minimizes equation (2.24), i.e. the error grows with increasing K^*. Hence, we may conclude that the form of the particular droplet breakup probability distribution is also important, though it plays a weaker role as compared to the effect of including the viscous range for this particular wave breaking case. In Chapter 8 we explore different breakup probability models formulated conservatively[68] by using a beta distribution.

We demonstrate the effect of an increase in the assumed maximum eddy size (upper limit of integration in equation allowed to break the droplets in Figure 2.6. We find that for a maximum eddy size 20% larger than the droplet size ($d_{e,max} = 1.2d_i$), the fitted prefactor is reduced to $K^* = 0.1$. Using this value of K^* we see from Figure 2.6a that the steady state size distribution is in good

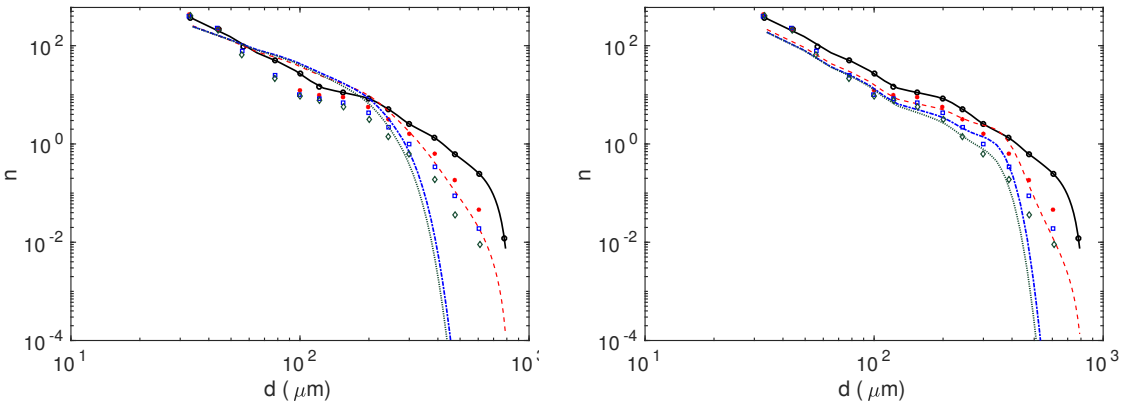

(a) $K^* = 0.2$. **(b)** $K^* = 0.2$.

Figure 2.5: Time evolution of the droplet size distribution for $K^* = 0.2$. (*a*) uses an inertial scaling of u_e. In (*b*) we plot the effect of using a normal distribution proposed by Coulaloglou and Tavlarides[23]. The symbols correspond to the experimental data, $t = 5$ s (–●–) represents the initial condition where experiment and column model are matched, $t = 15$ s (∗) , $t = 35$ s (□), $t = 55$ s (◆), while the lines correspond to the column model, $t = 15$ s (- - -), $t = 35$ s (-·-·-) and $t = 55$ s (· · ·).

agreement with case where $d_{e,max} = d_i$ and $K^* = 0.2$. Clearly, however the resulting breakup frequency shows some dependence on the upper cutoff of the integral (Figure 2.6b).

2.3 Droplet Breakup Model Validation

In order to begin testing the model when applied to a system with different flow properties than the case for which K^* was fitted, we consider the experiment by Eastwood et al.[27]. Oil droplets of varying density, viscosity and interfacial tension are injected continuously at the centerline in the fully developed region of a turbulent water jet. The downstream evolution of the centerline

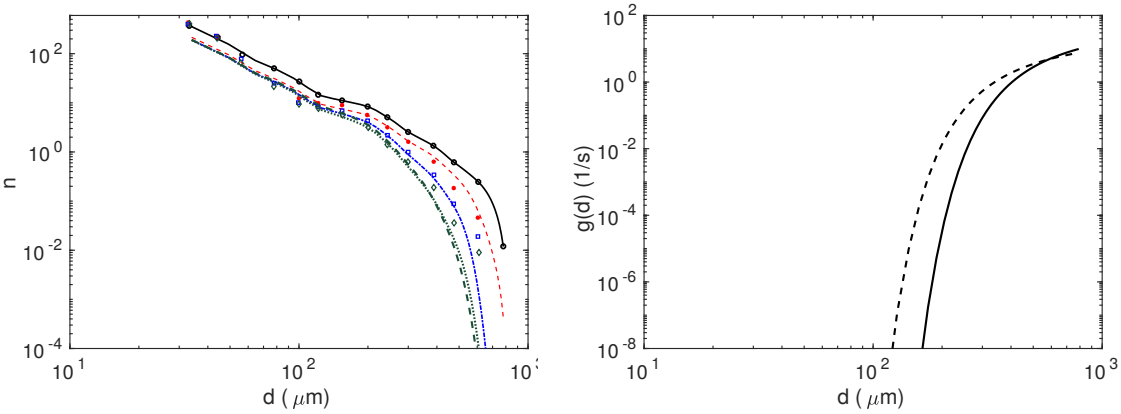

(a) **(b)**

Figure 2.6: We depict the effect of changing the maximum diameter size on the size distribution and breakage frequency. In (*a*) the symbols correspond to the experimental data, $t = 5$ s (–●–) represents the initial condition where experiment and column model are matched, $t = 15$ s (∗) , $t = 35$ s (□), $t = 55$ s (◆), while the lines correspond to the column model using $K^* = 0.2$, $t = 15$ s (- - -), $t = 35$ s (-·-·-) and $t = 55$ s (· · ·). The green dashed line (- - -) corresponds to the case where $d_{e,max} = 1.2d_i$ and $K^* = 0.1$ was used to calculate $g(d_i)$. In (*b*) we compare the resulting breakup frequency for the two cases, $d_{e,max} = 1.2d_i$(- - -) and $d_{e,max} = d_i$(——).

velocity and dissipation rate was well characterized and found to obey classic scalings of a turbulent round jet,

$$\frac{U_0}{U(x)} = \frac{1}{C_u}\left(\frac{x}{D_j} - \frac{x_0}{D_j}\right), \qquad \frac{\epsilon D_j}{U_0^3} = C\left(\frac{x}{D_j} - \frac{x_0}{D_j}\right)^{-4}, \tag{2.27}$$

where $C_u = 4.08$ and $C = 36$ are empirical constants. The virtual origin $x_0/D_j = 5.47$ was found by fitting the experimental data with equation (2.27). The breakup and downstream evolution of oil droplets were tracked using digital image processing techniques[27]. The authors defined a characteristic droplet size d_{max} whose number density $n(d_{max})$ can only change due to its own breakup

Oil	d_{max}(mm)	We	ρ_d (kg/m^3)	μ_d (Pa s)	σ (N/m)
Heptane	1.9	10	684	5.00×10^{-4}	4.8×10^{-2}
Olive Oil	1.91	30	881	7.19×10^{-2}	2.0×10^{-2}
10 cSt silicone oil	1.92	20	936	9.70×10^{-3}	3.5×10^{-2}
50 cSt silicone oil	1.81	20	970	5.09×10^{-2}	3.7×10^{-2}

Table 2.1: Dispersed fluid properties.

but cannot increase due to breakup of other (larger) droplets. This condition isolates the effect of the breakup frequency on the evolution of the number density. Mathematically the evolution of the size distribution can be tracked using equation (2.1), where for the size d_{max} we can drop the first term in equation (2.2). Additionally for the quasi-one-dimensional steady state jet flow considered, we can write the PBE for the largest size as

$$\nabla_x \cdot [\boldsymbol{v}(d_{max}, \boldsymbol{x}) n(d_{max}, \boldsymbol{x})] = -g(d_{max}, \boldsymbol{x}) n(d_{max}, \boldsymbol{x}), \tag{2.28}$$

where $n(d_{max}, x) = N(d_{max}, \boldsymbol{x})/V_w$, with V_w being the volume of the interrogation window and $N(d_{max}, x)$ the total number of droplets measured in the window at x. The droplet velocity $\boldsymbol{v}(d_{max}, \boldsymbol{x})$ can be approximated by the local mean velocity of the turbulent jet, $U(x)$. Equation (2.28) can then be written for the number of droplets $N(d_{max}, x)$ as,

$$\frac{\mathrm{d}}{\mathrm{d}x}[U(x)\, N(d_{max}, x)] = -N(d_{max}, x) g(d_{max}, x). \tag{2.29}$$

The maximum diameter d_{max} represented the size where at least 80% of the volume of the distribution was contained in droplets smaller than d_{max}. The overall decay of $N(d_{max}, x)$ with downstream distance was found to be similar when this criterion was enforced, thereby ensuring that the evolution of the largest size class is being captured. In order to validate our model with the experiments, we solve equation (2.29) using a fourth-order explicit Runge-Kutta method (ode45 in MATLAB). Equation (2.16) is used to calculate the breakup frequency $g(d_{max}, x)$ with $K^* = 0.2$ for all the oils considered. A summary of the physical properties of the different oils used for the simulation along with the corresponding size d_{max} is provided in Table 2.1.

We compare the model predictions with the experimental data in Figure 2.7. We see that the model does a good job of capturing the decay of the number of droplets for the 50 cSt silicone oil and the olive oil cases. For heptane and 10 cSt silicone oil the predicted decay is too rapid and $K^* = 0.2$ appears not to be the optimal value, while $K^* = 0.1$ and $K^* = 0.15$ are seen to give better agreement with the data. We have not found any obvious parameter dependencies that could explain the different K^*. Single droplet breakup experiments could be used in order to better tune the model and determine whether weak dependency on system parameters exist (see Chapter 8) . For the rest of the thesis we use $K^* = 0.2$, which works well for majority of the cases considered.

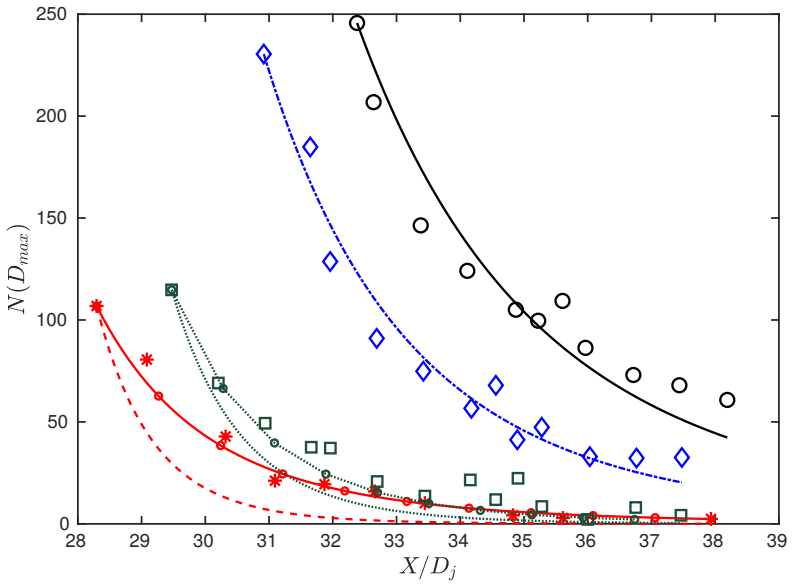

Figure 2.7: Evolution of the $N(d_{max})$ with downstream distance for the four different oils in 2.1. The symbols correspond to the experimental data of the different oils, 50 cSt Silicone oil (○), Olive oil (◇), 10 cSt Silicone oil (□) and Heptane (∗). The different lines correspond to the model, 50 cSt Silicone oil (——), Olive oil (-·-·), 10 cSt Silicone oil (· · ·) and Heptane (- - -) with $K^* = 0.2$. Also shown are the model for Heptane (—○—) with $K^* = 0.1$ and 10 cSt Silicone Oil (··○··) with $K^* = 0.15$.

2.4 Conclusions

We follow the general procedure of Konno et al.[50], Prince and Blanch[81] and Tsouris and Tavlarides[104] in which the breakup is modelled as due to collision of turbulent eddies with droplets. Previous models assumed the droplet size to be in the inertial range of turbulence and use Kolmogorov scaling (K41) for the velocity increment valid for the inertial range. For many applications the droplet size range can lie in the viscous subrange. We have thus proposed a model that includes the effect of the viscous range of scales of turbulence using a generalized structure function approach to characterize the eddy fluctuation velocity. The formulation contains an adjustable parameter K^* that has been fitted using experimental data. To reduce computational cost, we parameterize the breakup frequency in terms of the various (locally changing) nondimensional parameters, and provide practical fits that enable rapid calculation. The model is finally validated with an experiment of oil droplets injected in a turbulent jet[27] where we find that $K^* = 0.2$ works well for majority of the cases considered.

Chapter 3

Large Eddy Simulations : Methods

Large eddy simulations capture the large and intermediate scale turbulent motions (depending on the grid resolution), and only require modeling of the unresolved subgrid-scale turbulence effects. While the cost of LES is higher than Reynolds-Averaged Navier–Stokes simulations, LES provides the ability to resolve unsteady spatially fluctuating phenomena at least down to scales on the order of the grid scale. In this thesis we will highlight this strength of LES in the context of simulations of the evolution and transport of size distributions of polydispersed oil droplets in water. The LES equations used to describe the large scales of a turbulent jet are discussed in Section 3.1.

In this thesis, high-fidelity large-eddy simulations use an inhouse LES code

(LESGO). Initially adapted from the LES code of Albertson and Parlange[3], the code has since been used to simulate air pollutant transport in urban canopies[103], flow over fractal trees[20], wind farms[13], heat entrainment under arctic sea ice[84] and buoyant plumes from oil blowouts[112,113]. In Section 2.1 we describe the fast Eulerian method used to solve for the concentration field.

3.1 LES Governing Equations

3.1.1 Filtered Navier-Stokes Equations

The jet and surrounding fluid are governed by the three–dimensional incompressible filtered Navier–Stokes equations with a Boussinesq approximation for buoyancy effects:

$$\nabla \cdot \tilde{\boldsymbol{u}} = 0, \tag{3.1}$$

$$\frac{\partial \tilde{\boldsymbol{u}}}{\partial t} + \tilde{\boldsymbol{u}} \cdot \nabla \tilde{\boldsymbol{u}} = -\frac{1}{\rho_c}\nabla \tilde{P} - \nabla \cdot \boldsymbol{\tau}^d + \left(1 - \frac{\rho_d}{\rho_c}\right) \sum_i (V_{d,i}\tilde{n}_i) g \boldsymbol{e}_3 + \tilde{F}\boldsymbol{e}_3. \tag{3.2}$$

A tilde denotes a variable resolved on the LES grid, $\tilde{\boldsymbol{u}}$ is the filtered fluid velocity, ρ_d is the density of the droplet, ρ_c is the carrier fluid (seawater) density, $V_{d,i} = \pi d_i^3/6$ is the volume of a spherical oil droplet of size d_i, $\boldsymbol{\tau} = (\widetilde{\boldsymbol{u}\boldsymbol{u}} - \tilde{\boldsymbol{u}}\tilde{\boldsymbol{u}})$ is the subgrid-scale stress tensor with deviatoric part, $\boldsymbol{\tau}^d = \boldsymbol{\tau} - [tr(\boldsymbol{\tau})/3]\boldsymbol{I}$ where $\boldsymbol{I}$ is the identity tensor, $\tilde{P} = \tilde{p}/\rho_c + tr(\boldsymbol{\tau})/3 + |\tilde{\boldsymbol{u}}|^2/2$ is the pseudo-pressure, with $\tilde{p}$ being the resolved dynamic pressure, $\tilde{F}$ is a locally acting body force used to

generate a coarse turbulent jet, and e_3 is the unit vector in the vertical direction.

In order to solve equation (3.2), a closure model for the subgrid stress tensor $\boldsymbol{\tau}_{ij}^d$ is needed. We use an eddy viscosity based model where the stress as represented as :

$$\boldsymbol{\tau}_{ij}^d = -2\nu_T \tilde{S}_{ij}, \tag{3.3}$$

where $\tilde{S}_{ij}$ is the filtered strain rate tensor

$$\tilde{S}_{ij} = \frac{1}{2}\left(\frac{\partial \tilde{u}_i}{\partial x_j} + \frac{\partial \tilde{u}_j}{\partial x_i}\right) \tag{3.4}$$

The problem is now reduced to finding a suitable model for the eddy viscosity ν_T. In this thesis we use the Lilly-Smagorinsky eddy viscosity model[94], where the eddy viscosity is given by

$$\nu_T = C_s^2 \Delta^2 |\tilde{S}|; \qquad |\tilde{S}| = 2\tilde{S}_{ij}\tilde{S}_{ij} \tag{3.5}$$

where C_s is the Smagorinsky coefficient and Δ is the filter width. In this thesis we adopt a dynamic approach to prescribe the eddy viscosity C_s. This eliminates the need of an adjustable parameter and dynamically determines the Smagorinsky coefficient. The dynamic model uses multiple filter sizes, Δ to determine the Smagorinsky coefficient in the resolved scales of the flow[33,10]

We use the Lagrangian-averaged scale-dependent (LASD) model[10] which accounts for spatial inhomogeneity to dynamically determine C_s. The LASD model has been validated for flows over homogeneous and heterogeneous rough surfaces[10], stable and unstable atmospheric boundary layer simulations[48] and in wind farm simulations[109]. The LES code with the LASD model has been used successfully in a number of prior LES studies[103,48,13,112,114].

3.1.2 Filtered Concentration Equation

The droplet size range is discretized into a finite number of classes. The number concentration for each droplet size is described by a continuous field, $\tilde{n}_i$ whose evolution follows the equation :

$$\frac{\partial \tilde{n}_i}{\partial t} + \nabla \cdot (\tilde{\boldsymbol{v}}_i \tilde{n}_i) + \nabla \cdot \boldsymbol{\pi}_i = \widetilde{S}_{b,i} + \widetilde{q}_i, \quad i = 1, 2..N. \tag{3.6}$$

$\tilde{n}_i$ is the resolved number density of the droplet of size d_i The filtered version of the transport equation for the number density $\widetilde{n}_i(\boldsymbol{x}, t; d_i)$ is given by equation (3.6). The term $\boldsymbol{\pi}_i = (\widetilde{\boldsymbol{v}_i n_i} - \tilde{\boldsymbol{v}}_i \tilde{n}_i)$ is the subgrid-scale concentration flux of oil droplets of size d_i (no summation over i implied here) and $\widetilde{q}_i$ denotes the injection rate of droplets of diameter d_i.

The SGS scalar flux $\boldsymbol{\pi}_i$ is modelled using an eddy-diffusion SGS model. We use the approach of prescribing a turbulent Schmidt/Prandtl number, $Pr_\tau =$

$Sc_\tau = 0.4$[114] (not to be confused with the RANS-level diffusivity and Schmidt number used in the previous section for the 1D model). The SGS flux can be parameterized as $\pi_{n,i} = -(\nu_\tau / Sc_\tau)\nabla \tilde{n}_i$. With the evolution of oil droplet concentrations being simulated, their effects on the fluid velocity field are modelled and implemented in (3.2) as a buoyancy force term (the last term on the right-hand side of the equation) using the Boussinesq approximation. A basic assumption for treating the oil droplets as a Boussinesq active scalar field being dispersed by the fluid motion is that the volume and mass fractions of the oil droplets are small within a computational grid cell.

In the fast Eulerian method[31], the droplet velocity is modeled as a function of the droplet timescale. This saves on computational cost as separate momentum equations need not be solved for the velocity of each droplet size. The validity of the method requires the both small Stokes number and small volume fraction.

The droplet transport velocity $\tilde{\boldsymbol{v}}_i$ is calculated by an expansion in the droplet time scale $\tau_{d,i} = (\rho_d + \rho_c/2)d_i^2/(18\mu_f)$[31]. The expansion is valid when $\tau_{d,i}$ is much smaller than the resolved fluid time scales, which requires us to have a grid Stokes number $St_{\Delta,i} = \tau_{d,i}/\tau_\Delta \ll 1$, where τ_Δ is the turbulent eddy turnover time at scale Δ. The transport velocity of droplets of size d_i, $\tilde{\boldsymbol{v}}_i$, is given by[31]

$$\tilde{\boldsymbol{v}}_i = \tilde{\boldsymbol{u}} + w_{r,i}\boldsymbol{e}_3 + (R-1)\tau_{d,i}\left(\frac{D\tilde{\boldsymbol{u}}}{Dt} + \nabla\cdot\boldsymbol{\tau}\right) + O(\tau_{d,i}^{3/2}), \tag{3.7}$$

where $w_{r,i}$ is the droplet terminal (rise) velocity, $\boldsymbol{e}_3$ is the unit vector in the vertical direction, and $R = 3\rho_c/(2\rho_d + \rho_c)$ is the acceleration parameter.

In the formulation of the droplet velocity described by equation (3.7) the Stokes number is assumed to be small. For $St > 1$, additional higher order terms need to be incorporated to provide a complete description. The velocity due to the Saffman lift force has been neglected in equation (3.7) and can be written as[31]

$$\tilde{\mathbf{v}}_m = \frac{3J_\infty}{2\pi^2}\sqrt{\frac{3R\tau_d}{|\tilde{\boldsymbol{\omega}}|}}\tilde{\boldsymbol{\omega}} \times (-w_r \boldsymbol{e}_3), \tag{3.8}$$

where $\tilde{\boldsymbol{\omega}}$ is the vorticity, $J_\infty = 2.255$ and τ_d is the droplet response timescale that can be related to the rise velocity

$$\tau_b = \frac{w_r}{(R-1)g} \tag{3.9}$$

The migration velocity compared to the droplet rise velocity can be written as :

$$\frac{|\tilde{\mathbf{v}}_m|}{w_r} \sim \frac{3J_\infty\sqrt{3R}}{2\pi^2}\sqrt{\tau_b|\tilde{\boldsymbol{\omega}}|} \sim 0.6\sqrt{\frac{\tau_b}{\tau_\Delta}}, \tag{3.10}$$

where $R \approx 1$ (for oil droplets) and τ_Δ is the eddy turnover time of the resolved eddies in LES and can be estimated as

$$\tau_\Delta = \frac{l}{w'}\left(\frac{\Delta}{l}\right)^{2/3}, \tag{3.11}$$

where w' is the r.m.s of the velocity fluctuation and l is the integral length-scale of the jet (related to the half-width). The inertial velocity $|\tilde{\mathrm{v}}_m|/w_r \sim$ O(0.1) and can be neglected for $St < 0.2$. In the simulations considered in this study the Stokes number, $St < 0.5$ except very near the nozzle exit. In Chapter 6 the Stokes number in the near nozzle region is $\sim$ O(1) for the largest droplet size. However the inertial migration velocity can be neglected as $|\mathrm{v}_m/\boldsymbol{u}| << 1$. In the self-similar region where the present study's focus lies and most results for velocity and concentration field are presented and analyzed, the Stokes number $St < 1$ even for the largest droplet sizes.

The term $\widetilde{S_{b,i}}$ in equation (3.6) represents the rate of change of droplet number density due to breakup and is modelled using equations (2.6) and (2.20) described in §2.1. The breakup rate g_i is evaluated using the fits presented in Appendix A and depend on the local Reynolds number expressed in terms of the local rate of dissipation. From the SGS model, the local rate of dissipation at the LES grid scale is given by

$$\epsilon(\boldsymbol{x}, t) = 2(c_s\Delta)^2|\tilde{S}|\tilde{S}_{ij}\tilde{S}_{ij}. \tag{3.12}$$

In implementing the model, when evaluating the filtered source term, we use the filtered parameters (e.g. grid-scale dissipation rate, etc.), that is to say, we assume $\widetilde{gn} \approx \tilde{g}\tilde{n}$, and further that $\widetilde{g(\epsilon, ..)} \approx g(\tilde{\epsilon}, ..)$. This means that we

neglect the subgrid correlations between locally fluctuating dissipation rates at scales smaller than the grid scale and subgrid fluctuations in the concentration field. The neglect of such subgrid-scale contributions to the modelled source terms must be kept in mind, especially for applications at very high Reynolds numbers when the Kolmogorov scale is much smaller than the grid scale where further refinements and new subgrid models may be required.

3.2 Numerical Treatment

The numerical discretization for the velocity field used in the LES combines a pseudo-spectral representation in the horizontal directions (x and y) and a second-order centered finite difference in the vertical direction (z). The second-order Adams-Bashforth method is used for time integration. The continuous fields are represented by a discrete mesh with N_x nodes in the x-direction, N_y nodes in the y-direction, and N_z nodes in the z-direction with the total domain size $L_x \times L_y \times L_z$. The LES employs uniform grid spacing in each direction, such that the grid-spacing is defined as

$$\Delta_i = L_i/N_i, \tag{3.13}$$

where the subscript i denotes the Cartesian co-ordinate directions (x, y and z). The locations for storing the primitive variables in physical space of a node

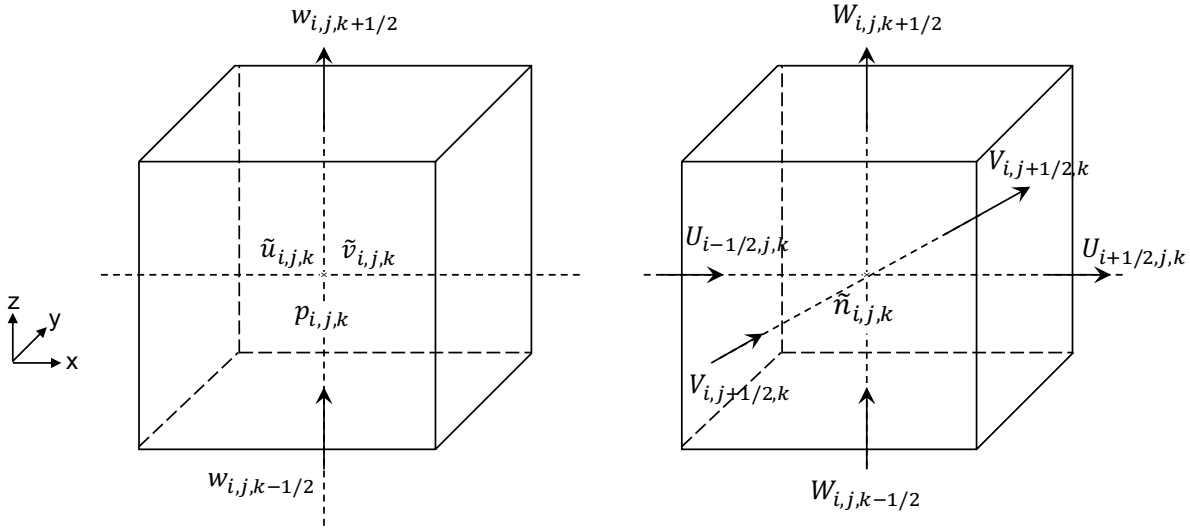

Figure 3.1: Primitive variables with respect to staggered mesh. Left : Variables on the pseudo-specral grid. Right : Finite volume grid. (Adapted from Chamecki et al.[14].

indexed with (i, j, k) in each dimension are shown in Figure 3.1.

The horizontal components of velocity ($\tilde{u}$ and $\tilde{v}$), pressure ($\tilde{p}$) and scalar concentration ($\tilde{C}$) are located at the center of the grid node. The vertical component of the velocity (w) is placed on a staggered grid. All variables represent nodal values of the fields. As the horizontal directions are assumed to be periodic (in the pseudo-spectral formulation), a discrete variable can be represented by its Fourier series as

$$\tilde{u}_m(x, y, z) = \sum_{k_x} \sum_{k_y} \hat{u}_m(k_x, k_y, z) e^{i(k_x x + k_y y)} \tag{3.14}$$

where tilde denotes a variable resolved on the LES grid, $\hat{u}_m$ is the complex Fourier amplitude, k_x and k_y are the wavenumbers in the x and y directions

with summations ranging over the integer numbers $-N_x/2+1 \leq k_x \leq N_x/2$, and $-N_y/2+1 \leq k_y \leq N_y/2$. Horizontal spatial derivatives are calculated in Fourier space, while vertical derivatives are calculated through finite differences. The x and y derivative of equation (3.14) can be written as :

$$\frac{\partial \tilde{u}_m(x,y,z)}{\partial x} = \sum_{\substack{k_z \\ k_x \neq N_x/2, k_y \neq N_y/2}} \sum_{k_y} (\hat{u}_m(k_x,k_y,z) i k_x)\, e^{i(k_x x + k_y y)} \tag{3.15}$$

$$\frac{\partial \tilde{u}_m(x,y,z)}{\partial x} = \sum_{\substack{k_z \\ k_x \neq N_x/2, k_y \neq N_y/2}} \sum_{k_y} (\hat{u}_m(k_x,k_y,z) i k_y)\, e^{i(k_x x + k_y y)}, \tag{3.16}$$

where the summation is over all wavenumbers except the Nyquist wavenumbers. The horizontal derivatives are calculated at the same spatial location as the variable (uv-nodes). The vertical derivatives are calculated using finite differences on the uv-node. The staggering ensures that all the derivatives needed to calculate the divergence are calculated at the same location. The vertical derivative can be written as :

$$\frac{\partial \tilde{u}_m(x,y,z)}{\partial z} = \frac{\tilde{u}_m(x,y,z+\Delta/2) - \tilde{u}_m(x,y,z-\Delta/2)}{\Delta z} \tag{3.17}$$

Although horizontal derivatives are calculated in the Fourier domain, products between variables are calculated in physical space to avoid calculating expensive convolutions in the Fourier domain. Aliasing errors arise as we attempt to resolve the product of two variables with N modes, while each variable

itself is resolved using N modes. The variables are dealiased by padding and subsequent truncation. Fourier transforms are evaluated using $3N/2$ points and then truncated to N nodes. The transform calculated using $3N/2$ modes results in aliasing between $3N/2 \leq k \leq 2N$ to the wavenumbers between N and $3N/2$ that the subsequent truncation removes.

The concentration equation is solved using a finite-volume algorithm with the center of the volume (C_{ijk}) located on the uv-node (3.1). The advection term is computed using the SMART (Sharp and Monotonic Algorithm for Realistic Transport) scheme[32]. The finite volume grid used for the concentration field is placed so that the center of the volume corresponds to the uv-node (where the concentration C_{ijk} is stored. As shown in Figure 3.1 the velocity on the spectral grid is denoted by (u, v, w) while the face velocities are denoted by (U, V, W). The horizontal face velocities are obtained by interpolation, whereas the vertical W face velocity is directly available due to the staggered grid arrangement. The conservation of mass (equation (3.2) is enforced using spectral (non-local) derivatives. In general the velocity field interpolated on the surfaces of the control volume will not satisfy the divergence free condition. We use the conservative interpolation scheme developed by Chamecki et al.[14] in order to circumvent this problem. The conservative interpolation method uses the spectral derivatives instead of the velocity along with an integration scheme consistent with the finite volume discretization. The spectral derivatives are known at

the center of the control volume and satisfy the conservation of mass exactly :

$$\left(\frac{\partial \tilde{u}}{\partial x}\right)^{spec.} + \left(\frac{\partial \tilde{v}}{\partial y}\right)^{spec.} + \frac{\tilde{w}(i,j,k+1/2) - \tilde{w}(i,j,k-1/2)}{\Delta z} = 0 \tag{3.18}$$

Using a centered second order discretization, the interpolated velocities can be obtained from :

$$\frac{U_{i+1/2,j,k} - U_{i-1/2,j,k}}{\Delta x} = \left(\frac{\partial \tilde{u}}{\partial x}\right)^{spec.}, \tag{3.19}$$

$$\frac{V_{i,j+1/2,k} - V_{i,j-1/2,k}}{\Delta y} = \left(\frac{\partial \tilde{v}}{\partial y}\right)^{spec.}. \tag{3.20}$$

In equation (3.19) and (3.20) the neighbouring indices are coupled for each (i,j) and a bi-diagonal matrix system needs to be solved to obtain the face velocities. One obtains N_y decoupled systems of N_x equations for the U elements and N_x systems with N_y equations for the V elements. The system is underdetermined since equation from the periodicity is a linear combination of two other equations. One cannot fully determine the velocity field by imposing only the derivatives everywhere. Therefore, we impose the equality condition for the average velocity along a line between original field (u, v) and interpolated field (U, V) as an additional equation. The system for the (j,k) line of the U

velocity can be written as :

$$\begin{bmatrix} -1 & 1 & 0 \dots & 0 & 0 \\ 0 & -1 & 1 \dots & 0 & 0 \\ 0 & 0 & -1 \dots & 0 & 0 \\ \dots & \dots & \dots \dots & \dots & \dots \\ 0 & 0 & 0 \dots & -1 & 1 \\ 1 & 1 & 1 \dots & 1 & 1 \end{bmatrix} \begin{pmatrix} U_{1-1/2,j,k} \\ U_{2-1/2,j,k} \\ U_{3-1/2,j,k} \\ \dots \\ U_{N_x-1-1/2,j,k} \\ U_{N_x-1/2,j,k} \end{pmatrix} = \begin{bmatrix} (\Delta x) \left(\frac{\partial \tilde{u}}{\partial x}\right)^{spec.}_{1,j,k} \\ (\Delta x) \left(\frac{\partial \tilde{u}}{\partial x}\right)^{spec.}_{2,j,k} \\ (\Delta x) \left(\frac{\partial \tilde{u}}{\partial x}\right)^{spec.}_{3,j,k} \\ \dots \\ (\Delta x) \left(\frac{\partial \tilde{u}}{\partial x}\right)^{spec.}_{N_x-1,j,k} \\ \sum_i \left(\tilde{u}_{i,j,k}\right) \end{bmatrix}, \tag{3.21}$$

and similarly for $V_{i,j-1/2,k}$. The solution for the system $Ax = b$ can be implemented efficiently as all the matrices for each velocity component are the same, and the inverse of the matrix A depends only on N.

$$A^{-1} = \begin{bmatrix} (1-N) & (2-N) & (3-N) \dots & (N-1-N) & 1 \\ 1 & (2-N) & (3-N) \dots & (N-1-N) & 1 \\ 1 & 2 & (3-N) \dots & (N-1-N) & 1 \\ \dots & \dots & \dots \dots & \dots & \dots \\ 1 & 2 & 3 \dots & (N-1-N) & 1 \\ 1 & 1 & 1 \dots & (N-1) & 1 \end{bmatrix}. \tag{3.22}$$

The face velocities can be obtained by simply calculating the spectral derivatives and assembling the vectors on the right-hand side of equation (3.21) The required velocity components are then obtained by multiplying the vectors by

the matrix A^{-1} given above.

3.3 Generating a Turbulent Jet via Body Forcing

The injected jet is modelled in the LES framework using a locally applied vertically upward pointing body force $\tilde{F}$ (3.2, since at the LES resolution used in the simulation it is not possible to resolve the small-scale features of the injection nozzle. To minimize the effect of Gibbs phenomena, the applied force is spatially smoothed in the x and y directions using a super-Gaussian smoother defined as

$$\tilde{G}(x,y) = F\left(A\exp\left[-\left(\frac{(x-x_p)^2+(y-y_p)^2}{2\sigma^2}\right)^p\right]\right) \tag{3.23}$$

where x_p and y_p is the source location of the applied forcing F, p is the order of the super-Gaussian function and A is a suitable normalization constant ensuring that $\int \tilde{G}(x,y)\mathrm{d}x\mathrm{d}y = F$. The value of the exponent determines the "smoothness" of the forcing. A values of $p = 2$ results in a Gaussian distribution, whereas a large value results in a top hat profile. Through trial-and-error we find a value of $p = 5$ to be sufficient as a compromise between locality (large p) and smoothness (small p). The forcing is analogous to a body force, accelerating fluid around the region where the force is applied resulting in an upward

injection of momentum. The resulting injection velocity of the jet is controlled by the strength of the imposed body force. A simple analysis using the inviscid Euler equation including the forcing $\tilde{F}$ would suggest that the injection velocity W_J scales as the square root of the applied force i.e $W_J \sim \sqrt{|F|}$.

Since the details of the nozzle cannot be resolved, the body force can be thought to be applied at a location downstream of the real nozzle, where the jet is expected to have grown to a scale at which the numerical grid is sufficient to resolve at least the mean velocity profile. It is important to validate whether the forcing method reproduces well known scalings for turbulent round jets in the far field. The main results for a round turbulent jet are : 1) the centerline velocity decays as a function of downstream distance with a known inverse power-law, 2) the half-width of the jet grows linearly as a function of downstream distance and 3) the far field of the jet is self-similar. Self-similarity implies that as the jet decays and spreads, the mean velocity profile changes, but the shape of the profile does not change[80]. We present a simulation of a coarse round turbulent jet generated using the forcing method, and validate the resulting velocity decay and jet growth with experimental data.

Let (x, y, z) be the coordinate directions and the corresponding velocity components denoted by (u, v, w). The simulation is performed in a rectangular box with dimensions $(L_x, L_y, L_z) = (1, 1, 2.5)\ m$ using a grid resolution of $(N_x, N_y, N_z) = (288, 288, 384)$. The simulation represents a turbulent jet with nozzle diameter

$D_J = 3\ mm$ and an injection velocity of $w_0 = 11.9m/s$. The injection velocity magnitude is controlled by the applied forcing. As the injection nozzle of the jet cannot be resolved by the grid resolution of the LES, the location of the forcing is chosen downstream of the nozzle at $z = 10\ D_J$ with the corresponding injection velocity of $w_0 = 7\ m/s$ (less than the original injection velocity due to the known decay of the velocity as a function of downstream distance). The jet is then simulated by marching equation (3.2) using a second-order Adams-Bashforth scheme with a timestep $\Delta t = 6 \times 10^{-5}$. Three-dimensional snapshots of the entire simulation domain are recorded every 350 timesteps for statistical analysis.

Taking advantage of the axisymmetric nature of the flow, statistics are calculated using a cylindrical coordinate system with z being the axial coordinate. The time averaging is supplemented with additional averaging over the angular θ direction. The axial velocity of the jet is known to follow the well known inverse power law (hyperbolic)[40,78] :

$$\frac{w_0}{w_0(z)} = \frac{1}{C_u}\left(\frac{z}{D_J} - \frac{z_0}{D_J}\right), \tag{3.24}$$

where C_u is the decay constant for the velocity, w_0 is the injection velocity and z_0 is the virtual origin of the jet.

The jet half-width $r_{1/2}$ is defined as the radial location where the velocity

has dropped to half the centerline value[80],

$$\langle \tilde{w}(z, r_{1/2}(z), 0) \rangle = \frac{1}{2} \langle \tilde{w}_0(z) \rangle, \tag{3.25}$$

where z is the distance downstream measured from the nozzle exit. Figure 3.2 examines the evolution of the centerline velocity $\langle \tilde{w}_0(z) \rangle$ and half-width $r_{1/2}$ as a function of downstream distance scaled by the nozzle diameter $D_J = 3\ mm$. The injection velocity $w_0 = 11.9$ ms^{-1} at $z = 0$ is used to scale the data. The inverse centerline velocity growth shown in Figure 3.2 follows the expected hyperbolic law (3.24) with a decay coefficient of $C_u = 6.3$ calculated from the slope of the curve. This is in good agreement with existing experimental[40,78] and numerical data[64]. The jet growth in the region between $z = 50\ D_J$ and $z = 300\ D_J$ is linear. The slope of the curve, $S = 0.097$ compares well with values obtained in the literature of $S \approx 0.1$[78,40]

We also document the radial distribution of velocity at different downstream locations, in Figure 3.3. As expected from theory, the velocity profiles show approximate collapse on self similar behavior when normalized by the centerline value and plotted as a function of the similarity coordinate $r/r_{1/2}$, the radial coordinate scaled by the jet half-width.

Additionally we plot the the constant eddy-viscosity similarity solution to be discussed later in this thesis (in equation (5.6) in Chapter 5). The LES

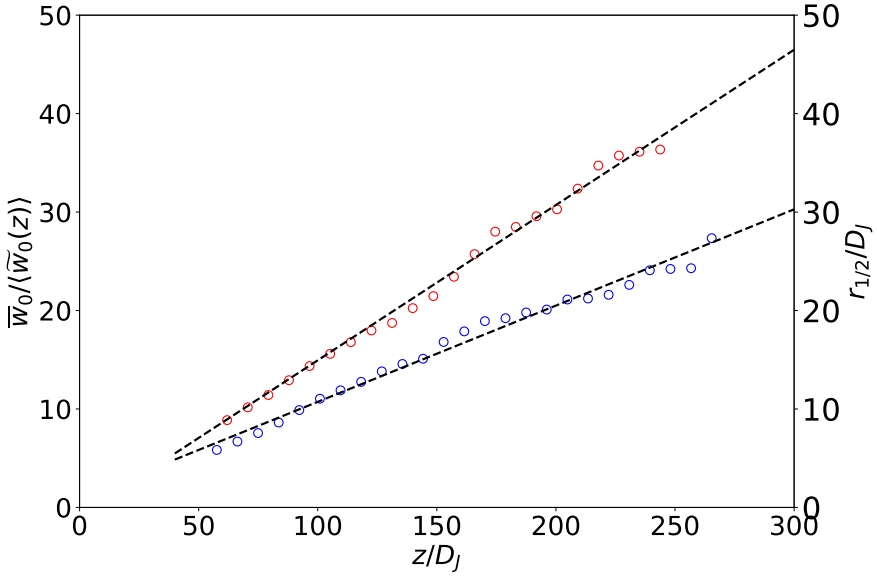

Figure 3.2: Downstream variation of half width of the jet (o, right axis) and the evolution of the inverse of the averaged centerline velocity (□, left axis) from LES. The linear fit to the data is depicted by the black dashed line (- - -).

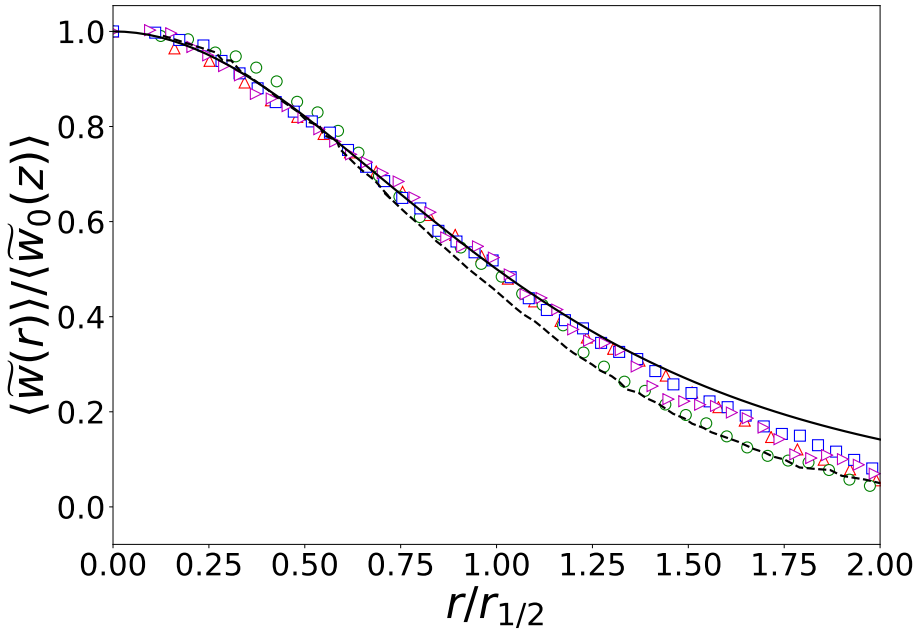

Figure 3.3: Downstream variation of half width of the jet (o, right axis) and the evolution of the inverse of the averaged centerline velocity (□, left axis) from LES. The linear fit to the data is depicted by the black dashed line (- - -).

data shows good agreement with the theoretical solution in the central part of the jet, whereas it falls below the constant eddy viscosity solution at larger r values, a behavior typically ascribed to the decreasing eddy viscosity in the outer parts of the jet[80]. The DNS result from Lubbers et al.[64], shown as the black dashed lines, agrees well with LES data also in the outer portions of the jet. The round turbulent jet generated using the local body force successfully reproduces the decay and spread of the jet along with the self-similar behaviour in the far-field.

We show the radial stress, $< v_r' v_r' >$, axial stress $< w'w' >$ and the turbulent transport $< w'v_r' >$ in Figure 3.4 along with the corresponding DNS data. The terms $< w'v_\theta' >$ and $v_r'v_\theta'$ are zero due to circumferential symmetry and absence of mean swirl. The primes denote fluctuating quantities obtained by subtracting the time averaged mean from the LES variables,

$$w' = \tilde{w} - \overline{\tilde{w}}. \tag{3.26}$$

Here the $\overline{()}$ denotes the time average. We see that the transport, $\langle w'v_r' \rangle$ is accurately captured by the LES. Due to the coarse grid resolution the normal stress $\langle w'w' \rangle$ is under-resolved as compared to the DNS. A possible explanation could be due to the fact that the vertical z direction is the finite difference direction in the code that is less accurate than the spectral (horizontal) directions. In-

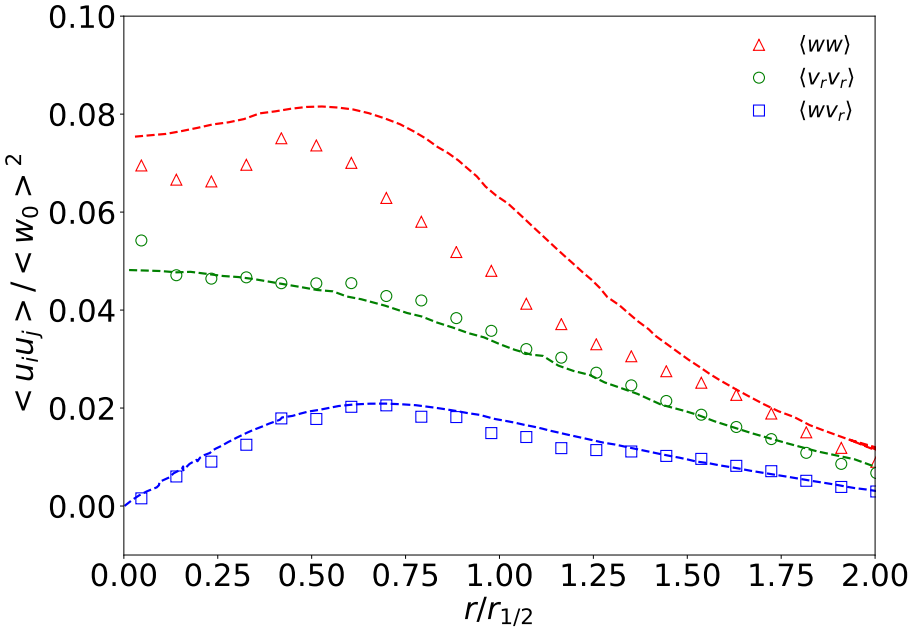

Figure 3.4: Downstream variation of half width of the jet (○, right axis) and the evolution of the inverse of the averaged centerline velocity (□, left axis) from LES. The linear fit to the data is depicted by the black dashed line (- - -).

creasing the grid resolution in the finite difference direction could increase the accuracy of the prediction.

3.4 Conclusions

In this chapter we presented the governing equations and the numerical methods that are used throughout this thesis. The droplet concentration is solved using an Eulerian formulation, with the droplet velocity modelled as a function of the droplet time scale. The breakup kernel is added as a source term to the droplet concentration equation and is solved using a population

balance equation. A round turbulent jet is generated in the LES using a locally acting upward body force. The decay of the centerline velocity and the growth of the jet is validated with experimental data and shows good agreement.

Chapter 4

LES of Polydisperse Droplets in a Jet-in-crossflow

A jet subjected to crossflow is an ideal surrogate for a deep water oil-spill. We describe here a method to combine LES with PBE's in modelling polydisperse oil plumes using the method of classes. The velocity and concentration field are described using the Eulerian-Eulerian LES method presented in Chapter 3 and the droplet breakup model (Chapter 2). We focus on the droplet breakup and transport occurring in regions away from the nozzle and compare the size distributions to experimental data of Murphy et al.[72]. In the present LES application, the nozzle details will not be resolved and thus the initial breakup mechanisms of oil into large droplets near the nozzle will be replaced by an appropriately chosen initial inflow condition of droplets of a given diam-

eter. (A method for developing more realistic inlet conditions is presented in Chapter 5). The focus of the study will be on comparing the size distributions far away from the nozzle with available experimental data, and to showcase the advantage of LES in being able to predict variability and intermittency of the size distribution and characteristic scales of the droplets. The content in this chapter is published in Aiyer et al.[1].

4.1 Simulation Setup

A sketch of the simulation domain is shown in Figure 4.1. We simulate a turbulent jet with imposed crossflow aiming to reproduce the experiments of Murphy et al.[72], who studied a turbulent oil jet in crossflow and measured droplet size distributions using a submersible digital inline holography technique. The experiments were carried out in a 2.5 m $\times 0.9$ m $\times 0.9$ m acrylic tank. The injection nozzle was connected to a carriage, driven by a stepper motor to generate desired crossflow speeds. The injection nozzle had a $D_{expt} = 4$ mm diameter orifice and was located at a distance of 0.14 m from the bottom of the tank. The oil was injected at a flow rate of $Q = 1.9$ L/min, (i.e. an injection velocity of $U_{j,expt} = 2.5$ m/s) and the carriage was towed at a speed of $U_c = 0.15$ m/s. In the experiments performed, the number of droplets was measured using a holocam fixed at the center of the tank in the horizontal plane, and at a dis-

tance of 0.47 m from the nozzle exit. It thus sampled different sections of the jet in the cross stream direction in the course of its evolution. Numbers of droplets in various size bins were measured at two times, at $t = 3.4$ s and $t = 6.9$ s. Additionally, the total oil distribution calculated by summing over five time measurements was recorded. As the nozzle in the experiments moved with a constant speed of 0.15 m/s, this corresponds to a downstream location of measurement at $x = 0.76$ m and $x = 1.3$ m respectively, in a frame moving with the jet nozzle (as will be done in the simulation). The total oil concentration at the measurement location height corresponds to the sum of the number of droplets measured as a function of downstream distance. In the experiments, the droplet size distributions were measured in 3 realizations of the experiments, hence the resulting size distribution and droplet concentrations were not fully statistically converged but the shape of the size distribution (relative size distribution) was well captured in the measurements.

As shown in Figure 4.1, the simulations are performed in a rectangular box of size $(L_x, L_y, L_z) = (2, 0.781, 1)$ m in which the jet is stationary but a constant inflow (crossflow) velocity is prescribed. The domain size is chosen to mimic the experimental setup and the length is sufficiently large to capture the complete turning of the jet. The crossflow is imposed along the x direction while the jet is pointed in the z direction. In order to handle the inflow and outflow conditions at the two boundaries in the x direction within the code that uses

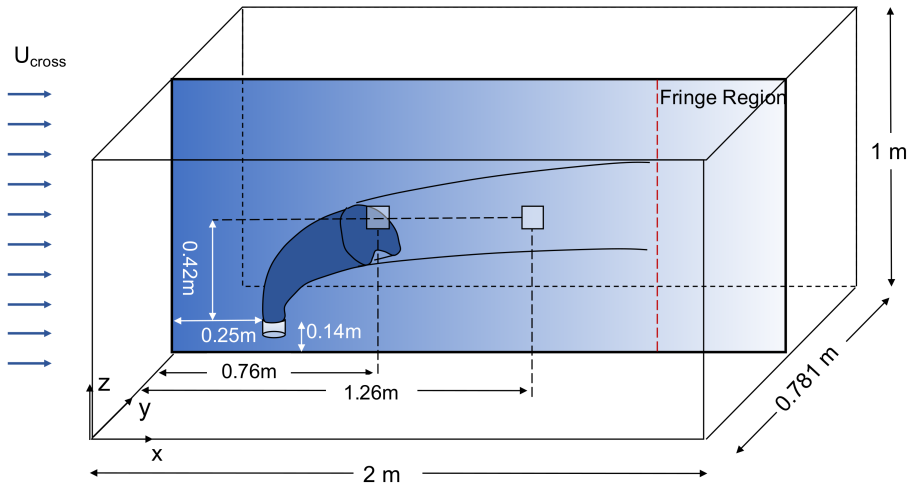

Figure 4.1: Sketch of the simulation domain and dimensions.

a Fourier-series based pseudo-spectral method, we specify a fringe zone that starts at $x = 1.666$ m, which damps out the velocity towards the inflow value. The simulations use a grid with $N_x \times N_y \times N_z = 384 \times 150 \times 384$ points for spatial discretization, and a timestep $\Delta t = 0.0002$ s for time integration. The resolution in the horizontal directions is $\Delta x = \Delta y = 5.2$ mm, and is $\Delta z = 2.6$ mm in the vertical direction for the finite difference method. Since the latter can be regarded as requiring about twice as much resolution for the same accuracy, we regard the overall numerical resolution to be about 5.2 mm. The injected jet is modelled in the LES using a locally applied vertically upward pointing body force, since at the LES resolution used in the simulation it is not possible to resolve the small-scale features of the injection nozzle. We choose to position the body force at a location where the experimental jet is expected to have achieved the half-width equal to the simulated jet's inflow radius, that is we re-

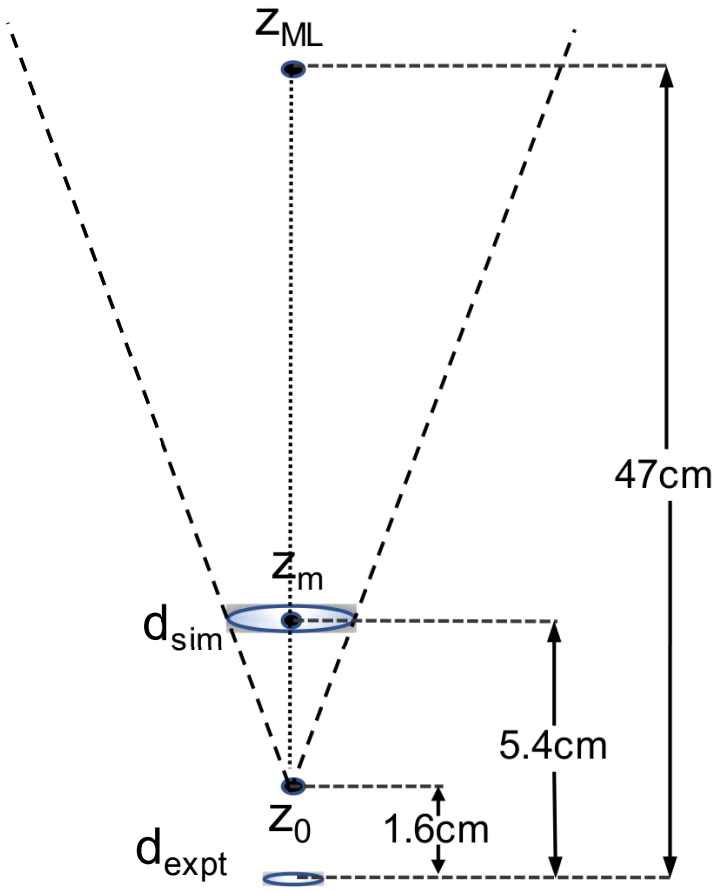

Figure 4.2: Sketch depicting the nozzle placement in LES (at vertical position $z_m = 54$ mm downstream of the experimental nozzle), the virtual origin of the experiment (assumed to be at $z_0 = 16$ mm $= 4d_{expt}$ downstream of the nozzle), and the measurement location (at a height of $z_{ML} = 470$ mm above the experimental nozzle position - in the experiment with cross-flow, there is additional displacement in the horizontal direction).

quire that $r_{1/2,expt} = d_{sim}/2$. The applied force is spatially smoothed in a region over three grid points in x, y and z using a super-Gaussian smoother (of order 5 and width $\sigma_G = \Delta x$) centered at z_m as shown by the sketch 4.2. We recall that $r_{1/2,expt}(z_m) = S(z_m - z_0)$, where z_0 is the virtual origin of the experimental nozzle. Using the value $d_{sim} = 7.8$ mm found above, we solve for $z_m - z_0$ and find $z_m - z_0 = d_{sim}/(2S) = 38.2$ mm, i.e. we apply the force 38.2 mm above the location of the real nozzle's virtual origin. The last parameter to determine is the jet centerline velocity, $U_{j,sim}$, at location $z = z_m$. The simulated injection jet velocity will be set equal to the experimental centerline velocity at that location, thus reproducing the mean flow of the jet as the most basic condition to be met at that location, where the LES grid resolution is just sufficient to resolve a jet's mean velocity profile. Using the classical scaling, the centerline velocity at z_m in the experiment may be obtained by

$$U_{0,expt}(z_m) = \frac{U_{j,expt}\, B\, d_{expt}}{z_m - z_0}. \tag{4.1}$$

Setting $U_{j,sim} = U_{0,expt}(z_m)$ and replacing $z_m - z_0 = r_{1/2,expt}/\,S = d_{sim}/(2S)$ we obtain

$$U_{j,sim} = \frac{2\,S\,U_{j,expt} B\, d_{expt}}{d_{sim}}. \tag{4.2}$$

Substituting $d_{sim} = 7.8$ mm, $S = 0.102$, $B = 6$ and $U_{j,expt} = 2.5$ m/s we can

calculate $U_{j,sim} \approx 1.6$ m/s. The body force magnitude is adjusted in the LES so as to achieve this value of the maximum velocity in the region where the body force is applied. We note that the magnitude of the velocity is lower than that in the experiment owing to the fact that the centerline velocity has already decayed at the simulated injection point. A uniform crossflow of $U_{cross} = 0.15$ m/s is imposed at the inflow boundary in order to simulate a jet in crossflow. The droplet number density fields are initialized to zero everywhere. Oil droplets of size $d = 1$ mm are injected at the jet source after a delay of 1 s to allow the flow to be established. The number density transport equation for the bin corresponding to the largest droplets ($i = N_d$ with $d_i = 1$ mm) contains a source term on the RHS which represents injection with a specified volume flow rate that matches the experimental value of Q= 1.9 L/min as in Murphy et al.[72]. The source is distributed over two grid points in the z direction with weights 0.25 and 0.75 and over three grid points in the x and y directions centered at $x = 0.245$ m, $y = 0.385$ m with weights 0.292 for the center and 0.177 for the neighbouring points. The physical properties of the oil and the simulation parameters are given in tables 4.1 and 4.2. The Weber number (We) has been calculated using the near nozzle dissipation $\langle\epsilon\rangle = 30$ m^{2}s^3 and the injection droplet size $d = 1$ mm.

The jet in crossflow is simulated for a total of 26 s, corresponding to 13×10^4 timesteps. The oil droplets are released after $t = 1$ s giving sufficient time for

ρ_d (kg/m^3)	ν_d (m^2/s)	σ (N/m)	ρ_c (kg/m^3)	Γ
864	1.02×10^{-5}	1.9×10^{-2}	1018.3	**10.5**

Table 4.1: Physical properties of fluids used in the simulation.

$Re = \frac{U_J D_J}{\nu_c}$	$We = \frac{2\rho_c \langle\epsilon\rangle^{2/3} d^{5/3}}{\sigma}$	U_J (m/s)	D_J (mm)	D_{expt} (mm)
12500	10	1.6	7.8	4

Table 4.2: Simulation parameters.

the jet to become fully turbulent. Starting from $t = 12$ s, 350 three-dimensional snapshots of the entire simulation domain are recorded for statistical analysis with an interval of 0.04 s (200 timesteps) between each snapshot.

4.2 Instantaneous and Mean Concentration Distributions

We plot a volume rendering of an instantaneous snapshot of the $20\ \mu m$-droplet plume in Figure 4.3. The concentration of the $1000\ \mu m$ plume is shown using solid spheres on the same plot for visualization purposes. Qualitatively we can observe that the upper plume boundary for the $1000 \mu; m$ droplets is higher than the $20\ \mu m$ plume due to a larger rise velocity.

In Figure 4.4 we show contour plots of instantaneous number density in logarithmic scale ($\log_{10}(\tilde{n}_i)$) for four representative droplet sizes on the mid y-

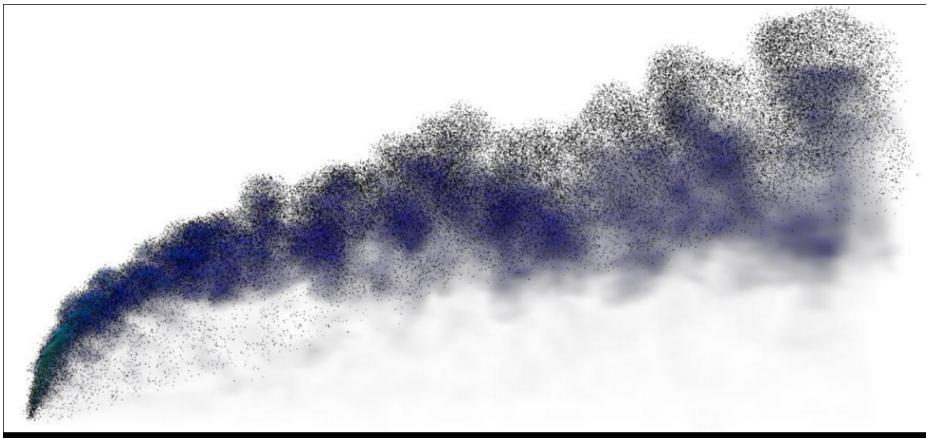

Figure 4.3: Volume rendering of an instantaneous snapshot of the $20\mu\ m$ droplet plume with the $1\ mm$ droplets shown as solid spheres.

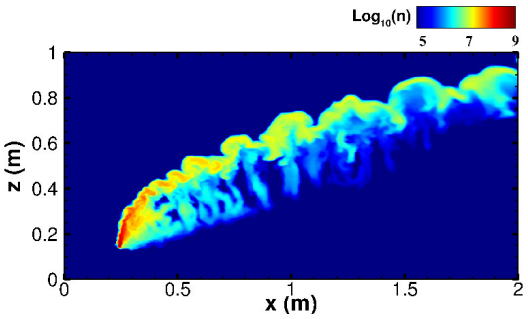

(a) $d = 1000\ \mu$m.

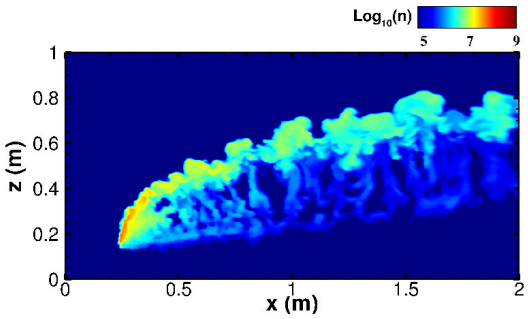

(b) $d = 432\ \mu$m

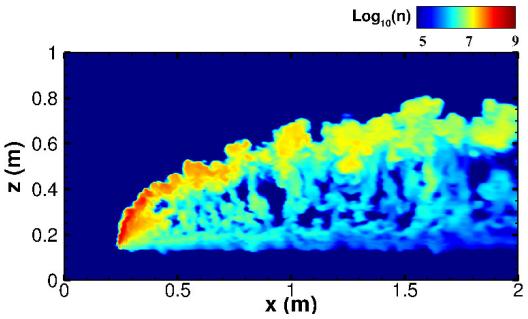

(c) $d = 107\ \mu$m

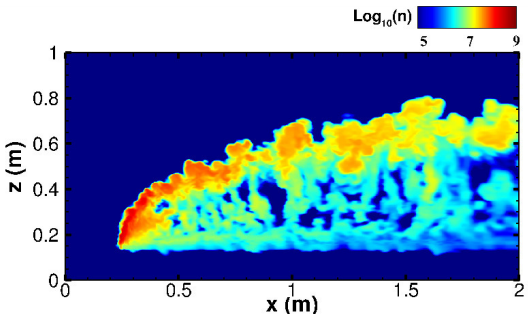

(d) $d = 20\ \mu$m

Figure 4.4: Contour plots of instantaneous concentration fields at the midplane of the jet. The concentration is plotted in logarithmic scale. (a) is the concentration of the droplet of size $1000\ \mu$m, (b) for $d = 432\ \mu$m, (c) for $d = 107\ \mu$m, and (d) for $d = 20\ \mu$m.

plane as function of x and z. The largest droplet size is in the top left panel and the smallest one is in the bottom right. The spatial distributions of the number densities for different droplet sizes show distinct qualitative behaviours. The plumes of the smaller droplets appear significantly more dispersed than those of the larger sizes, showing some presence also in the bottom portions of the domain and clear effects of vertical column vortices. The largest droplets are more concentrated towards the upper portions of the overall plume (consisting of all size bins) as expected from their larger rise velocity.

Figure 4.5 shows the time averaged number density fields of the various droplet sizes at the mid y-plane. The maximum concentration for each bin size occurs in the near-nozzle region where the energy dissipation is also the highest and thus the breakup rate is fastest. The larger droplets are more buoyant, having a larger rise velocity and thus their average plume has a higher inclination angle with respect to the crossflow direction.

4.3 Relative Droplet Size Distributions

To make a quantitative comparison with the experiments we compare droplet size distributions measured at the two cross-stream locations indicated in Figure 4.1. The measurement locations are centered at a vertical distance of 42 cm above from the nozzle (see Appendix B). The width of bins used in the experi-

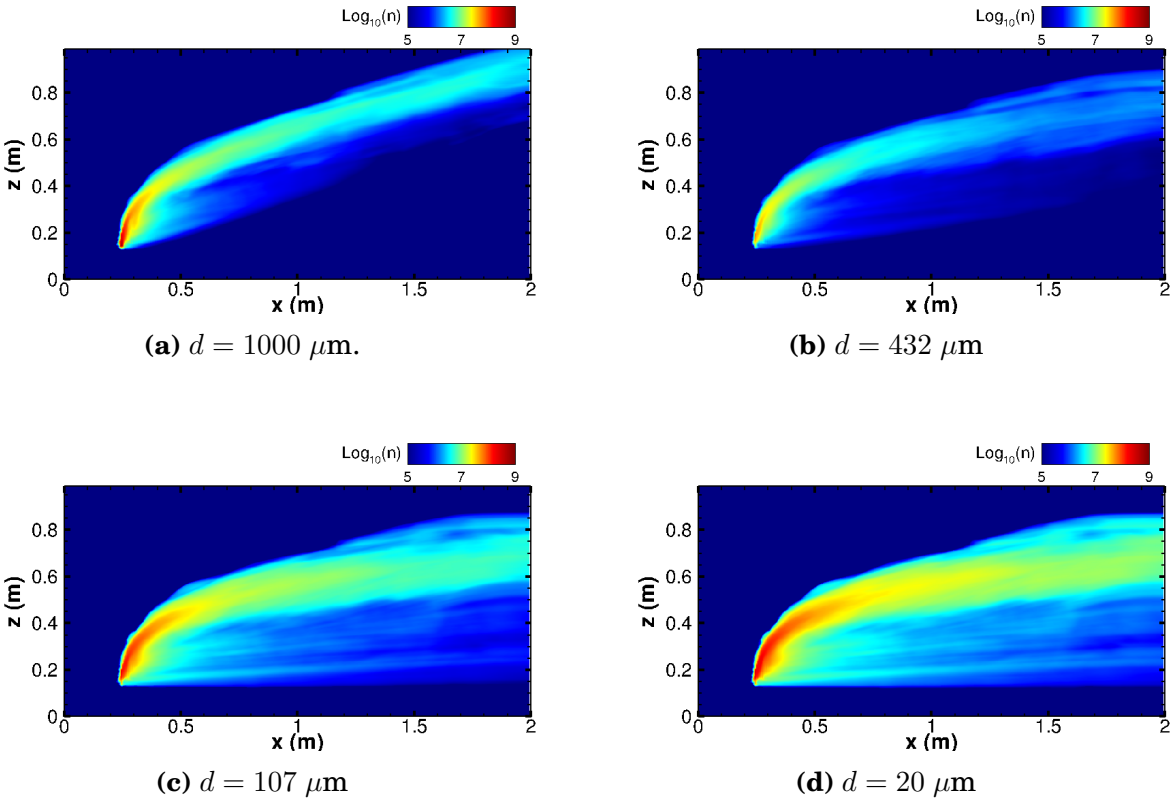

(a) $d = 1000$ μm.

(b) $d = 432$ μm

(c) $d = 107$ μm

(d) $d = 20$ μm

Figure 4.5: Time averaged concentration fields at the midplane of the jet plotted in logarithmic scale. Panel (a) is the concentration of droplets of size 1000 μm, (b) shows the concentration field for $d = 432$ μm, (c) shows the concentration field for $d = 107$ μm, and (d) shows the concentration field for $d = 20$ μm.

ments are not necessarily the same as that used in the simulation. In order to make comparisons with the experiments, we define a number density normalized by the bin width, i.e.

$$n_i^* = \frac{\tilde{n}_i}{\delta d_i}, \tag{4.3}$$

here $\tilde{n}_i$ is the number of droplets per m^3 of fluid in bin i, $\delta d_i = \frac{1}{2}(d_{i+1} - d_{i-1})$ for $i = 2$ to 14, $\delta d_1 = d_2 - d_1$ and $\delta d_{15} = d_{15} - d_{14}$. This normalization ensures that the result is conceptually independent of the discretization of the size range, i.e. the bin width. The simulated number density fields are averaged in time and the normalized time-averaged number density $\overline{n}_i^*$ in each bin is obtained.

Since the experimental data are not fully converged statistically, a comparison of the average total oil concentration (integrated over all bins) between experiment and simulation yielded differences of factors of 1.4 and 3.7 at downstream locations corresponding to $x = 0.76$ m and $x = 1.3$ m respectively, in this case. Therefore, here we focus the comparison between experiment and simulation on the shape of the resulting size distribution rather than the total concentration. In particular, we normalize the size distribution for both the experiment and the simulation by the total volume concentration ($\overline{n}_i^* \times V_i$) summed over the entire size range, where V_i is the volume of a droplet of size

d_i, as defined earlier. We define the relative size distribution, N_i^* according to

$$N_i^* = \frac{\overline{n}_i^*}{\sum_j (\overline{n}_j^* V_j)\delta d_j}. \tag{4.4}$$

Figure 4.6 depicts the log of the total volume-averaged concentration of oil, $\log_{10}(\sum_i \widetilde{n}_i V_i)$. The black squares show the locations of the measurement volumes used to obtain the size distributions. We compare the relative size and volume distributions obtained from the simulations with the experimental data in Figures 4.7 , 4.8 and 4.9. The left panel depicts the relative size distribution and the right panel shows the relative volume defined by $N^* V_i$, where V_i is the volume of a particular bin. The data reported in the experiment represents an average over three realizations recorded during 1 s. In the simulation, the nozzle is fixed, and so the measurement at $t = 3.4$ s for the experiment translates to a window between $x = 0.76$–0.91 m. We chose a region from $y_1 = 0.37$ m to $y_2 = 0.4$ m and $z_1 = 0.56$ m to $z_2 = 0.59$ m for our measurement volume. We can see that the simulation captures the overall relative size volume distribution at this location, although the experimental data have large scatter. The number density for the smallest droplet sizes are higher in the simulation than in the experiment, and we do not observe the dip seen in the experimental data. The higher number density for the smaller sizes seen in the LES results may be due to the fact that the breakup probability density function favors the

formation of small droplets according to the model equation used for $P(d_i, d_j)$. The reported data is not statistically converged and the experiment can only measure droplets with diameter larger than about 20 μm.

In order to explore the sensitivity of the results to the assumed initial size distribution at the injection point, we perform a second simulation in which instead of placing the entire volume injection rate into a single bin at 1 mm, it is distributed equally among the two largest bins. As shown in Figure 4.7 (circles with dot dashed line), the results for droplets smaller than 400 μm are the same and are quite robust to details of the injection distribution at the large droplets.

Figure 4.8 shows the normalized size distribution at $t = 6.9$ s for the experiment corresponding to a window of $x = 1.285$–1.435 m for the simulation. We see that the relative size and volume distribution is well matched for this later time, now also including the smaller droplets. Finally, Figure 4.9 shows the total normalized size distributions for the experiment. The total size distribution was measured in the experiment using data from 5 time instances corresponding to a spatial window $x = 0.76$–1.66 m in the simulation. We see that the model captures the relative size and volume distributions well.

We can track the plume paths of the different droplet sizes by calculating the centroid of the plume in the axial direction for each droplet size as a function of cross-stream distance. We can see from the left panel of Figure 4.10 that

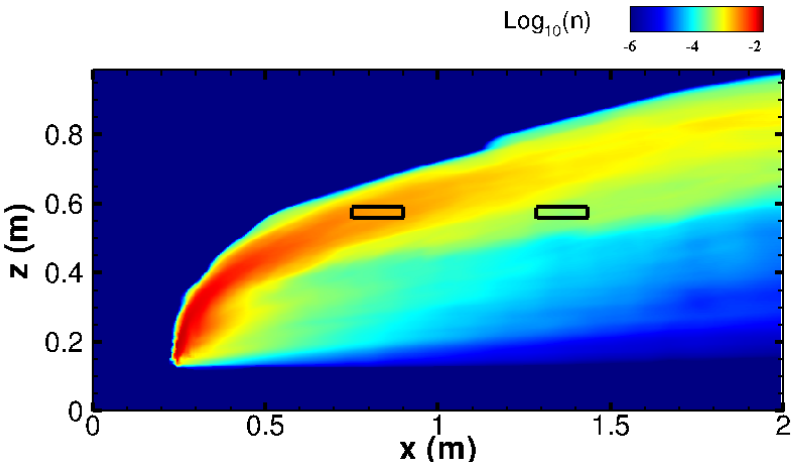

Figure 4.6: Contour plot of the logarithm of the averaged total volume concentration of oil showing the measurement location at $x = 0.76$ m and $x = 1.3$ m.

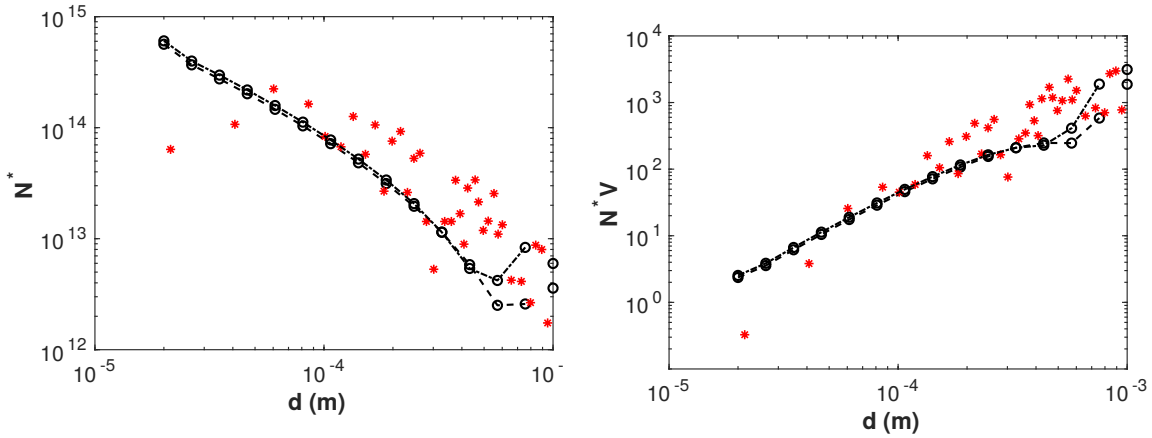

Figure 4.7: Comparison of LES model at $x = 0.76$ m for mono-dispersed injection (-o-) and bi-dispersed injection (-o··), and experimental data from[72] measured at the corresponding time (∗). Left panel: Relative size distribution from LES, Right panel: Relative volume distribution.

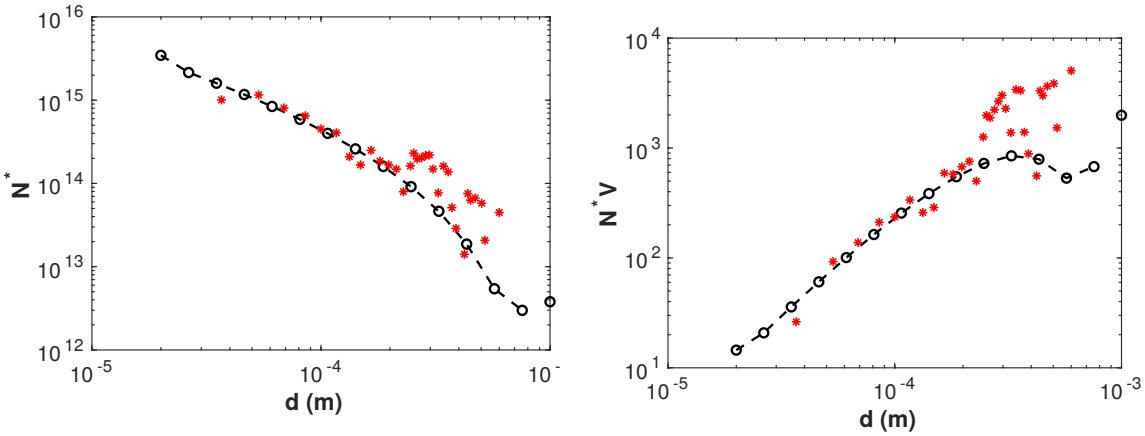

Figure 4.8: Comparison of LES model at $x = 1.3$ m (-⊖-) , and experimental data from[72] measured at the corresponding time ($*$). Left panel: Relative size distribution from LES, Right panel: Relative volume distribution.

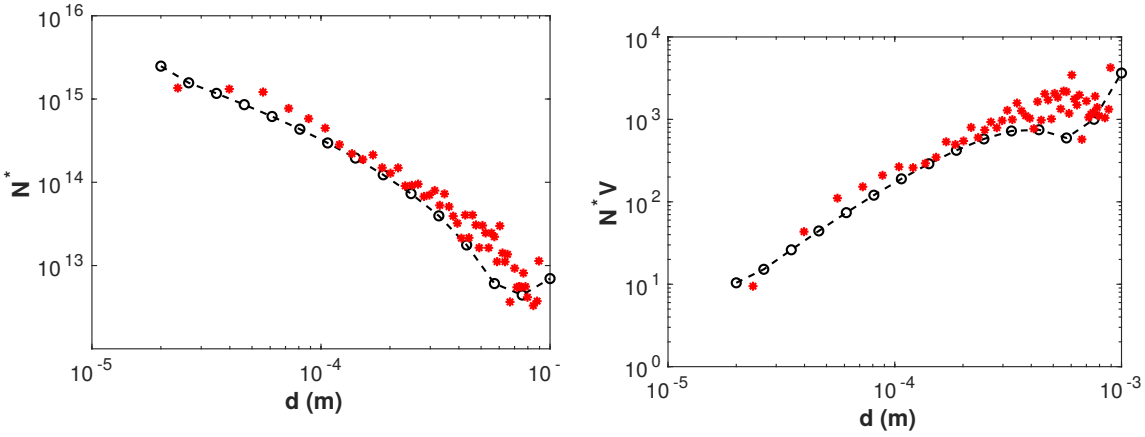

Figure 4.9: Comparison of LES model averaged over a spatial window of $x = 0.76$–1.66 m (-⊖-) , and total averaged experimental data from[72] ($*$). Left panel: Relative size distribution from LES, Right panel: Relative volume distribution.

as the jet moves farther downstream, the centroid for the larger droplets moves above the smaller ones, with the difference in height being related to the difference in rise velocities as noted already. The centroid evolution for the smallest droplets shown (20 and 107 μm) are indistinguishable. The rise velocities for these droplet sizes are very small (3×10^{-5} and 9×10^{-4} m/s, respectively) and their trajectories and plume centroids are thus dominated (equally for both droplet sizes) by mean flow and turbulence, but not appreciably by buoyancy.

We can also examine the concentration distribution of the different sizes along the axial direction at different cross-stream locations. In the right panel of Figure 4.10 we plot the concentration distribution at $x = 1$ m. We can see that the concentration is peaked more towards the top end of the plume. This trend can be attributed to the counter-rotating vortex pair generated due to the jet in crossflow[22]. This results in droplets being moved from the bottom of the plume towards the top, leading to a higher concentration at the top end. We can also confirm that the plume of smaller droplets is wider than that of larger droplets, showing that the smaller droplets are more dispersed by the turbulence.

The simulation showcases the importance of including the viscous range of scales in the formulation of the breakup frequency. The Kolmogorov scale in the near nozzle region, close to the injection location ($x = 0.125$ m and $z = 0.14$ m) where $\langle\epsilon\rangle = 30$ m^{2}s^{-3} can be calculated as $\eta = (\nu^3/\langle\epsilon\rangle)^{1/4} \approx 13$ μm.

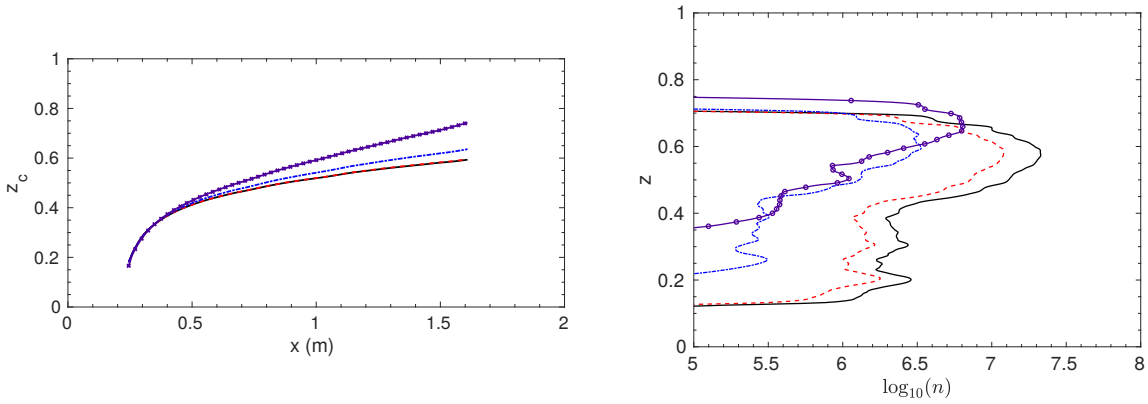

Figure 4.10: Left panel: evolution of centroid of various droplet plumes. Right panel: logarithm of the concentration profile as function of height at a downstream distance, $x = 1$ m and transverse position $y = 0.385$ m. The lines are $d = 1000$ μm(—o—), $d = 432$ μm(- · -), $d = 107$ μm(- - -) and $d = 20$ μm(——).

Droplets smaller than $\approx 10\eta = 130$ μm would lie in the viscous range. Further downstream at the y-mid-plane, where the average dissipation has decayed to $\langle\epsilon\rangle \approx 0.1$ m^{2}s^{-3}, $\eta \approx 60$ μm. Thus most of the droplet size range is in the viscous range. Earlier models that assumed that all the sizes were in the inertial range would predict incorrect breakup frequencies for these droplets as it would overestimate the eddy fluctuation velocity at the scale of the droplet. This highlights the importance of having a framework that can smoothly transition between droplets in the inertial and viscous range.

In order to characterize the 'typical size' of droplets, one may evaluate the widely used Sauter mean diameter, denoted as d_{32}, that expresses the mean diameter of the polydisperse oil by taking into account the volume to surface area ratio of the distribution. It is calculated directly from the distribution

using the formula,

$$d_{32} = \frac{\sum_i \tilde{n}_i d_i^3}{\sum_i \tilde{n}_i d_i^2}. \tag{4.5}$$

Using the mean concentrations from the LES, the d_{32} value can be computed at various locations of the flow. Figure 4.11 shows the downstream evolution of d_{32} as a function of the downstream distance x at three heights. Clearly the mean droplet size decreases as the jet flow evolves along the downstream direction of the crossflow due to droplet breakup, though the rate of change diminishes and appears to reach a stationary scale of about $d_{32} \approx 300$ μm at large distances away from the nozzle.

Another scale often used is the Hinze (maximum) diameter, $d_{max} \sim \langle\epsilon\rangle^{-2/5}(\sigma/\rho_c)^{3/5}$, by assuming that droplet coalescence does not occur[49,38] and using Kolmogorov scaling. Since here the dissipation rate varies greatly from one location to the next, it requires us to first compute the average dissipation. It is computed as the time average of ϵ according to equation (3.12) from the LES. Typical values are $\langle\epsilon\rangle \approx 0.6$ m^2/s^3 at $x = 0.3$ m and $z = 0.29$ m near the nozzle, and $\langle\epsilon\rangle \approx 0.001$ m^2/s^3 at $x = 0.75$ m and $z = 0.56$ m further downstream. Accordingly, using $\rho_c = 1018.3$ kg/m^3 and $\sigma = 1.9 \times 10^{-2}$ N/m (see table 1), we obtain $d_{max} = 1$ mm near the nozzle while $d_{max} = 18$mm far from the nozzle. The latter value is consistent with the fact that far from the nozzle breakup becomes far less frequent and the distribution has acquired an equilibrium value. The results show that the Hinze scale at a particular location in which the flow has

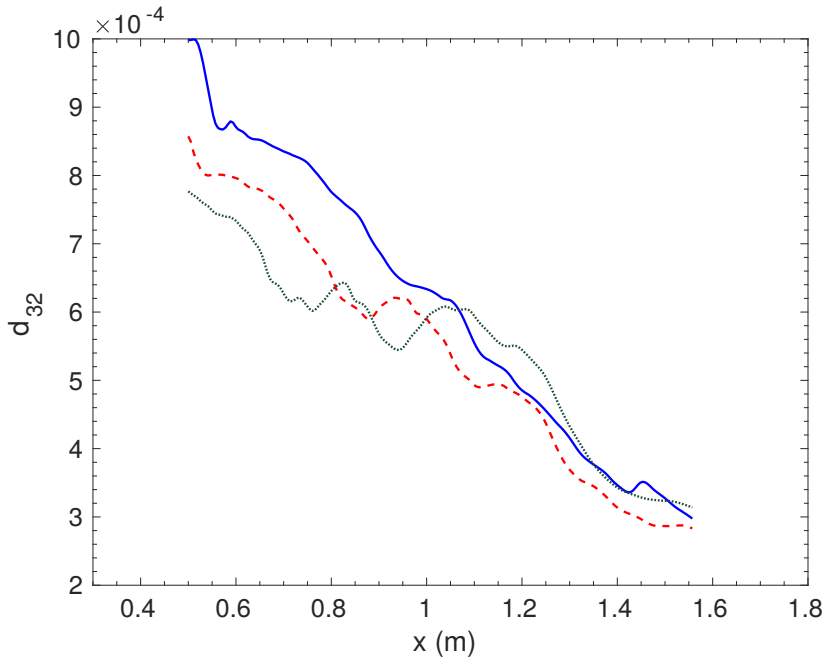

Figure 4.11: Average d_{32} diameter as function of downstream distance x at various plume heights. The lines correspond to $z = 0.55$ m (—), $z = 0.50$ m(- - -) and $z = 0.45$ m(· · ·)

large differences in dissipation rates from one location to another (as is usually the case in turbulent shear flows) cannot be used to determine the typical local droplet scale that is, instead, influenced mostly by upstream events. Note that at a few grid points from the nozzle exit, where the dissipation $\langle\epsilon\rangle \approx 30$ m^2/s^3 the Hinze diameter, $d_{max} = 300$ μm. The dissipation in a turbulent flow is highly intermittent, a property that is captured in the current study and is discussed further subsequently. Hence, we prefer to continue the discussion of the median diameter d_{32} and its variability in the next section.

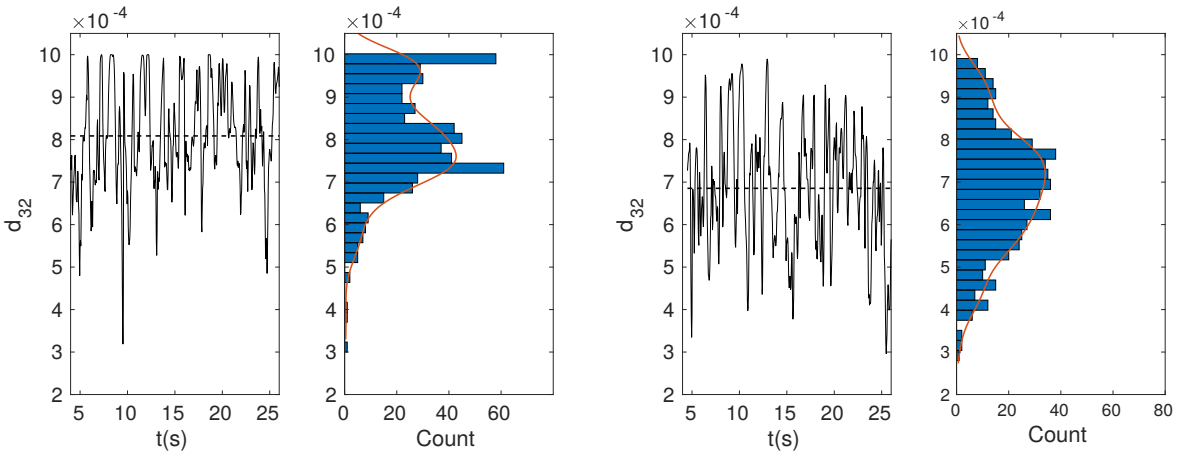

(a) $x = 0.75$ m, $z = 0.56$ m. **(b)** $x = 0.9$ m, $z = 0.56$ m.

Figure 4.12: Representative time signals (left panels) and histograms (right panels) for the Sauter mean diameter, d_{32} at two downstream locations on the centerline. Dotted lines denote mean values.

4.4 Variability of Droplet Size Distribution

As mentioned earlier, LES enables us to diagnose variability of the droplet size distributions and number density transport that RANS cannot obtain, since the latter only predicts time or ensemble average values. In order to illustrate this capability of LES, we now ask what is the inherent variability of typical droplet sizes as well as that of other practically relevant quantities.

We plot a time signal and histograms of the d_{32} diameters at different plume locations in Figure 4.12. We can see that there is a high variability of the diameter about the time averaged mean value. This variability can be observed in LES since we are solving for 3D time-dependent number density fields for

each bin and so d_{32} can be evaluated at any grid point at any timestep. At $x = 0.75$ m, where the averaged d_{32} diameter is about 800 μm, we see a variability from 300 μm to 1000 μm. The PDF also shows non-Gaussianity, with two peaks, clearly showing that the average values of d_{32} do not provide a complete description. The peak near 900 μm is affected by the discrete bins. This scale corresponds to the first bin considered in the summation corresponding to $d = 1$ mm.

Recall that in LES the breakup time scale depends upon the local value of dissipation, which is also known to be highly intermittent in turbulent flows. In order to illustrate the (grid-scale averaged) dissipation intermittency, in Figure 4.13 we show time signals of the logarithm of dissipation as well as histograms. The histogram of the logarithm of dissipation is reminiscent of Gaussian (log-normality) but with a non-Gaussian highly asymmetric tail and some outliers at very low dissipation, corresponding possibly to laminar regions outside the plume. This highly variable quantity then determines the local time scale of droplet breakup in the LES model.

Next, we consider a property that is crucial in determining reaction rates for processes that occur on the droplet surface such as bio-degradation. The total rate of bio-degradation will depend on the total surface area of the oil available for microorganisms to act upon. Given the instantaneous concentration of droplets in each bin, the instantaneous total surface area available for

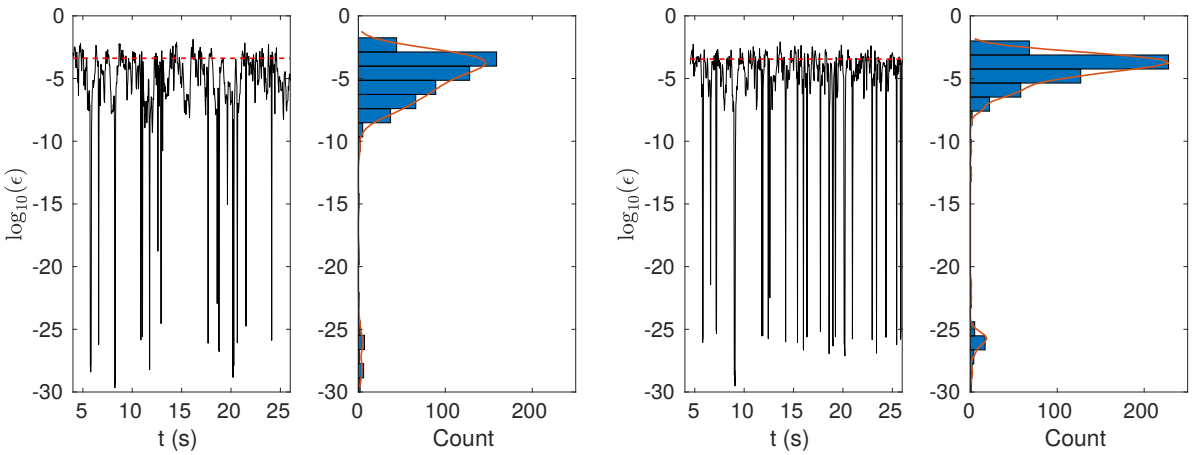

(a) $x = 0.75$ m, $z = 0.56$ m. **(b)** $x = 0.9$ m, $z = 0.56$ m.

Figure 4.13: Representative time signals (left panels) and histograms (right panels) of $\log_{10}(\epsilon)$ at two downstream locations on the centerline. ϵ is in m^2/s^3. Dotted lines denote mean value.

surface reactions can be evaluated according to

$$A_{tot}(\mathbf{x}, t) = \sum_{i=1}^{N_d} \tilde{n}_i(\mathbf{x}, t)\,(\pi d_i^2). \tag{4.6}$$

Representative signals and histograms of $A_{tot}(\mathbf{x}, t)$ are shown in Figure 4.14, again at the two locations $x = 0.75$ m and $x = 0.9$ m at $z = 0.56$ m and the plume center in the transverse direction.

We can see from the panels in Figure 4.14 that there is a high variability of the total area about the mean of about 30 m^2 per cubic meter of water at $x = 0.75$ m and about 16 m^2 per cubic meter of water at $x = 0.9$ m (even though one may expect smaller droplet sizes to be associated with an increase in total surface area, further downstream the total oil concentration has also

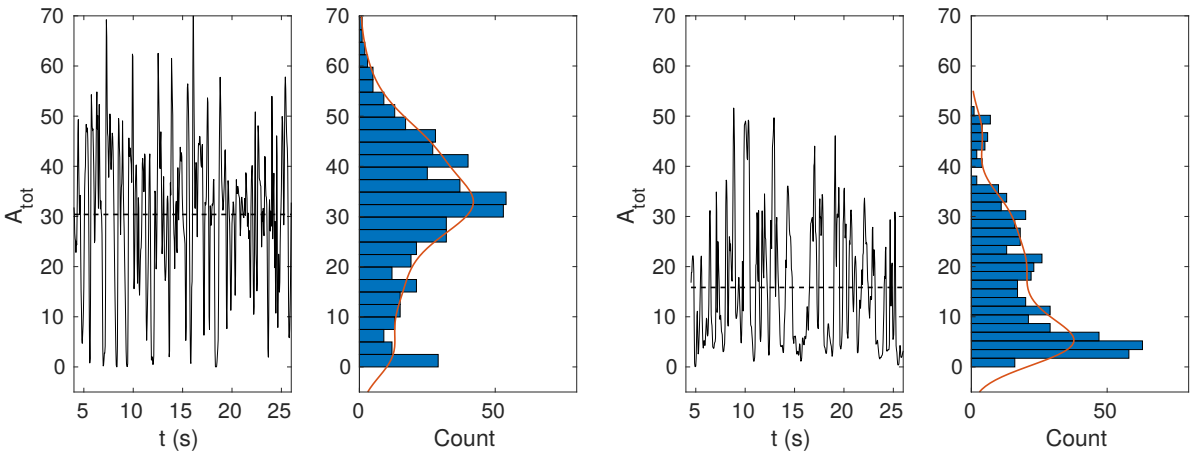

(a) $x = 0.75$ m, $z = 0.56$ m. **(b)** $x = 0.9$ m, $z = 0.56$ m

Figure 4.14: Representative time signals (left panels) and histograms (right panels) of total surface area of the oil per cubic meter of fluid at two downstream locations on the centerline. A_{tot} is in m^2/m^3. Dotted lines denote mean values.

decreased due to turbulent transport thus leading to the smaller area there). The root mean square of the surface area distribution is quite significant, of similar order of magnitude to the mean area.

It is also instructive to examine time signals and statistics of the breakup source term for each droplet size, $\tilde{S}_{b,i}$, normalized by the concentration. This normalization can be interpreted as an inverse time scale for the droplet breakup, i.e. it tells us the inverse of the time taken for the number of droplets in any given bin to change appreciably over its existing value, at any given scale. In Figure 4.15 we show representative signals of $\tilde{S}_{b,i}(\mathbf{x}, t)/\tilde{n}_i(\mathbf{x}, t)$ in logarithmic scale, as well as its histograms at two locations. As can be seen from the right panel of Figure 4.15*a*, the average values are around 0.5 s^{-1}, with very large variability about this value. It means that it takes about 2 seconds for the local

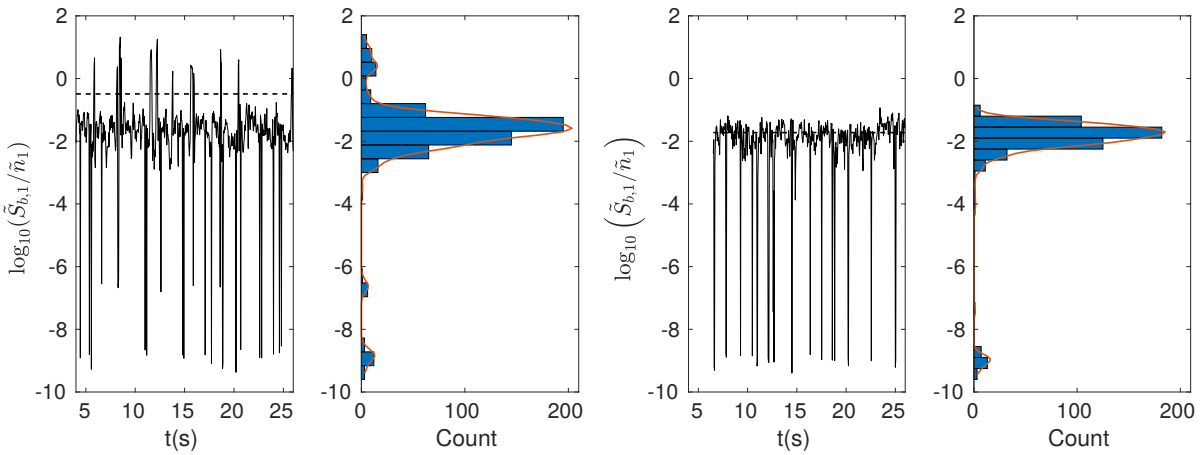

(a) $x = 0.75$ m, $z = 0.56$ m. **(b)** $x = 1.21$ m, $z = 0.56$ m.

Figure 4.15: Representative time signals (left panels) and histograms (right panels) of $\log_{10}(\tilde{S}_{b,i}/\tilde{n}_i)$ for $d = 20$ μm plotted at two downstream locations of the plume at a fixed height. The values of $\tilde{S}_{b,i}/\tilde{n}_i$ are given in $1/s$. Dotted lines denote mean values.

breakup rate to appreciably change the local concentration of droplets of size 20 μm but occasionally the breakup can be far more rapid.

Finally, we document the breakup source term by plotting it in linear units for different droplet sizes, at two different locations as shown in Figure 4.16. We can see that the time signals for the source term are highly intermittent, with the largest size (i.e. 15th bin) acting as a source for the smaller ones (negative source term in its transport equation). Further downstream at $x = 1.56$ m, Figure 4.16*b* shows much smaller frequencies indicating a decreased breakup of the largest droplets. Some of the intermediate bins display both positive and negative values, as some intermediate droplet sizes act as both sources and sinks at different locations along the plume (for example see panel for $S_{b,7}/n_7$ in Figure 4.16*c*).

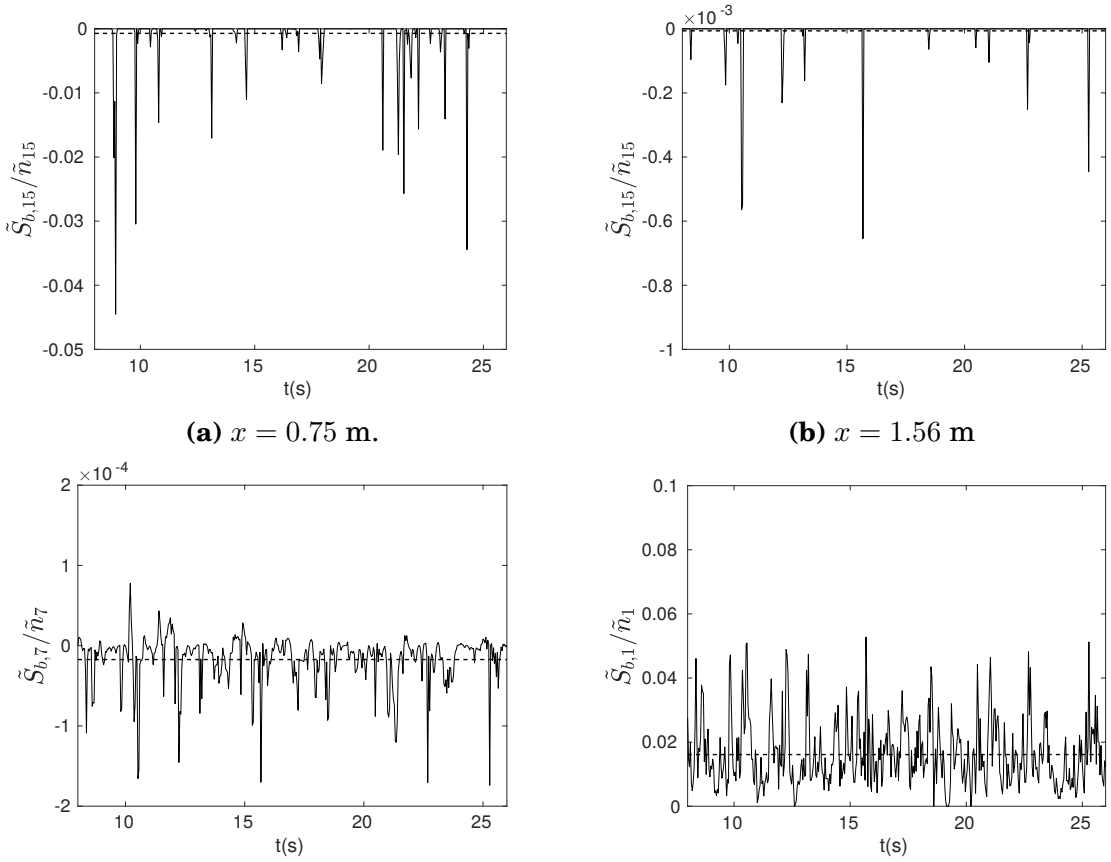

(a) $x = 0.75$ m. **(b)** $x = 1.56$ m

(c) $x = 1.56$ m **(d)** $x = 1.56$ m

Figure 4.16: Time history of $\tilde{S}_{b,i}$ normalized by concentration for different droplet sizes at $z = 0.56$ m on the centerline. (a) and (b) represent the droplet of size 1000 μm at two different x locations, (c) is the time history for $d = 432$ μm and (d) is for $d = 20$ μm. Dotted lines denote mean values.

We still see a significant variance in the volume median diameter (d_{32}) at this location despite the magnitude of the normalized source terms for the larger droplets being small. Clearly, the turbulent nature of the flow prevents us from solely relying on the averaged quantities to provide us with a complete view of the droplet size distribution in this flow, while LES contains significant amount of new information regarding the fluctuations, at least down to the grid scale.

4.5 Conclusions

We have proposed a method to couple LES with a population balance equation to study the evolution of polydisperse oil droplets in turbulence. We use the method of classes to discretize the droplet size range into contiguous subclasses and consider the case of spherical droplets at relatively low volume fraction for which coalescence can be neglected. Using a jet in crossflow as a flow application inspired by previous studies on deep-water oil spills, the model can be used to predict the turbulent transport of droplets of various sizes while accounting for breakup due to the turbulent flow field. The formulation was tested by comparing the size distributions of oil droplets obtained at different locations along the plume with the experimental data of Murphy et al.[72]. We find that the relative droplet size distribution from the simulation showed good

agreement with the experimental data.

Finally, we used the LES results to quantify various new properties of the distribution as it refers to the inherent variability of turbulence. We show how the LES provides information on the variability of the median diameter, the total area available for surface reactions and illustrate the highly non-Gaussian properties of the source (reaction) terms in the transport equations for each bin of droplet concentration fields.

Chapter 5

Hybrid ODE-LES Approach : Model Development

5.1 Introduction

Brandvik et al.[11] performed a series of oil jet experiments in a large cylindrical tank with a diameter of 3 m and a height of 6 m filled with $40\ m^3$ of water . Crude oil was injected from a nozzle in the form of a submerged turbulent jet into the system at a controlled temperature at various flow rates. The nozzle diameter size ranged from $D_J = 0.5\ mm$ to $D_J = 3\ mm$ with injection flow rates varying from $Q = 0.5\ L/min$ to $Q = 5\ L/min$. The steady state droplet size distribution was measured using an in situ laser diffractometer. The apparatus had a maximum detection size of $460\ \mu$m which could be insufficient for some

of the cases simulated. In all these experiments the droplet size distribution in the near nozzle region is difficult to characterize due to the high turbulence intensity and opacity and measurements were taken $2\ m$ downstream of the injection location. Simulating smaller nozzle diameters is challenging as the near nozzle region requires high resolution to capture deforming interfaces. Coarse simulations, focusing on the secondary breakup use a mono-disperse inlet droplet size distribution, however this is not sufficiently general.

We develop a hybrid modeling approach that allows us to specify more realistic inlet size distributions for use in a coarse LES of a turbulent jet. As shown schematically in Figure 5.1 the LES starts some distance downstream of the experimental nozzle, where the initial jet has spread sufficiently so that it can be resolved by the coarse LES mesh. In this Chapter we discuss a method to determine the inlet size distribution for coarse LES using a one-dimensional version of the population dynamics approach (denoted as 1D ODE model) as a reduced order parcel model for the breakup processes. The model assumes droplet breakup due to turbulence at smaller scales than what we can resolve initially in our simulation. We use simplified (eddy-viscosity based) theory of turbulent jet evolution to account for the radial turbulent transport of centerline concentrations. This approach predicts the actual rather than the relative concentration distribution at the centerline. The 1D ODE population dynamics model is validated with experimental data available downstream[11], and is

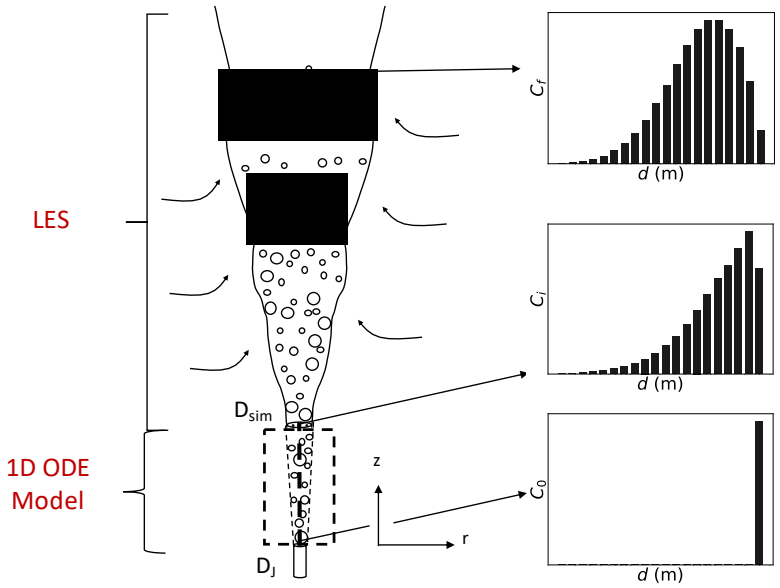

Figure 5.1: Schematic diagram of the hybrid ODE-LES modeling approach: Between the nozzle and the end of the 1D ODE model region, the size distribution is obtained by integrating a 1D ordinary differential equation for the centerline concentrations. The results are used as inflow concentrations for the Eulerian-Eulerian LES further downstream.

then used to provide the inflow size distribution (inlet condition) for the coarse large-eddy simulations.

5.2 One-Dimensional ODE Model

Following the approach of Chapter 2, the size distribution of drops is assumed to be governed by a population dynamics equation including the effects of advection, radial diffusion and droplet breakup due to turbulence. In general, one can include other source terms for coalescence, evaporation or aggregation into the framework but here we focus on dilute turbulent jets and limit

the discussion to droplet breakup.

5.2.1 Model Development

We begin using a 2D polar co-ordinate system to develop the model with z as the axial and r the radial coordinate. The origin is at $z = 0$ corresponding to the nozzle exit shown in Figure 5.1. We use a Reynolds-averaged Navier-Stokes (RANS) formulation (unlike the eddy-resolving LES case treated in Chapter 4) coupled with a simple eddy-viscosity approach. The 2D approach is then cast as a 1D problem by only considering the centerline evolution ($r = 0$). The total concentration field of oil droplets is discretized into a finite number of bins based on the droplet diameter. The total concentration is related to the concentration in each bin through the equation

$$\overline{c}(z,r) = \sum_{i=1}^{N} V_i \overline{n}_i(z,r), \tag{5.1}$$

where, N is the total number of bins used to discretize the droplet size range, n_i is the number of droplets of size d_i per m^3 of fluid and $V_i = (\pi/6)\, d_i^3$ is the volume of a droplet of diameter d_i. The overbar denotes RANS averaging. The steady-state population dynamics equation for the droplet concentration including the effects of advection, radial diffusion and droplet breakup can be written for

each droplet size as,

$$\overline{w}\frac{\partial \overline{n_i}V_i}{\partial z} + \bar{v}_r\frac{\partial \overline{n_i}V_i}{\partial r} = S_{b,i}\,V_i + \frac{D_T}{r}\frac{\partial}{\partial r}\left(r\frac{\partial}{\partial r}\overline{n_i}V_i\right), \tag{5.2}$$

where $\bar{v}_r, \overline{w}$ are the mean radial and axial velocities, respectively, and $S_{b,i}\,V_i$ is the droplet breakup source term to model the change of the concentration due to droplet breakup, to be described later. The eddy diffusivity D_T is assumed to be independent of radial position and only depend on z. The rise velocity of the individual droplets has been neglected as it would be small compared to the jet centerline velocity in the near nozzle region. The molecular diffusivity is also neglected since typically $D << D_T$.

The mean velocity is modeled following the classic eddy viscosity approach. The conservation of mass and momentum in a round turbulent jet, expressed in polar co-ordinates using the boundary-layer approximation, read:

$$\frac{\partial \overline{w}}{\partial z} + \frac{1}{r}\frac{\partial (r\bar{v}_r)}{\partial r} = 0, \tag{5.3}$$

$$\overline{w}\frac{\partial \overline{w}}{\partial z} + \bar{v}_r\frac{\partial \overline{w}}{\partial r} = \nu_T\frac{1}{r}\frac{\partial}{\partial r}\left(r\frac{\partial \overline{w}}{\partial r}\right) \tag{5.4}$$

Above, ν_T is the z-dependent eddy viscosity. Again, the molecular viscous diffusion term is neglected in the high Reynolds number cases considered. The

mean velocity profile using the assumption of a similarity variable can be written as[80],

$$\overline{w}(z,r) = \overline{w}_0(z) f(\eta), \tag{5.5}$$

where $\eta = r/(z - z_0)$ is the similarity variable. For the case of $r-$independent eddy viscosity, the resulting self-similar velocity profile $f(\eta)$ reads[80,56],

$$f(\eta) = \frac{1}{(1 + \alpha^2 \eta^2)^2}, \tag{5.6}$$

where the coefficient α is related to the spreading rate S of the jet, $\alpha^2 = (\sqrt{2} - 1)/S^2$. The downstream centerline velocity, jet width, and dissipation can thus be deduced :

$$\frac{\overline{w}_0}{\overline{w}(z)} = \frac{1}{C_u}\left(\frac{z}{D_J} - \frac{z_0}{D_J}\right), \qquad r_{1/2} = S(z - z_0), \qquad \frac{\epsilon D_J}{\overline{w}_0^3} = C\left(\frac{z}{D_J} - \frac{z_0}{D_J}\right)^{-4}, \tag{5.7}$$

where $C_u = 6$, $S = 0.1$ and $C = 65$[67,101,40] are empirically determined constants, z_0 is the virtual origin of the jet, and D_J is the nozzle diameter. Next, we consider the droplet concentration equation (5.2). Similar to equation (5.7), we aim for a formulation that describes the centerline concentration evolution as function of z only, and must therefore replace the radial derivatives term with a suitable approximation. To this end we assume that the relative radial dependence of the solution is unaffected by the source term. Setting $S_{b,i} = 0$ in

equation (5.2), the concentration in each bin obeys the same evolution equation of the total mean concentration, $\bar{c}$, given by:

$$\overline{w}\frac{\partial \overline{c}}{\partial z} + \bar{v}_r\frac{\partial \overline{c}}{\partial r} = \frac{D_T}{r}\frac{\partial}{\partial r}\left(r\frac{\partial}{\partial r}\overline{c}\right) \tag{5.8}$$

that is amenable to solution using a similarity variable. To complete the similarity solution, one must express it in terms of the total scalar flux injected at the source, Q_0, defined as

$$Q_0 = 2\pi\int_0^\infty \overline{w}(z,r)\,\overline{c}(z,r)\,r\,dr, \tag{5.9}$$

which remains constant independent of z.

We can introduce a non dimensional scalar profile similar to equation (5.5) for equation (5.8) according to:

$$\frac{\overline{c_i}(z,r)}{\overline{c}_{0,i}(z)} \;=\; \phi(\eta) \;=\; \frac{\overline{c}(z,r)}{\overline{c}_0(z)}. \tag{5.10}$$

In order to find $\phi(\eta)$ we can substitute equation (5.10) into equation (5.8). Using the expressions for the self similar velocity profile and the evolution of the mean centerline velocity field described in equations (5.6) and (5.7), we obtain

an ordinary differential equation for $\phi(\eta)$,

$$D_T^{-1}\eta\left(1+\alpha^2\eta^2\right)^2\phi^{''}+\left(D_T^{-1}\left(1+\alpha^2\eta^2\right)^2+\frac{C_u w_0 D_J \eta^2}{2}\left(1+\alpha^2\eta^2\right)\right)\phi^{'}+C_u w_0 D_J \eta\phi=0. \tag{5.11}$$

In order to write equation (5.11) in terms of α and the turbulent Schmidt number, $Sc_T = \nu_T/D_T$, we note that for the constant eddy-viscosity solution, $C_u D_J w_0 = 8\alpha^2\nu_T$[80]. Equation (5.11) can then be re-written as,

$$Sc_T^{-1}\eta\left(1+\alpha^2\eta^2\right)^2\phi^{''}+\left[Sc_T^{-1}\left(1+\alpha^2\eta^2\right)^2+4\alpha^2\eta^2\left(1+\alpha^2\eta^2\right)\right]\phi^{'}+8\alpha^2\eta\phi=0. \tag{5.12}$$

The solution to the above equation that monotonically decreases away from the centerline is given by[56],

$$\phi(\eta)=\frac{1}{\left(1+\alpha^2\eta^2\right)^{2Sc_T}}. \tag{5.13}$$

Equation (5.13) is an exact solution to 5.8 but only approximately valid for the individual bin concentration fields as we had neglected the breakup source term in its derivation (for which no similarity solution exists in general). Note however that we only make this approximation in evaluating the radial derivative term, and then set $\eta = 0$. Substituting equations (5.6) and (5.10) into

equation (5.2) we obtain,

$$\overline{w}_0(z)f(\eta)\frac{\partial}{\partial z}[n_{0,i}(z)\phi(\eta)] = S_{b,i} + \frac{1}{r}\frac{\partial}{\partial r}\left(rD_T\frac{\partial}{\partial r}[n_{0,i}(z)\phi(\eta)]\right). \tag{5.14}$$

Substituting the similarity solution given by equation (5.13), evaluating the derivatives with respect to r and setting $r = \eta = 0$ we obtain the centerline evolution of each bin's number concentration,

$$\frac{d}{dz}n_{0,i}(z) = S_{b,i}(z,0)\,\frac{z}{w_0 C_u D_J} - \frac{n_{0,i}(z)}{z}, \quad i = 1,2,3..N. \tag{5.15}$$

Equation (5.15) describes a system of ODEs that needs to be solved numerically to obtain the evolution of the individual droplet concentrations, accounting for droplet breakup and turbulent transport at the centerline. Note that the breakup source term $S_{b,i}$, does not alter the decay rate of the overall concentration, $\overline{c}(z)$ defined through equation (5.9). This can be verified by multiplying equation (5.15) by the corresponding droplet volume V_i and summing over all droplet sizes and noting that $\sum_i S_{b,i}V_i = 0$.

The breakup source term is modeled based on Chapter 2. The source term can be written as :

$$S_{b,i}(z,0) = \sum_{j>i}^{N} P(d_i,d_j)g(z,0,d_j)\overline{n}_j(z,0,d_j) - g(z,0,d_i)\overline{n}_i(z,0,d_i). \tag{5.16}$$

The first term on the right-hand side of equation (5.16) represents the birth of droplets of size d_i due to the total contribution from breakup events of larger droplets of diameter d_j. The second term accounts for death of droplets of size d_i due to breakup. $P(d_i, d_j)$ is the probability of formation of a droplet of size d_i due to the breakup of a parent droplet of size d_j. The breakup is considered to be binary, and $P(d_i, d_j)$ is formulated based on the formation energy required to form the daughter droplets of size d_i and a complementary droplet to ensure volume conservation[104,1] (see Chapter 2 for additional details).

5.2.2 Model Validation

We validate the 1D ODE model in equation (5.15) with data from turbulent oil jet experiments[11]. The experimental setup consists of a cylindrical tank with a diameter of 3 m and a height of 6 m with crude oil being injected at a controlled temperature at various flow rates. The details of the cases used in this work are provided in table 5.1. The droplet size distribution for each case was measured 2 m above the nozzle exit using a LIST-100X laser diffractometer. For each experiment oil volume fractions (i.e oil concentration of a particular bin, normalized by the total concentration of all bins) were provided for 29 logarithmically spaced droplet size classes ranging from 4.5 μm to 460 μm. Droplets larger than 460 μm could not be recorded by the instrument. The experimental data is reported as a relative volume fraction of oil for each size at

the measurement location. In order to make comparisons with the 1D ODE model, we first need to determine the total oil concentration of the reported distribution.

The overall centerline concentration can be determined as a function of downstream distance, Schmidt number, Sc_T and the inflow rate Q_0 using equation (5.9). Substituting the similarity profiles for $w(z,r)$ and $\phi(z,r)$ into the equation we obtain

$$Q_0 = 2\pi z^2 \int_0^\infty \frac{w_0(z)}{\left(1+\alpha^2\eta^2\right)^2} \frac{c_0(z)}{\left(1+\alpha^2\eta^2\right)^{2Sc_T}} \eta \, d\eta. \tag{5.17}$$

The integral in equation (5.17) can be evaluated analytically and yields :

$$I = c_0(z) w_0(z) (2\alpha^2)(2\mathrm{Sc}_T + 1)^{-1} \tag{5.18}$$

We can therefore evaluate the centerline concentration as a function of downstream distance z and the centerline mean velocity $w_0(z)$ as:

$$c_0(z) = \frac{Q_0 \alpha^2 (2\mathrm{Sc}_T + 1)}{\pi w_0(z)\, z^2}. \tag{5.19}$$

Given the known total oil injection rate Q_0 in the experiments, the total (all sizes) centerline oil concentration as a function of downstream distance, $c_0(z)$, can be obtained using equation (5.19). This result would be expected to include

both the concentration measured by the instrument and the unmeasured concentration of larger drops. The limitation on the maximum measurable drop size is expected to lead to an underestimation of the total oil volume at the measurement location, since we expect at least some of the drops to be larger than $460\ \mu m$. An extrapolation approach will be used to augment the measurement data.

We define the number density, as the number concentration $\overline{n}_i$ normalized by the bin width, as the width of the bins used in the experiments is not necessarily the same as that used in the model, i.e

$$n_i^* = \frac{\overline{n_i}}{\delta d_i}, \tag{5.20}$$

where $\overline{n}_i$ is the number of droplets per m^3 fluid in bin i with a bin width $\delta d_i = (d_{i+1} - d_{i-1})/2$ for $i = 2$ to $N-1$, $\delta d_1 = d_2 - d_1$ and $\delta d_N = d_N - d_{N-1}$. The normalization ensures that the result is independent of the discretization of the size range (bin width). The symbols in Figure 5.2a show the experimentally measured relative number density n_{rel}^* as a function of drop diameter at the measurement location $z = 2\ m$, for both Expt. 1 and Expt. 2. The units for the relative number density are number of droplets per m^3 of fluid per bin width μm^{-1} normalized by the total oil concentration of the measured distribution. We can see that the scaling of the relative size distribution follows two distinct

power law regimes for the small and large droplets. In order to quantify the unmeasured concentration, we smoothly extend the tail of the distribution to the nozzle diameter D_J using a fitting function $F(d)$. This step will account for the contribution of droplets of size $d > d_{max}$ to the total concentration. The unmeasured volume fraction can then be calculated by integrating the fitted particle size distribution $F(d)$ from $d_{max} = 460$ μm to the largest possible droplet size, here assumed to be the nozzle diameter D_J,

$$\phi_{un} = \int_{d_{max}}^{D_j} v(d)\, F(d)\, \mathrm{d}d, \tag{5.21}$$

where $v(d) = \pi/6\ d^3$ is the volume of the particle with diameter d (internal coordinate for the size range discretization). The concentration in the experimental distribution can be calculated as,

$$c_{dist} = \frac{c_0(z = 2m)}{1 + \phi_{un}}. \tag{5.22}$$

Using equations (5.19), (5.21) and (5.22) we can determine the fraction of the concentration measured by limiting the maximum diameter to $d_{max} = 460$ μm. For the case with $d = 1.5$ mm and $Q = 1.5$ L/min we find that the measured concentration accounts for 92.86% of the total, whereas for $d = 3$ mm and $Q = 5$ L/min the measured concentration describes only 44% of the total concentration. Thus for the case with the larger nozzle diameter, restricting

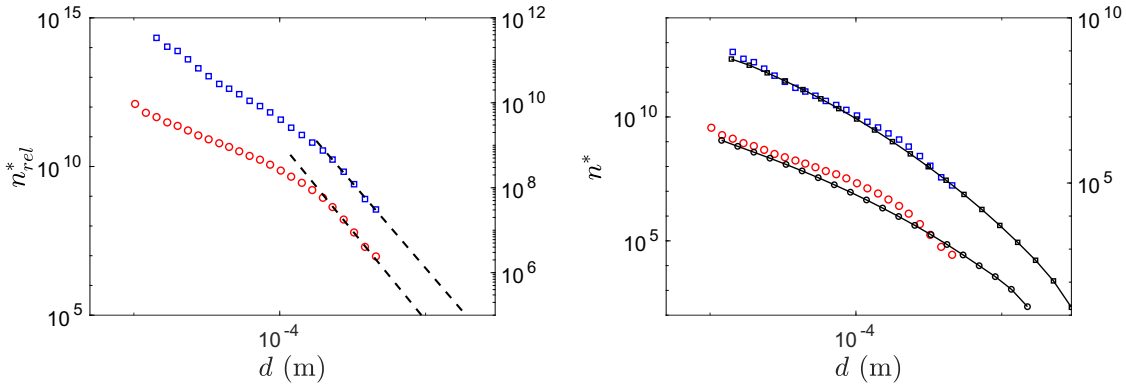

Figure 5.2: (a) Relative number density distribution of Expt. 1 (□) and Expt. 2 (○) at $z = 2m$. The y-axis is scaled differently for visualization purposes. The right axis depicts the size distribution from Expt. 1 while the left axis depicts the size distribution from Expt. 2. The dashed line (- - -) denotes the fit of the tail of the distribution with $F_1(d) = A_2 d^{-4}$ and $F_2(d) = A_1 d^{-6}$. The fitted constants are $A_1 = 1.28 \times 10^{-6}$ and $A_2 = 6.76 \times 10^{-14}$, (b) Comparison of number density distribution from the 1D ODE model for Expt 1. (–□–) and Expt. 2 (–●–) and corresponding experimental data (□, ○) at measurement location.

the maximum droplet size to 460 μm would underestimate the total volume of oil measured. Therefore, for our validations and subsequent simulations, we choose the maximum droplet size to be equal to that of the nozzle.

For the purpose of validation, we discretize the droplet size range into $N = 20$ bins, with the maximum diameter, $d_{20} = D_J$. We have tested the sensitivity of the results to the number of bins used to discretize the droplet size range and find that 20 bins is sufficient to accurately capture the size distribution. The initial droplet concentration is determined by equation (5.19) at a distance of $z = 2\ D_J$ from the nozzle and a potential core region is assumed between $2 - 6\ D_J$ after which the velocity and dissipation decay according to equation

(5.7). The entire inflow number concentration was placed into the largest bin, d_{20}, i.e. assuming that the injection begins at the nozzle with drops of diameter equal to the jet diameter. The number concentration was obtained by dividing the concentration in a bin by the volume of a single drop with diameter equal to that corresponding to the bin size. The concentration for all other bins were initially set to zero. The physical properties of the oil and inflow conditions of the experiments are summarized in Table 5.1. The Schmidt number is set to $Sc_T = 0.7$ which is in the range of commonly used values in literature for passive scalars in turbulent jets[21,64]. We then numerically solve the set of ODE's Eq. (5.15) for the number concentration (number of droplets per m^3 of fluid) of each droplet size, from $z = 2\ D_J\ z = 2\ m$, also using equations (5.7),(5.19), and (5.16).

The total experimental distribution for each case was calculated by multiplying the relative size distribution by the total concentration obtained from equation (5.22). This renormalization ensures that the total oil flux at the measurement location in the experiment is equal to the source flux Q_0. The number density from the model is compared to the experimental results at $z = 2$ m for Expt. 1 and Expt. 2 in Figure 5.2b. We see that the model not only predicts the size distribution in the experimental size range, but also smoothly extends the distribution for larger sizes. The total concentration distribution can then be reconstructed using equation (5.10).

Table 5.1: Summary of Experimental conditions for the different cases.

$No.$	D_J (mm)	Q (L/min)	U_J (m/s)	$\sigma(N\ m^{-1})$	$\mu_d(Pa\ s)$
Expt. 1	3	5	11.8	15.5×10^{-3}	5×10^{-3}
Expt. 2	1.5	1.5	14.1	15.5×10^{-3}	5×10^{-3}

5.2.3 Inlet Condition for Large Eddy Simulations

In the previous section, it was shown that the 1D ODE model can predict the average size distribution of oil droplets at the centerline, showing good agreement with experimental datasets. This model can be considered as sufficient if the only aim is to predict the time-averaged size distribution. If one also wishes to predict the variability of the size distribution and radial concentration fluctuations in each size bin, taking into account the effect of the underlying turbulence, the use of LES is required.

In this section we describe using the 1D ODE model to generate an inlet condition for LES bridging the near nozzle region to further downstream, where LES begins to resolve the flow. We explain the approach for the case with $D_J = 3\ mm$ and $Q = 5\ L/min$ and assume that the LES grid is coarse such that only at $z > 10D_J$ can it begin to represent the eddying motions inherent in the turbulent jet.

The 1D ODE model requires as input the centerline velocity and dissipation, for which we utilize Eq. (5.7). These inputs are plotted in Figure 5.3a, where we plot the evolution of the centerline velocity and dissipation as a func-

tion of downstream distance. The 1D ODE model (Eq. (5.15)) is then integrated numerically and the results, i.e. the normalized centerline concentration evolution of the different droplets sizes, are shown in Figure 5.3b. As can be seen, in the first part the breakup process dominates the evolution (concentration of the smaller drop sizes increases downstream), while downstream (after around $z/D_J \sim 30$), all concentrations decrease monotonically, where fluid transport (axial advection and radial turbulent transport) dominates the evolution of concentrations. In order include some of the droplet breakup process in the LES domain, we chose $z = 10\ D_J$ downstream of the nozzle exit as the location where the size distribution from the 1D ODE model is used as inlet condition for the LES. This location is depicted by the dashed line in Figure 5.3b. The jet width at this location can be calculated using equation (5.7) to be $r_{1/2} = 0.1z = D_J$ (this width also sets the diameter of an equivalent "coarse jet for the LES" as $D_{sim} \approx 2D_J$, see discussion in Chapter 4) . The corresponding centerline velocity shown in Figure 5.3a at $z = 10\ D_J$ is used as the jet injection velocity. It is important to note that there is no special significance of choosing $z = 10\ D_J$. If a different location, for example, for $z = 13\ D_J$, we would use the corresponding size distribution from Figure 5.3b and injection velocity from Figure 5.3a.

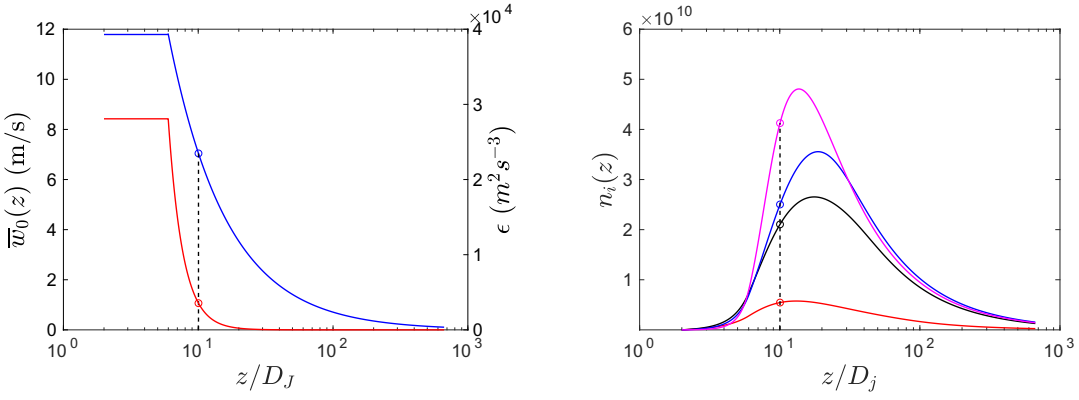

Figure 5.3: a Parameterized jet centerline velocity (- · -) and dissipation (—), used as an input to the 1D ODE model. b Scaled centerline number concentration, n_2 ; $d = 18.5$ μm (—), $5 \times n_7$; $d = 76$ μm (- · -), $10 \times n_9$; $d = 134$ μm(—) and $10 \times n_{12}$; $d = 313$ μm(- - -) as a function of downstream distance. The initial conditions for LES are determined by the concentration values at $z = 10D_J$ depicted by the dashed line (- - -).

5.3 Conclusions

Accurate prediction of the droplet size distribution in a turbulent flow is paramount in understanding the dynamics of numerous multiphase processes. We have applied a population balance model to study the evolution of oil droplets at the centerline of an axisymmetric turbulent jet. A key unknown in simulating secondary breakup in turbulent multiphase jets is the inflow size distribution generated within the primary breakup zone near the nozzle exit. A mono-disperse injection inflow condition is commonly used for simplicity, but this choice is often unrealistic. In order to provide more realistic injection conditions for coarse-grid LES, we develop a 1D ODE model that predicts the evolution of the dispersed phase at the centerline turbulent jet by incorporat-

ing effects of droplet breakup and turbulent transport. The model is based on classical turbulent jet theory and is validated with experiments of Brandvik et al.[11], obtaining good agreement. The 1D ODE model is then used to provide an injection condition for a coarse grid LES of a turbulent jet described in Chapter 6.

Chapter 6

Hybrid ODE-LES Approach Applied to a Turbulent Round Jet

6.1 Introduction

We follow the approach used in Chapter 4 that couples population dynamics equations with Eulerian LES for both the continuous and dispersed phases (population densities of droplets of various sizes). Using the hybrid approach developed in Chapter 5 we specify a realistic inlet size distribution for droplets injected at the centerline of a coarse LES. As shown schematically in Figure 5.1 (in Chapter 5) the LES starts some distance downstream of the experimental nozzle, where the initial jet has spread sufficiently so that it can be resolved by the coarse LES mesh. We present simulations for two droplet Weber num-

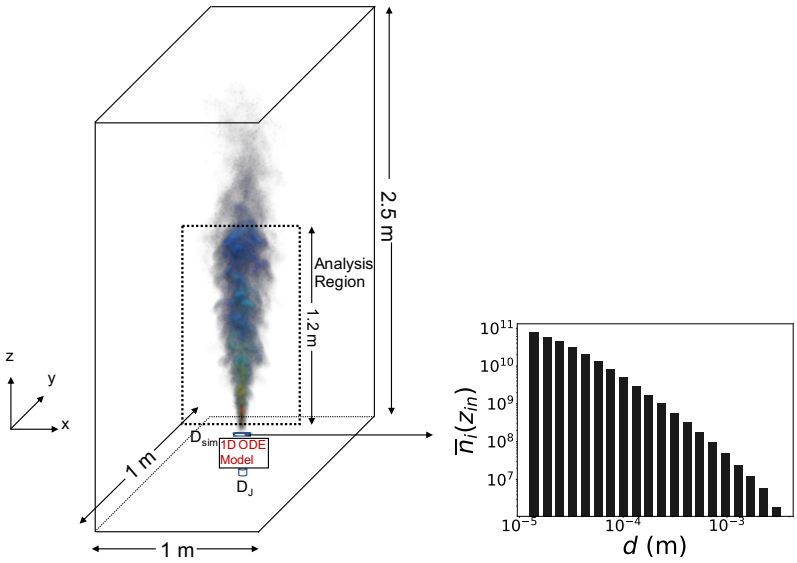

Figure 6.1: (a) Sketch of the simulation setup. Volume rendering of the instantaneous 14 μm diameter droplet concentration with the 1000 μm droplets visualized as dots placed randomly with density proportional to its concentration field. (b) Inlet distribution, n_i (number of droplets per m^3 of fluid) for LES determined by the one-dimensional model,

bers and examine the role of changing Weber number on the evolution of the droplet size distribution. In the following sections, we first describe the simulation setup in section 6.2 and then present results, including comparisons with experimental data in section 6.3. Conclusions are presented in section 6.4. The content in this chapter can be found in in Aiyer and Meneveau[2].

6.2 Simulation Setup

A sketch of the simulation domain is shown in Figure 6.1. We simulate a turbulent jet aiming to reproduce the experiments of Brandvik et al.[11], specif-

No.	$We = \frac{2\rho_c \langle\epsilon\rangle^{2/3} d_{20}^{5/3}}{\sigma}$	$\sigma(mN\ m^{-1})$	$\overline{w}_{in}$ (m/s)	D_{sim} (mm)	D_J (mm)
SIM 1	410	15.5	7	6	3
SIM 2	820	7.75	7	6	3

Table 6.1: Simulation parameters.

ically the case with nozzle diameter $D_J = 3\ mm$ and flow rate $Q_0 = 5\ L/min$. This particular case, due to the larger nozzle diameter, allows us to use a relatively coarse mesh for the LES, while at the same time resolving a significant portion of the breakup. For instance, the case with $D_J = 1.5\ mm$ discussed in Chapter 5 would require us to have double the resolution in the horizontal directions in order to simulate the breakup dominated zone in LES. The experimental setup and measurement techniques have been described in Chapter 5. We use a hybrid approach where a population balance model is used to provide the drop concentration injection rates at each size (q_i) as inlet condition (Figure 6.1b), and the subsequent secondary breakup and evolution of the oil droplets is simulated using LES. As shown in Figure 6.1, the simulations are carried in a rectangular box of size $(L_x, L_y, L_z) = (1, 1, 2.5)$ m. The experimental nozzle exit is chosen as the origin in the vertical direction. The simulated jet starts at a distance of $z = 10\ D_J$ from the origin. The simulations use a grid with $N_x \times N_y \times N_z = 288 \times 288 \times 384$ points for spatial discretization, and a timestep $\Delta t = 6 \times 10^{-5}$ s for time integration. The resolution in the horizontal directions, $\Delta x = \Delta y = 3.47$ mm is set to ensure that at the location where the LES begins

to resolve the jet (the 'simulated inlet', see below), we have at least 3 points across the jet. In the vertical direction we use a grid spacing of $\Delta z = 6.5$ mm enabling us to capture a domain height 2.5 times the horizontal domain size.

The injected jet is modelled in the LES using a locally applied vertically upward pointing body force following the procedure outlined in Chapter 3, since at the LES resolution used in the simulation it is not possible to resolve the small-scale features of the injection nozzle. The resulting injection velocity is controlled by the strength of the imposed body force $\widetilde{F}$ applied such that the resulting centerline velocity in the LES matches the mean centerline velocity expected for the experiment at a distance $z = 10\ D_J$ from the experimental nozzle as shown in Figure 5.3a.

The droplet number density fields are initialized to zero everywhere. In order to avoid additional transient effects, the concentration equations are solved only after a time at which the jet in the velocity field has reached near the top boundary to allow the flow to be established. Based on the inlet distribution calculated in Chapter 5 oil droplets are injected as follows: The number density transport contains a source term, $\widetilde{q_i}$ on the RHS of equation (3.6) that represents injection of droplets of a particular size. The source term is calculated based on equation (5.17) for each bin size as:

$$\widetilde{q_i} = \frac{\gamma_z \gamma_{xy}}{\Delta x \Delta y \Delta z} \frac{4\pi\alpha^2 z_{in}^2 \overline{w}_0(z_{in}) \overline{n_i}(z_{in})(2\alpha^2)}{(2\mathrm{Sc}_T + 1)}, \tag{6.1}$$

where $\overline{w}_0(z_{in})$, $\overline{n_i}(z_{in})$ are the inlet velocity and concentration determined in §5.2.3 at $z_{in} = 10\ D_J$. This ensures that the total injected concentration flux at the inlet $\sum_i \widetilde{q}_i V_i$ is equal to the source flux, $Q_0 = 5\ L/\text{min}$ from Brandvik et al.[11]. The source is centered at (x_c, y_c, z_c) = (0.5 m, 0.5 m, 10 D_J) and distributed over two grid points in the z direction with weights $\gamma_z = 0.7$ and $\gamma_z = 0.3$ at z_c and $z_c + \Delta z$ respectively and over three grid points in the horizontal directions with weights $\gamma_{xy} = 0.292$ at (x_c, y_c) and $\gamma_{xy} = 0.177$ at $(x_c \pm \Delta x, y_c \pm \Delta y)$. In order to study the effects of changing Weber number on the concentration distribution, we perform a second simulation halving the surface tension of the oil, and thus doubling the Weber number. The physical properties of the oil and the simulation parameters are given in Tables 5.1 and 6.1.

6.3 Results

6.3.1 Jet Velocity and Total Concentration Field

Statistics of the velocity and concentration fields are shown using a cylindrical coordinate system with z being the axial coordinate, and supplement the time averaging with additional averaging over the angular θ direction. The LES averaged quantities will be denoted by angluar brackets while the aver-

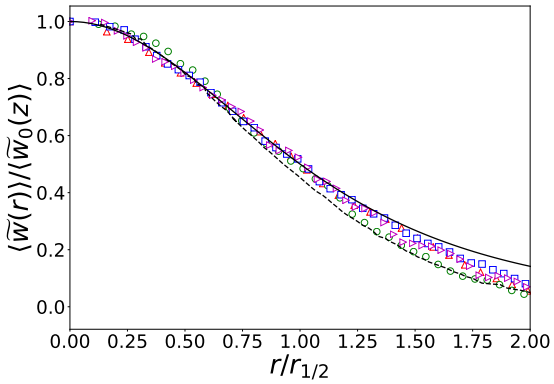

(a) Velocity

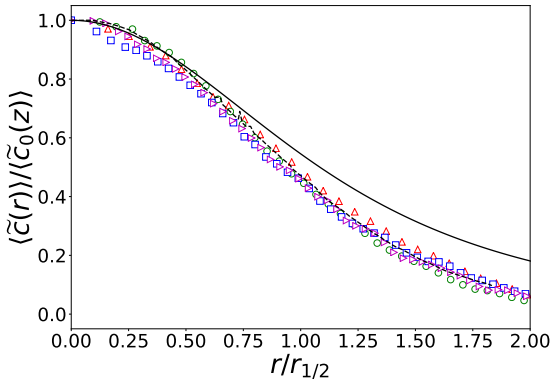

(b) Concentration

Figure 6.2: a Averaged axial velocity profiles as function of normalized radial distance, b Averaged concentration profiles at $z/D_J = 135$ (△), $z/D_J = 168$ (○), $z/D_J = 211$ (□) and $z/D_J = 243$ (▷) as a function of self similarity variable $r/r_{1/2}$. The dashed line (- -) denotes the DNS data[64] and the solid line (——) represents the analytical constant eddy-viscosity solution.

aged quantities from the 1D ODE model will be denoted by an overbar.

We document the radial distribution of velocity and concentration at different downstream locations, in Figure 6.2. The velocity profiles shown in Figure 6.2a show approximate collapse on self similar behavior when normalized by the centerline value and plotted as a function of $r/r_{1/2}$, the radial coordinate scaled by the jet half-width. Additionally it shows good agreement with the

constant eddy-viscosity similarity solution defined in equation (5.6) in the central part of the jet, whereas it falls below the constant eddy viscosity solution at larger r values, a behavior typically ascribed to the decreasing eddy viscosity in the outer parts of the jet[80]. The DNS result from Lubbers et al.[64], shown as the black dashed lines, agrees well with LES data also in the outer portions of the jet. The radial profiles of the total oil concentration normalized by the centerline value at various downstream locations is shown in 6.2b. Similar to the velocity profiles, the total concentration appears to be self similar when plotted as a function of $r/r_{1/2}$. Additionally, we plot the concentration profile derived from the constant eddy-diffusivity hypothesis, defined in equation (5.10) with a Schmidt number, $Sc_T = 0.7$ as the solid black line. We see that the analytic solution shows agreement with the simulation results near the centerline of the jet, with discrepancies at $r/r_{1/2} > 0.5$. Conversely, the data is in excellent agreement with the DNS data[64] across the jet width.

The radial distribution of the concentration fluctuations root-mean-square (r.m.s.) normalized by the mean centerline concentration is shown in Figure 6.3. As observed in prior simulations[64], the concentration fluctuation r.m.s. shows an off-axis peak and in general shows good agreement with the DNS results of Lubbers et al.[64].

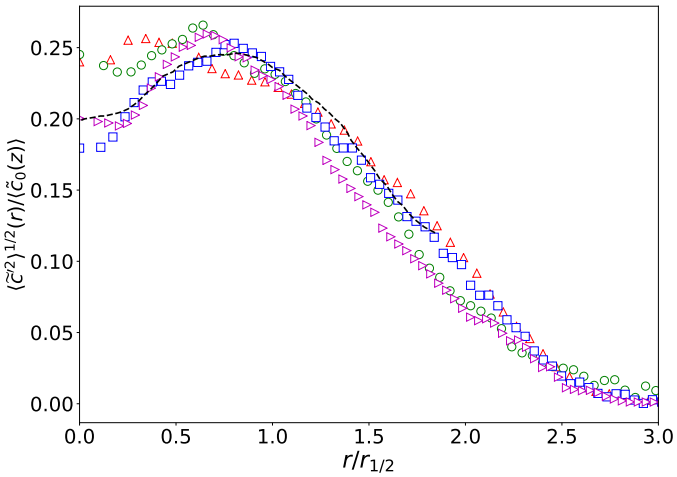

Figure 6.3: Radial distributions of concentration fluctuation root-mean-square at $z/D_J = 135$ (△), $z/D_J = 168$ (○), $z/D_J = 211$ (□) and $z/D_J = 243$ (▷)), normalized by centerline mean concentration, as a function of $r/r_{1/2}$.

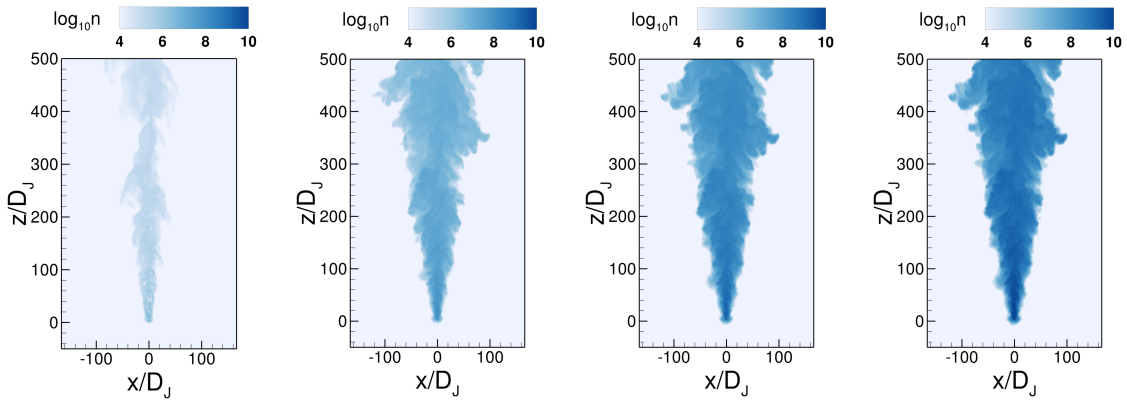

(a) $d = 3000$ μm **(b)** $d = 730$ μm **(c)** $d = 134$ μm **(d)** $d = 18$ μm

Figure 6.4: Instantaneous snapshots of concentration fields at the midplane of the jet plotted in logarithmic scale for different droplet sizes. The domain has been cropped at $z/D_J = 500$ for visualization purposes.

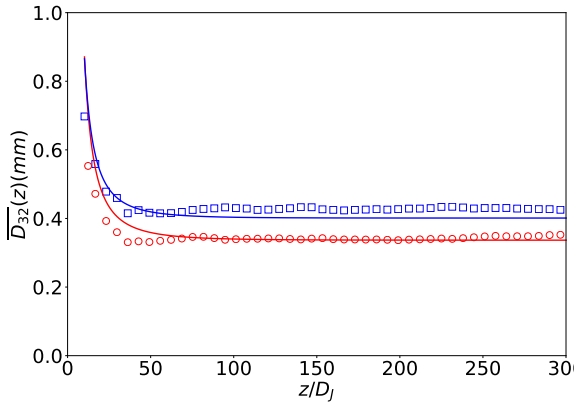

Figure 6.5: Evolution of Sauter mean diameter, D_{32} as a function of downstream distance from the nozzle for SIM 1 (□) and SIM 2 (○). The D_{32} curves from the ODE model for both cases are depicted by a solid line.

6.3.2 Droplet Size Distribution

Figure 6.4 shows contour plots of instantaneous number density in logarithmic scale ($log_{10}(\tilde{n}_i)$) for four representative droplet sizes on the mid y-plane as a function of x and z. The concentration of the largest droplet size is in Figure 6.4a and the smallest in Figure 6.4d. We can see that far away from the nozzle the concentration of the largest size has decreased significantly due to breakup into the smaller droplet sizes. High concentrations for the smaller sizes can be seen to occur already in the near nozzle region due to the high dissipation rate that causes rapid droplet breakup there.

The Sauter mean diameter, (D_{32}) is often used to quantify the size distribution by defining a characteristic diameter for a polydisperse distribution. It is defined as the volume to surface area ratio of the distribution and is calculated

from LES results using

$$\overline{D}_{32} = \left\langle \frac{\sum_i \tilde{n}_i d_i^3}{\sum_i \tilde{n}_i d_i^2} \right\rangle . \tag{6.2}$$

The Sauter mean diameter is calculated locally and at every time step using the instantaneous LES concentration and then averaged in time and polar direction θ. We plot the average $\overline{D}_{32}$ for the two simulations as a function of downstream distance in Figure 6.5. The solid lines depict the results from the 1D ODE model. We see good agreement between the mean diameter calculated by the model and LES. Increasing Weber number reduces the overall mean diameter due to increased breakup frequency of the larger droplets in the near nozzle region. This reduction in mean diameter is reproduced to similar degrees in the LES results and the 1D ODE model. We can see from 6.5 that there is no significant change in the centerline mean diameter beyond $z = 100\ D_J$. This suggests that beyond this downstream position, no significant droplet breakup occurs. It is therefore sufficient to compare the results from the LES with that of the ODE model at $z/D_J = 333$ corresponding to a distance of $z = 1\ m$ from the experimental nozzle. This allows us to save computational cost in the LES by limiting the analysis region only up to $z/D_J = 333$. We recall that the 1D ODE model has been validated with the experimental data at $z/D_J = 666$ ($z = 2\ m$) in Figure 5.2b and showed very good agreement.

The LES number concentration fields are averaged in time and the droplet size distribution $\langle n^* \rangle$, is calculated using equation (5.20) by normalizing the

number concentration by the bin width. Figure 6.6 compares the size distribution at the centerline at $z/D_J = 333$ to the size distribution obtained from the 1D ODE model at the same location. We can see that the LES and the 1D ODE model provide very consistent predictions of the size distribution at the centerline. The error bars provide additional information regarding the turbulent fluctuations of $\langle n^* \rangle$: they are calculated using the root-mean-square (r.m.s) of the concentration for each droplet size at the centerline. Beyond $z/D_J = 333$ the evolution of each of the bins concentration is affected only by transport and not by breakup. This allows us to carry out an additional validation step by using equation (5.15) with $S_{b,i} = 0$ to calculate the thus extrapolated LES size distribution at $z/D_J = 666$. The resulting distribution from the extrapolated LES is compared with the experimental measurements in Figure 6.6 (blue squares compared to red dashed line), with excellent agreement.

The size distribution for the case with increased Weber number is shown in Figure 6.6b. We can see that due to increased breakup of the larger sized droplets, the number density of the smaller-diameter bins is larger, and the distribution has a higher slope throughout. This effect is also observed in experiments when dispersant is premixed with oil[11,120,72,60]. This shift of the concentration towards the smaller scales results in the lower Sauter mean diameter observed in Figure 6.5 for SIM 2.

LES allows us to analyze the evolution of the droplet plumes for each droplet

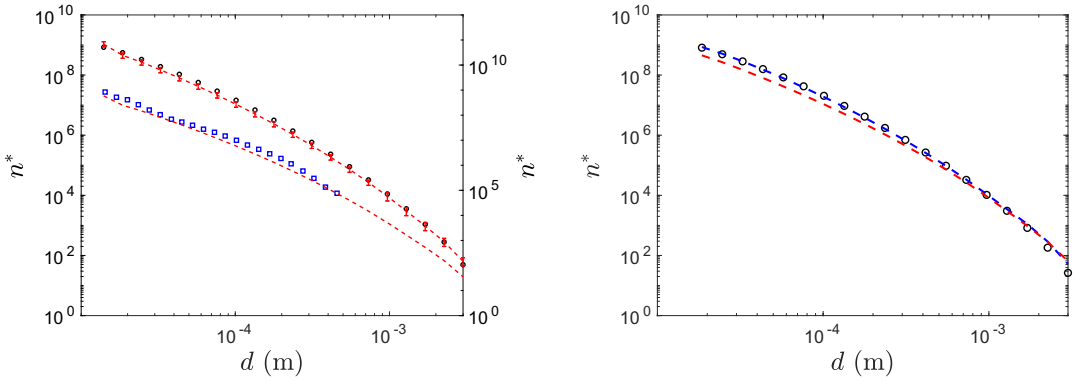

(a) SIM 1 **(b)** SIM 2

Figure 6.6: (a) Comparison of centerline droplet size distribution from experimental data (□, right axis) at $z/D_J = 666$ with extended LES results (also right axis, - - -). The latter is obtained by solving Eq. (5.15) using the LES data as inlet condition at $z/D_J = 333$ (left axis) as initial condition (these LES data at $z/D_J = 333$ are shown by the top - - -line). Error bars display the r.m.s. at $z/D_J = 333$ due to turbulence. The 1D ODE model applied between $z/D_J = 2$ to 333 is depicted by (○, left axis). (b) Comparison of droplet size distribution from SIM 2 (·····) with 1D ODE model (○) and SIM 1 size distribution (- - -) at $z/D_J = 333$.

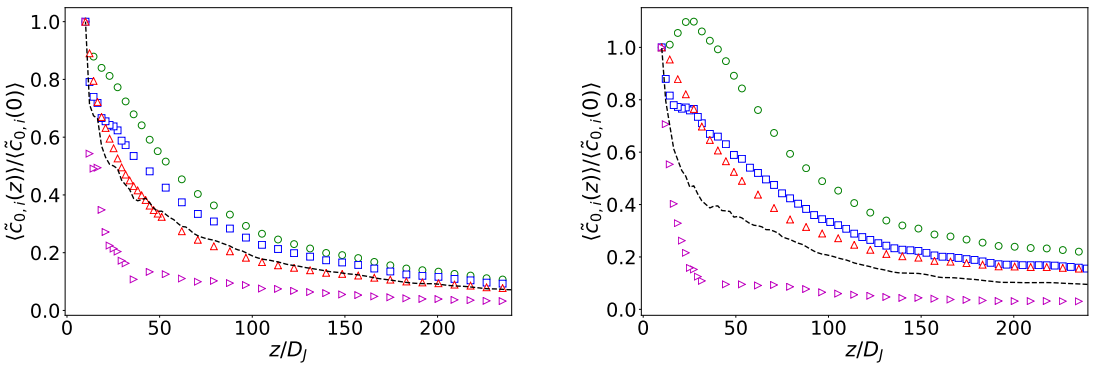

(a) SIM 1 **(b)** SIM 2

Figure 6.7: Decay of centerline concentration of different droplet sizes as a function of downstream distance from the nozzle. The symbols represent the LES evolution and the corresponding color coded dashed lines are the results from the 1D ODE model model for (a) SIM 1 and (b) SIM 2. The symbols are $d = 14$ μm (△), $d = 100$ μm (○), $d = 550$ μm (□) and $d = 3$ mm (▷). The total concentration from SIM 1 and SIM 2 is represented by the black dashed line.

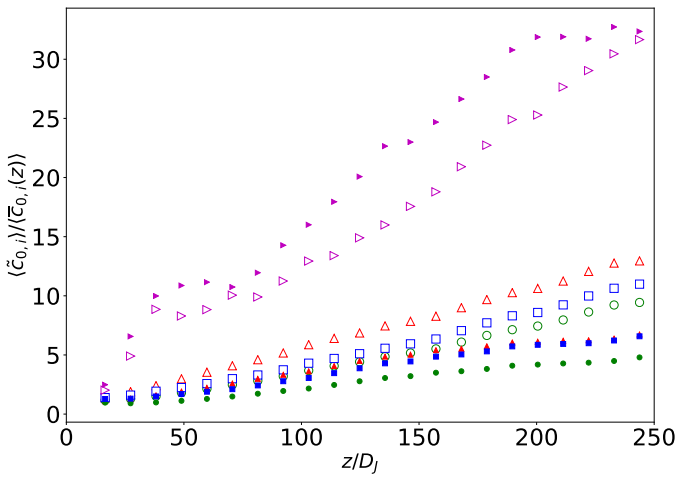

Figure 6.8: Evolution of the inverse centerline concentration for SIM 1(open symbols) and SIM 2 (closed symbols). The symbols are $d = 14$ μm (△), $d = 100$ μm (○), $d = 550$ μm (□) and $d = 3$ mm (▷).

size. The effects of breakup are clearly visible in Figure 6.7. For the largest droplet size, $d = 3$ mm we can see a rapid decay in the breakup dominated zone, approximately $z < 50\ D_J$ after which the change in concentration is primarily transport dominated. The change of initial slope and shape of the profiles among different droplet sizes is non-monotonic. The smallest droplets, of size $d = 14$ μm do not break down further and its bin acts as a sink for all the other sizes, resulting in a concentration profile that appears smoother and more monotonic than the other bins' mean concentration. The effect of increasing Weber number is to increase the rate of breakup of the larger droplets due to the reduction in surface tension, leading to the increase in concentration of the smaller droplet sizes as can be seen from Figure 6.7b. Intermediate sized droplets behave as both a source, breaking up into smaller droplets and a sink,

where larger droplets break up into the intermediate ones. This trend can be observed from the profile of the $d = 550$ μm droplet in Figure 6.7b that shows a peak near the nozzle followed by a decay of concentration. The profiles of the total concentration (summed over all bins), $\tilde{c}_0(z)$ for both the simulations are shown in Figure 6.7 as dashed lines. As expected, we confirm that the evolution of the total concentration is fairly insensitive to Weber number.

Figure 6.8 depicts the downstream evolution of the inverse of the centerline concentration for SIM 1 (open symbols) and SIM 2 (filled symbols) for different droplet sizes. The slope of the growth of the inverse concentration is size dependent, with a maximum slope for the largest droplet size, due to their rapid breakup. We can see that the change in slope for the different droplet sizes is non-monotonic, with the concentration of the $d = 550$ μm droplet decaying faster than the $d = 100$ μm droplet concentration. Increasing Weber number results in a shallower slope for the smaller sizes as can be seen from the solid symbols. Conversely for the larger sizes (primarily acting as sinks), the growth of the inverse concentration is more rapid due to the increased breakup frequency.

6.3.3 Temporal Variability of Size Distribution

As discussed earlier, LES allows us to calculate the variability of the droplet size distribution that averaged integral models or RANS cannot obtain. We

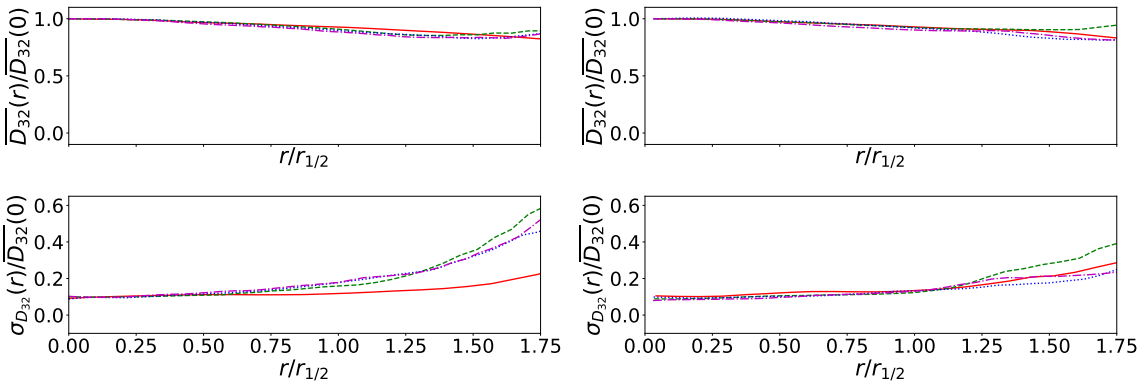

(a) SIM 1 **(b)** SIM 2

Figure 6.9: The top panel depicts the radial distribution of the averaged Sauter mean diameter, D_{32} normalized by its centerline value while the bottom panel depicts the normalized standard deviation at $z/D_J = 135$ (- - -), $z/D_J = 168m$ (- - -), $z/D_J = 211$ (····), $z/D_J = 243$ (-·-·) for (a) SIM 1 and (b) SIM 2.

proceed to quantify the radial distributions of the mean and standard deviations of practically relevant quantities such as the Sauter mean diameter, the total surface area and the inverse droplet breakup time-scale.

We begin by examining the radial distribution of the mean diameter defined in equation (6.2) normalized by its centerline value at different downstream locations in Figure 6.9. The mean diameter exhibits a weak decay with radial distance, with the centerline value decreasing by 20% at $r/r_{1/2} = 1.75$. The standard deviation of the Sauter mean diameter, normalized by the mean diameter at the centerline, is relatively low near the center (around 10%) but increases with radial distance towards the edge of the jet. We observe a maximum variability for the location farthest downstream from the nozzle. The increased variability at the edge of the jet can be attributed to the entrainment of

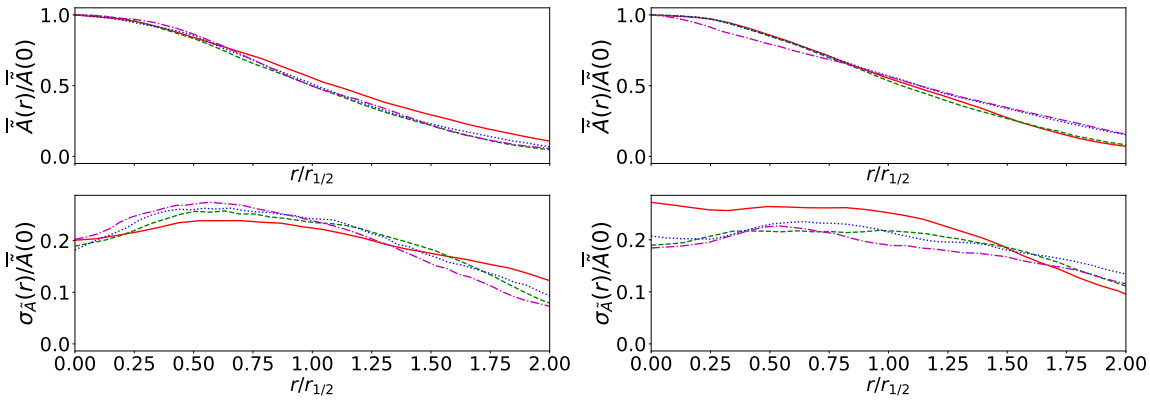

(a) SIM 1 **(b)** SIM 2

Figure 6.10: The top panel depicts the radial distribution of the averaged total surface area, $\widetilde{A}$ normalized by its centerline value while the bottom panel depicts the normalized standard deviation at $z/D_J = 135$ (——), $z/D_J = 168m$ (- - -), $z/D_J = 211$ (····), $z/D_J = 243$ (-·-·) for (a) SIM 1 and (b) SIM 2..

fluid at the edges that results in increased dilution of concentration. Increased variability in D_{32} means that the size distribution displays changes as function of time at a particular location. Increasing Weber number has minimal effect on the radial profiles of the normalized mean diameter. The variability is unchanged near the centerline of the jet but is slightly reduced towards the edge downstream of the nozzle.

Next, we examine the total surface area of the oil-water interface per unit volume of fluid, defined as:

$$\widetilde{A}(\mathbf{x}, t) = \sum_i \tilde{n}_i(\mathbf{x}, t)\, \pi d_i^2 \tag{6.3}$$

This quantity is critical in determining reaction rates for processes that occur at the surface of the droplet. The radial profiles of the total area closely follow

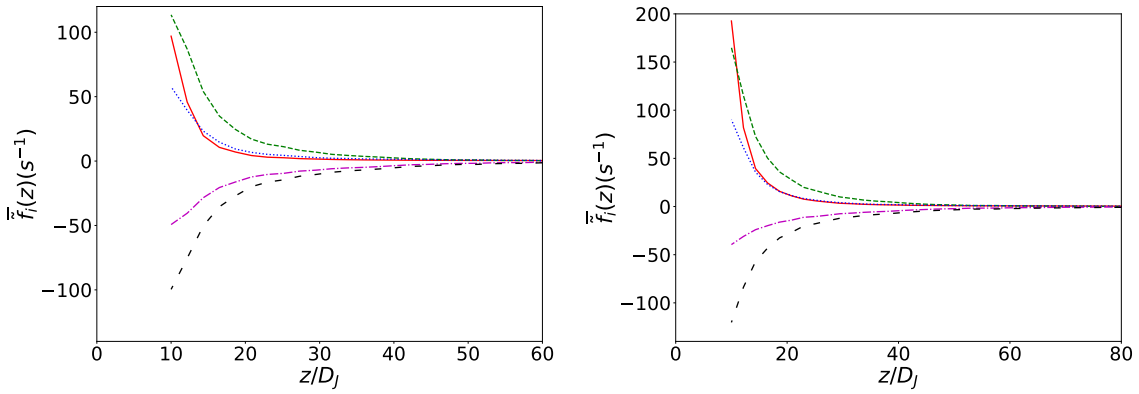

(a) SIM 1 **(b)** SIM 2

Figure 6.11: Evolution of the inverse breakup time scale with downstream distance for (a) SIM 1 and (b) SIM 2. The lines are $d = 14$ μm (——), $d = 100$ μm (- - -), $d = 550$ μm (····) and $d = 2261$ μm (-·-·) and $d = 3000$ μm (- -).

those of the mean concentration, and exhibit a reasonable collapse when plotted against the self similar co-ordinate. Interestingly, the temporal variability as quantified by means of the r.m.s. of $\widetilde{A}$ exhibits the opposite trend as compared to the Sauter mean diameter variability. There is maximum variation about the mean total area at about $r/r_{1/2} \sim 0.6$, which subsequently decays towards the edges. The shape of the profiles is similar to the concentration variance shown in Figure 6.3. We see that the normalized profiles for the mean and standard deviation are relatively unchanged with changing Weber number. Such information expands on that provided by reduced or RANS type models, that are capable of quantifying only the mean of these quantities.

The breakup source term $\widetilde{S}_{b,i}$ normalized by the droplet concentration $\tilde{n}_i$

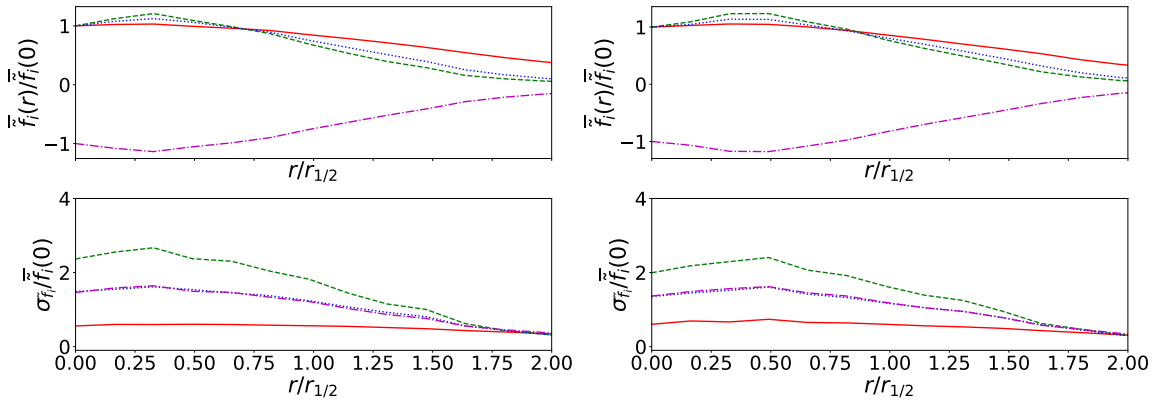

(a) SIM 1 **(b)** SIM 2

Figure 6.12: The top panel depicts the radial distribution of the averaged inverse breakup timescale, $\tilde{t}_i = \widetilde{S}_{b,i}/\tilde{n}_i$ normalized by its centerline value while the bottom panel depicts the normalized standard deviation for (a) SIM 1 and (b) SIM 2.The lines are $d = 14$ μm (——), $d = 100$ μm (- - -), $d = 550$ μm (-·-·) and $d = 3000$ μm (-·-·) at $z/D_J = 70$.

provides quantification of the inverse timescale for the breakup :

$$\tilde{f}_i = \left\langle \frac{\widetilde{S}_{b,i}}{\tilde{n}_i} \right\rangle . \tag{6.4}$$

This ratio can be interpreted as an inverse time-scale for droplet breakup to appreciably change the concentration of a particular size. Figure 6.11 depicts the near nozzle evolution of five representative droplet sizes as a function of distance from the nozzle. We can see that the values are high near the nozzle exit where the breakup is rapid. The negative sign denotes that the $d = 3$ mm and $d = 2261$ μm droplets, on average, act as sources for the smaller ones. A value of $\overline{\tilde{f}} = -60$ at the centerline means that it takes $1/60$ of a second for the local breakup to appreciably change the concentration of that droplet size. The

values of the inverse timescale are also non monotonic with respect to droplet size. For instance, the time-scale for $d = 100$ μm droplet size is more rapid than the $d = 14$ μm droplet size. We can see that the inverse time scale increases for SIM 2 indicating that at larger Weber number the concentration changes more quickly, on a shorter time-scale. The radial profiles for the mean inverse time scale and its variability at $z/D_J = 70$ are shown in Figure 6.12. From the top panel of Figure 6.12a we observe that the breakup is most rapid slightly off centre of the jet and then decays towards the edge of the jet. We can see that there is a high variability across the jet width, reflecting the underlying intermittency of the turbulent flow. Although an increase in Weber number results in a higher inverse breakup time-scale, the normalized radial profiles of the mean and variance appear relatively unchanged.

This variability analysis from LES can be used as a tool to determine inherent fluctuations due to turbulence in measured quantities characterizing the droplet size distribution. Droplet Weber number, although having a significant effect on the average distribution of various quantities, leaves the normalized radial profiles of the mean and standard deviations relatively unchanged.

6.4 Conclusions

We perform two simulations with distinct Weber numbers to study surface tension effects on the evolution of the droplet size distributions. The axial profiles of the individual droplet fields show interesting differences in the breakup dominated zone, exhibiting a size dependent decay rate. The radial profiles for the velocity and total concentration are, to a good approximation, self-similar and show good agreement with DNS results. We observe an off-axis peak for the total variance, similar to that observed in the evolution of a passive scalar. The droplet size distribution from the LES showed excellent agreement with both experimental data and the 1D ODE model discussed in Chapter 5. Additionally, LES is able to quantify new properties of the size distribution generated due to the inherent variability of turbulence. We quantify the radial profiles of the mean and variance of the characteristic diameter, total area available for surface reactions, and the normalized breakup source terms. In accordance with numerous experiments, we observe that the Sauter mean diameter, defined as the volume to surface area ratio of the distribution, decreases with increasing Weber number. This can be attributed to increased breakup of larger droplets resulting in a steeper slope in the small-scale size range of the droplet size distribution. Although demonstrating a significant effect on the averaged droplet size distribution, the Weber number has minimal effect

on the radial profiles of the normalized standard deviations of key quantities.

Chapter 7

Size Based Differential Droplet Dispersion

In the last chapter, we showed that the axial decay of the individual concentration plumes were size dependent. While the total concentration field showed a self-similar collapse when plotted as a function of $r/r_{1/2}$, we noticed that the radial profiles of the different droplet plumes exhibited different widths (see 7.1). This effect was suspected to be caused by the particle trajectory crossing effect, that occurs due to the finite particle rise velocity.

We briefly review the trajectory crossing effect, proposed by Csanady[24], in section 7.1. We further discuss the effect of trajectory crossing on the turbulent diffusion coefficients of different droplet sizes. Using the theory developed by Csanady[24] we quantify the effect of trajectory crossing on the profiles of droplet

concentration and compare it to simulation results in a turbulent jet in section 7.2. Conclusions are presented in section 7.3.

7.1 Particle Trajectory Crossing Effect

Particle motion is governed by an interplay of the turbulent flow field, inertial and buoyancy effects. When particle trajectories under the influence of gravity cross the trajectories of fluid elements, the particles are transported from one region of a highly correlated flow (e.g. an eddy) to another region (or another eddy). Heavy particles, owing to their finite free fall (or rise) velocity can move from one eddy to another faster than the average eddy decay rate[116]. This results in particles losing their velocity correlation more rapidly than fluid elements. As the particle correlation time is directly related to the dispersion coefficient[102], their dispersion is also reduced. The dispersion of light (smaller) particles however, is predominantly controlled by the turbulent flow field.

Taylor[102] derived the well known equation for the fluid dispersion coefficient ($D_{f,ij}$) in a stationary homogeneous turbulent flow in terms of the Lagrangian velocity $w_i'(t)$

$$D_{f,ij}(t) = w'^2 \int_0^t R_{ij}(s)ds, \tag{7.1}$$

where w'^2 is the turbulent r.m.s velocity and $R_{ij}(s)$ is the Lagrangian fluid-velocity autocorrelation function given by,

$$R_{ij}(s) = \frac{\overline{w_i'(t)w_j'(t+s)}}{\overline{w'^2}}. \tag{7.2}$$

The indices $i, j = 1, 2, 3$ represent the coordinate directions. Csanady[24] extended the theory of dispersion of fluid points proposed by Taylor[102] to particles. He reasoned that particles moving rapidly across the fluid will experience the fluid's Eulerian rather than Lagrangian velocity correlation function. The effect of the rise (or drift) velocity can then be obtained by substituting the Eulerian correlation function into Taylor's relation (equation (7.1)). By considering the most probable shape of the correlation isoclines for the Lagrangian and Eulerian correlation coefficients he was able to construct two relations for the particle dispersion coefficients parallel to (longitudinal) and normal to (lateral) the direction of the rise velocity :

$$\frac{D_{i,L}}{D_{f,L}} = \left(1 + \frac{Cw_{r,i}^2}{w'^2}\right)^{-1/2}, \tag{7.3}$$

$$\frac{D_{i,T}}{D_{f,T}} = \left(1 + \frac{4Cw_{r,i}^2}{w'^2}\right)^{-1/2}, \tag{7.4}$$

where $D_{i,L}$, $D_{f,L}$, $D_{i,T}$, $D_{f,T}$ are the longitudinal and transverse particle and fluid dispersion coefficients, $w_{r,i}$ is the particle rise velocity (in the vertical direction), $C = w'T_L/L_E$ relates the Lagrangian timescale T_L to the Eulerian length scale L_E and w' is the axial turbulent fluctuation velocity (in the direc-

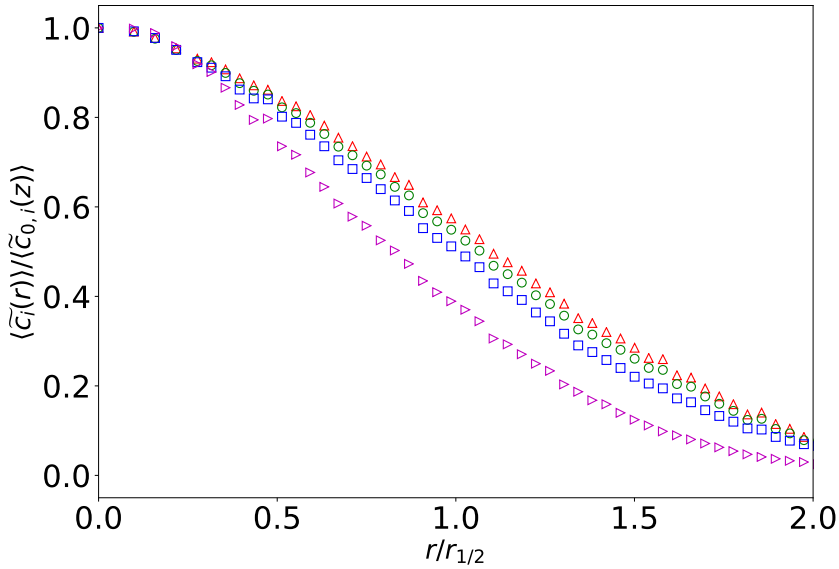

Figure 7.1: Normalized radial concentration profiles for different droplet sizes at $z/D_J = 160$. The symbols are $d = 14\ \mu m$ (△), $d = 236\ \mu m$ (○), $d = 730\ \mu m$ (□) and $d = 3\ mm$ (▷).

tion of the rise velocity). We shall use equation (7.3) to quantify the effect of trajectory crossing in the next section.

7.2 Results

We use the simulation setup and parameters presented in Chapter 6. We plot the concentration profiles as a function of radial distance for the different droplet plumes in Figure 7.1. The width of the profile of the largest droplet size ($d = 3000\mu m$) is much narrower than the smaller droplet sizes. The width is clearly size dependent with the larger droplet plumes being narrower.

The half-width of the concentration profile can be defined similarly to the velocity profile as :

$$\langle \tilde{c}_i(z, r_{1/2,i}(z), 0) \rangle = \frac{1}{2} \langle \tilde{c}_{0,i}(z) \rangle, \tag{7.5}$$

where c_i is the concentration of oil in the ith bin and $r_{1/2,i}$ is the half width of the concentration of a droplet with diameter d_i. The growth of the half width of the concentration is linear similar to the velocity field. We can obtain the growth rate S_i by finding the slope of the line fit through the half-width data. We can see from Figure 7.2 that this growth rate is size dependent, with the larger droplet sizes having a much reduced growth rate. The smaller droplet sizes tend to follow the fluid whereas the dispersion of the larger droplet sizes seem to be modified. This is due to the trajectory crossing effect described in section 7.1. We can calculate the reduction in the transverse particle diffusion coefficient, compared to the fluid using equation (7.3).

We plot the axial evolution of ratio of the transverse diffusion coefficient defined in equation (7.3) in Figure 7.3. The rise velocity of the droplet has been previously defined in equation (2.22) and we use the axial turbulent velocity from the LES. We can see that the ratio is near unity for the smaller droplets ($d = 14\ \mu m$ and $d = 236\ \mu m$), whereas for the larger droplet sizes the dispersion coefficient is suppressed due to trajectory crossing effects.

In Chapter 5 we derived a similarity solution for the concentration :

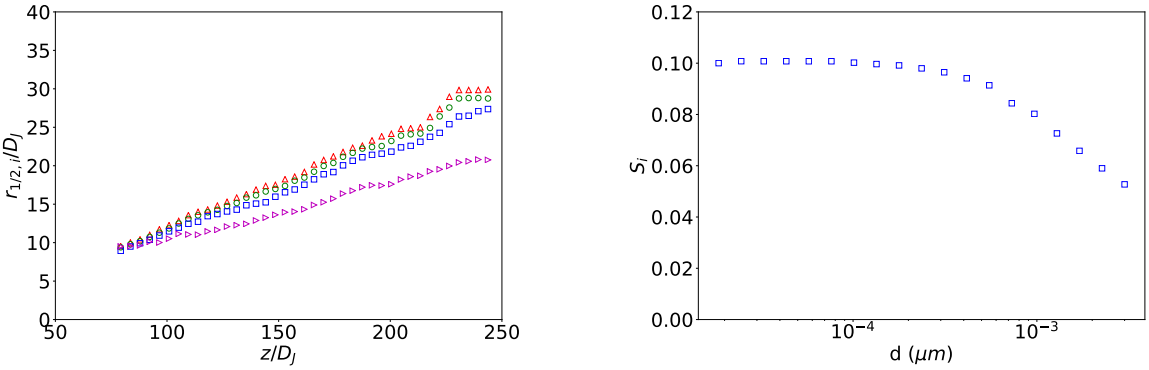

(a) Concentration Half Width **(b)** Spread Rate

Figure 7.2: (a) Evolution of concentration half width as a function of downstream distance from the nozzle. The symbols are $d = 14\ \mu m$ (△), $d = 236\ \mu m$ (○), $d = 730\ \mu m$ (□) and $d = 3\ mm$ (▷), (b) Spread rate of different droplet plumes as a function of diameter.

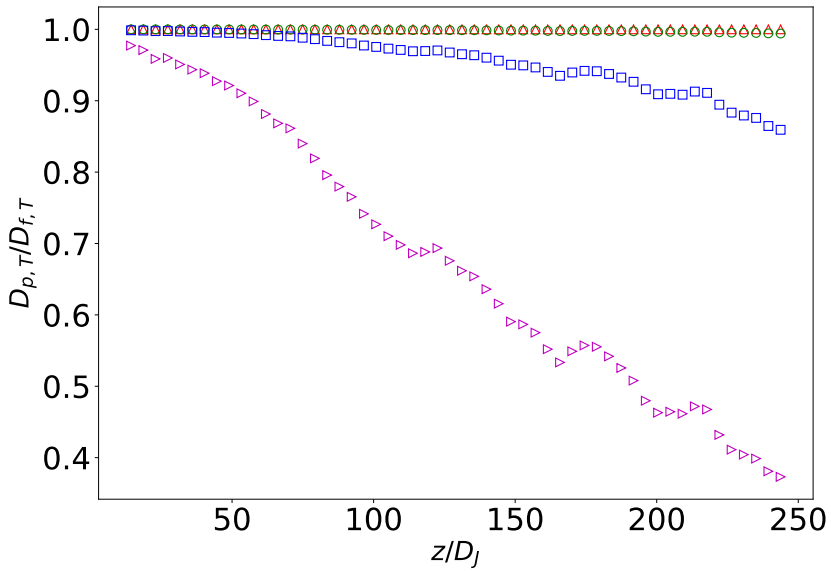

Figure 7.3: Ratio of transverse particle to fluid dispersion coefficient calculated using equation (7.3). The symbols are $d = 14\ \mu m$ (△), $d = 236\ \mu m$ (○), $d = 730\ \mu m$ (□) and $d = 3\ mm$ (▷).

$$c(r,z) = \frac{c_0(z)}{(1+\alpha^2\eta^2)^{2Sc_T}}, \tag{7.6}$$

where $\alpha^2 = (\sqrt{2}-1)/S^2$, Sc_T is the turbulent Schmidt number and $\eta = r/z$ is the similarity variable. One can account for the effect of trajectory crossing in the model by allowing the turbulent Schmidt number to be size dependent. The turbulent Schmidt number is defined as the ratio of the diffusion coefficients of the fluid to that of the particle.

$$Sc_T(z,d_i) = D_{f,T}/D_{i,T} \tag{7.7}$$

We can calculate the average of equation (7.3) along axial distance in order to obtain a size dependent Schmidt number $\langle Sc_T(d_i)\rangle_z$. Substituting $r = r_{1/2,i}$ or $\eta = S_{d,i}$, $c_i(r,z)/c_{0,i}(z) = 0.5$ in equation (7.6) we can the modified spread rate as:

$$0.5 = \frac{1}{\left(1+S_{d,i}^2\right)^{2\langle Sc_T(d_i)\rangle_z}}, \tag{7.8}$$

Simplifying equation (7.8) to solve for the growth rate we obtain:

$$S_{d,i}^2 = \frac{1}{\alpha^2}\left[\exp\left(\frac{0.5\log 2}{\langle Sc_T(d_i)\rangle_z}\right) - 1\right]. \tag{7.9}$$

The spread rate calculated using the modified Schmidt number and the de-

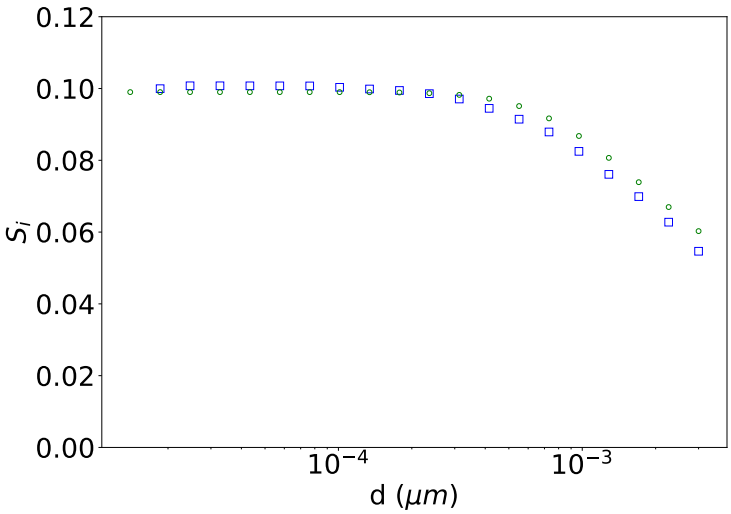

Figure 7.4: Spread rate calculated using LES concentration field (□) and using modified Schmidt number (○) defined by equation (7.3).

rived similarity profile can be validated with that calculated directly from the concentration profiles of the various droplet plumes. We can see from Figure 7.4 that the modified Schmidt number approach accurately predicts the spread rate of the individual droplet plumes.

7.3 Conclusions

The radial profiles of droplet concentrations are size dependent, with larger droplet diameter plumes having a narrower width. We hypothesize this effect to be due to particle trajectory crossing that occurs due to the finite rise velocity of the particle. We observe that the dispersion of larger droplets, $d > 300\mu m$ is suppressed due to trajectory crossing effects resulting in narrower concen-

tration profiles for the larger droplet sizes. This effect can be modelled in a turbulent jet by allowing the Schmidt number in the concentration similarity solution to be size dependent. To our knowledge this is the first time the trajectory crossing effect was shown in an Eulerian-Eulerian simulation with the fast Eulerian method.

Chapter 8

Summary and Future Work

Studying the evolution of polydisperse turbulent flow systems is a challenging task that requires an understanding of complex mechanisms governing particle behaviour. Numerous factors affect particle dynamics such as dispersed phase volume fraction, particle shape, breakup and coalescence. Resolving the dynamics of each particle using Direct Numerical Simulations (DNS) for large systems with many particles in practical applications is computationally intractable, and a modelling approach is needed. This thesis works towards building such an approach, by developing a large eddy simulation model coupled with population balance equations including the effects of droplet breakup to study the evolution of polydisperse droplets in turbulent flows.

There have been a large number of models developed over the years to study droplet breakup in a turbulent system. However, there is a lack of a consistent

framework in developing models valid for the entire spectrum of turbulence. As existing models use scalings only valid for the inertial range, they are unable to model viscous-range droplets accurately and rely on adjustable model constants that needed to be fit to experimental data often resulting in system dependent parameters. In Chapter 2 we develop a droplet breakup model consistently incorporating the viscous range of turbulence. We use an eddy-droplet collision model based on the kinetic theory of gases. The eddy-droplet fluctuation velocity is modeled using a second order structure function formulated in physical space, incorporating the viscous and inertial range of turbulence. The model only has one dimensionless constant that is fit using a single experiment of breakup of droplets following a plunging breaker impinging on an oil slick. The breakup model is further validated using an experiment with different turbulence properties to test its robustness.

Chapter 3 presents the Large-eddy simulation equations for the velocity and concentration fields. Coupling LES with population balance equations in an Eulerian framework is computationally efficient, while at the same time achieving high modelling accuracy. The LES-PBE model is used in Chapter 4 to study a crude oil jet in crossflow as a surrogate oil spill model. The model effectively predicts the averaged droplet size distribution and shows good agreement with experimental data. Additionally LES allow us to study the variability of key quantities related to the size distribution that arises due to the

underlying intermittency and variability of the turbulence. We find that the probability distribution functions of key quantities such as the mean diameter and the total water/oil interfacial area is non-Gaussian with high variation with respect to the mean at different plume locations.

Multiphase jet flows are characterized by a large separation of scales ranging from a few hundred microns (droplet scale), to the order of millimeters (nozzle scale), and up to meters (jet far field or plume). In Chapter 5 we develop a hybrid ODE-LES approach, where the near nozzle region of the jet is replaced by a 1D population dynamics model including breakup due to turbulence at scales smaller than what can be resolved by the coarse LES. In Chapter 6 we present two simulations of polydisperse oil droplets injected at the centerline of a turbulent jet at two distinct Weber numbers. We compare the droplet size distributions to experiments and obtain good agreement. Droplet breakup modifies the rate of decay of the axial concentration in the near nozzle region and the subsequent downsteam evolution of the centerline concentration of the individual droplet plumes depends on size and Weber number. We quantify the radial profiles of the mean and variance of key quantities of the size distribution. We find that although the Weber number has an effect on the Sauter mean diameter and the total interfacial area, the normalized profiles for the variability remain unchanged. In Chapter 7 we find that the dispersion coefficient of droplets is size dependent, with the horizontal dispersion of the

larger droplets being suppressed due to trajectory crossing effects. We model this effect by considering a size dependent Schmidt number for the similarity solution of the concentration field.

The results demonstrate that developing a breakup model by incorporating the entire spectrum of turbulence reduces the number of model constants required and can be used to model breakup of droplets in the viscous range of turbulence. The LES model is effective in simulating polydisperse dispersions with good accuracy (with as few as 15 bins), thereby saving on the high computational cost associated with Lagrangian methods. The suppression of transverse diffusion due to trajectory crossing effects was captured in the Eulerian description without any explicit modelling for the dispersion coefficient. Through this study we demonstrated that large-eddy simulations coupled with population balance equation is an effective tool to model polydisperse droplets in a turbulent flow.

8.1 Directions for Future Work

While this thesis presents progress in modelling polydisperse turbulent systems using large-eddy simulations, additional complexities can be incorporated to increase the scope and generality of the model. Followup studies are required to explore in more detail various relevant aspects such as the effects

of different breakup probability models ($\beta(d_i, d_j)$), the effects of changing grid resolution in LES, the possible effects of various subgrid-scale models for the momentum and scalar fluxes, and other possible extensions such as combining with Lagrangian models for the subgrid-scale velocity gradient fluctuations[43].

An important question that needs to be addressed is the scaling followed by the droplet size distribution in different size regimes. A common demarcation for the droplet size spectrum used in the literature is the Hinze scale, determined by the balance of inertial and capillary forces. In the context of bubble breakup under breaking waves, it has been shown through dimensional analysis that the number density for bubbles larger than the Hinze scale is proportional to $d^{-10/3}$, where d is the size of the bubble. The scaling for sub-Hinze scale droplets is still shrouded in some ambiguity. The daughter probability distribution function important is important in determining the final shape of the distribution especially for sub-Hinze scale droplets. There have been recent efforts to develop a probability model informed by experimental data[82] for bubble breakup. In general, the size spectrum for droplets and bubbles can be different and needs to be studied using a generalized framework that can capture different effects.

In the droplet breakup frequency model developed in Chapter 2, there is scope for improvement by using better models for the number of eddies and using a smooth cut-off for the largest eddy contributing to the breakup (instead

of the sharp cut-off used here). The breakup frequency of chapter 2 grows as a function of droplet size. This is supported through single droplet experiments which found that the frequency of breakup grew monotonically with droplet size[44]. However, for bubble breakup the opposite effect is observed for bubbles larger than the Hinze scale where the breakup frequency scales as $d^{-2/3}$. Controlled experiments or single droplet/bubble simulations are needed in order to address this issue.

To consider large volume fraction cases, droplet coalescence must be included. This can be incorporated in the current framework by using a filtered volume fraction, $\tilde{\alpha}$ in the momentum and mass equations of the fluid. Coalescence kernels can be added as source terms to the concentration equation, with the population balance equation solved either using a moving-pivot method or a moment method. To relax the limitation on the Stokes number, one can recast the equations into a two-fluid formulation where equations are solved for the each droplet velocity.

Appendix A

Empirical Modelling of the Breakup Frequency Integral

In this section we discuss the fit for the integral in the equation for the breakup frequency derived in Chapter 2

$$g_f(Re, Oh, \Gamma) = \int_0^1 r_e^{-11/3}(r_e+1)^2 \left(1+\left(\frac{r_e Re}{\gamma_2}\right)^{-2}\right)^{-1/3} \Omega(Oh, Re, \Gamma; r_e) dr_e. \quad \textbf{(A.1)}$$

As it would be computationally intensive to evaluate an integral at every grid point for every timestep we develop an empirical form of the integral as a function of the two nondimensional parameters Re and Oh, for discrete values of Γ. We begin by plotting the integral g_f for a wide range of Reynolds Re and Ohnesorge Oh numbers for a fixed value of $\Gamma = 10.5$. This is shown in figure

A.1 as the symbols for different Oh numbers. The value of Γ is chosen based on the physical properties of the oil in Murphy et al.[72]. We can see that we have a power law behaviour for higher Re with a sharp cutoff for the small Re. The cut-off location is a function of the Ohnesorge (Oh) number. This suggests that we could fit g_f using two power laws to capture the two extremes. The fit equation can be written as

$$G(Re_i, Oh_i) = ax^b + cx^d - e, \tag{A.2}$$

where $G = \log_{10}(g_f)$, $x = \log_{10}(Re)$, and a, b, c, d, e are functions of Oh. We use Matlab's curve fitting toolbox to carry out the fitting procedure. The toolbox uses a Levenberg-Marquardt algorithm to provide the best fit for the data. We find that the coefficient b can be fixed at $b = 0.45$. The other coefficients can be expressed as functions of the Ohnesorge number using the following fits as a function of $y = Oh$:

$$\begin{gathered} a(y) = a_1 \exp(-a_2 y) + a_3 \exp(-a_4 y) \\ b = 0.45 \\ log_{10}[-c(y)] = \frac{c_1 y^{-c_2}}{1 + c_3 y^{c_4}} \\ d(y) = -\frac{d_1 y^{-d_2}}{1 + d_3 y^{-d_4}} \\ \log_{10}[e(y)] = e_1 \exp(-e_2 \log_{10}(y+1)) + e_3 \exp(-e_4 \log_{10}(y+1)) \end{gathered} \tag{A.3}$$

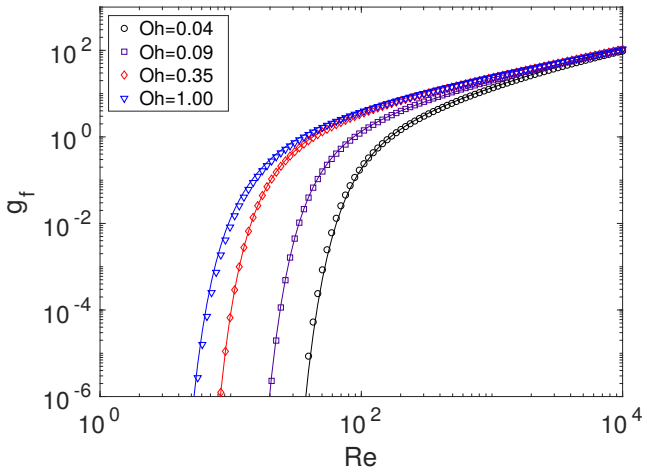

Figure A.1: Scaled breakup frequency as a function of Reynolds number for different Ohnesorge numbers. The fit is represented by the dashed lines whereas the numerically computed integral are the various symbols for $\Gamma = 10.5$.

The coefficients in (A.3) for the particular value of Γ chosen, are given in table A.1 for $\Gamma = 10.5$ and in table A.2 for $\Gamma = 5.45$. The fit is valid for droplet Reynolds number less than 10^4 and for $0.006 \leq Oh \leq 2$. We numerically evaluate the integral in ($A.1$) and compare it with by evaluating the algebraic fit from ($A.3$) in figure $A.1$ for four Oh numbers. The fit is plotted using the dashed lines of different color, while the numerically evaluated integral is represented by the symbols. We see that we have good agreement in the parameter range considered.

We can use the same methodology for a different value of Γ. As an example, we show in figure $A.2$ the fit for the breakup integral for $\Gamma = 5.45$, based on the oil properties from Johansen et al.[42]. We see that we can obtain a good fit for different values of Γ. The coefficients for intermediate Γ values can be obtained

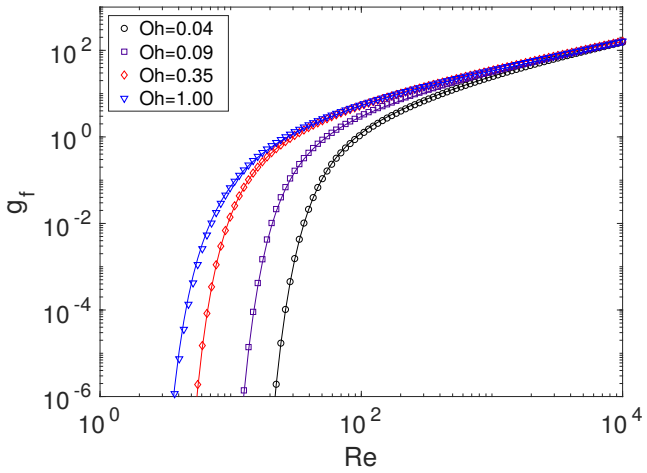

Figure A.2: Scaled breakup frequency as a function of Reynolds number for different Ohnesorge numbers. The fit is represented by the dashed lines whereas the numerically computed integral are the various symbols for $\Gamma = 5.45$.

Variable	Coefficients			
x_k	$k=1$	$k=2$	$k=3$	$k=4$
a	2.374	19.88	2.788	0.07416
c	1.41	0.245	5.178	0.83
d	5.313	0.4541	0.4981	0.4219
e	0.415	41.09	0.5088	0.4604

Table A.1: $\Gamma = 10.5$.

by interpolating the function $G(Oh_i, Re_i)$ between the two cases. For example, to obtain g_f for $\Gamma = 8$ we first linearly interpolate G from $\Gamma_1 = 5.45$ and $\Gamma_2 = 10.5$ as,

$$G(Re_i, Oh_i; \Gamma) = G(Re_i, Oh_i; \Gamma_1) + \frac{G(Re_i, Oh_i; \Gamma_2) - G(Re_i, Oh_i; \Gamma_1)}{\Gamma_2 - \Gamma_1}(\Gamma - \Gamma_1) \quad \textbf{(A.4)}$$

Variable	Coefficients			
x_k	$k=1$	$k=2$	$k=3$	$k=4$
a	2.392	26.76	2.877	0.1244
c	0.5446	0.3776	12.67	1.462
d	4.172	0.5492	0.5079	0.4879
e	0.4113	55.94	0.5125	0.7182

Table A.2: $\Gamma = 5.45$.

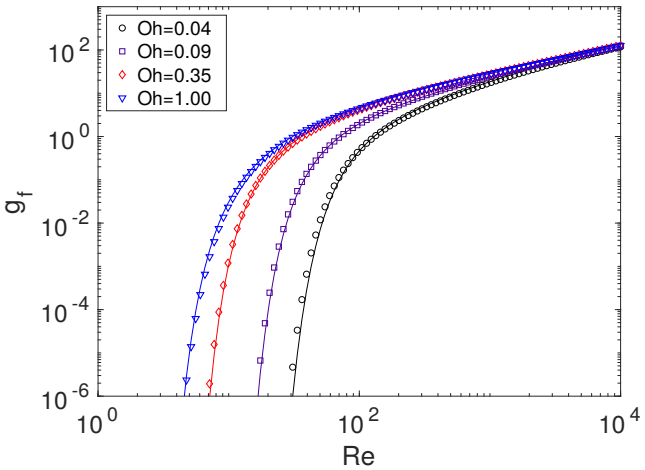

Figure A.3: Scaled breakup frequency as a function of droplet Reynolds number for different Ohnesorge numbers. The fit is represented by the dashed lines computed by interpolating between $\Gamma_1 = 5.45$ and $\Gamma_2 = 10.5$. The symbols represent the numerically computed integral for $\Gamma = 8$.

The integral can then be obtained as $g_f = 10^G$. The results from the interpolation for $Oh = 0.042, 0.09, 0.35$ and 1 are shown in figure $A.3$. We see that even with a simple linear interpolation we can obtain satisfactory results.

In order to quantify the speedup obtained by using the fits compared to the integral, we can calculate the CPU time per simulation time step for each case. We find that the LES with the fits is 60 times faster than an LES with the breakup frequency calculated with the numerical integration of the integral at every grid point and time step. This speedup is more pronounced when the grid is refined. The fits are calculated using vectorized operations that are fast and efficient even on fine grids. The integral on the other hand has to be evaluated at every grid point as the integrand is a function of position.

Bibliography

[1] A. K. Aiyer, D. Yang, M. Chamecki, and C. Meneveau. A population balance model for large eddy simulation of polydisperse droplet evolution. *Journal of Fluid Mechanics*, 878:700–739, 2019. ISSN 0022-1120. doi: 10.1017/jfm.2019.649.

[2] A. K. Aiyer and C. Meneveau. Coupled population balance and large eddy simulation model for polydisperse droplet evolution in a turbulent round jet. *under review for Physical Review Fluids*, pages 1–20, 2020.

[3] J. D. Albertson and M. B. Parlange. Surface length scales and shear stress: Implications for land-atmosphere interaction over complex terrain. *Water Resources Research*, 35(7):2121–2132, 1999. ISSN 00431397. doi: 10.1029/1999WR900094.

[4] V. Alopaeus, J. Koskinen, K. I. Keskinen, and J. Majander. Simulation of the population balances for liquid–liquid systems in a nonideal stirred tank. part 2—parameter fitting and the use of the multiblock model

for dense dispersions. *Chemical Engineering Science*, 57(10):1815 – 1825, 2002. ISSN 0009-2509. doi: https://doi.org/10.1016/S0009-2509(02)00067-2.

[5] S. Apte, M. Gorokhovski, and P. Moin. Les of atomizing spray with stochastic modeling of secondary breakup. *International Journal of Multiphase Flow*, 29(9):1503 – 1522, 2003. ISSN 0301-9322. doi: https://doi.org/10.1016/S0301-9322(03)00111-3.

[6] U. C. Bandara, S. M. Asce, P. D. Yapa, and M. Asce. Bubble Sizes , Breakup , and Coalescence in Deepwater Gas / Oil Plumes. *Journal of Hydraulic Engineering*, 137(7):729–738, 2011. ISSN 0733-9429. doi: 10.1061/(ASCE)HY.1943-7900.0000380.

[7] G. K. Batchelor. Pressure fluctuations in isotropic turbulence. *Proc. Cambr. Phil. Soc.*, 47(July 1950):359–374, 1951.

[8] J. Beyer, H. C. Trannum, T. Bakke, P. V. Hodson, and T. K. Collier. Environmental effects of the deepwater horizon oil spill: A review. *Marine Pollution Bulletin*, 110(1):28 – 51, 2016. ISSN 0025-326X. doi: https://doi.org/10.1016/j.marpolbul.2016.06.027.

[9] M. BINI and W. P. JONES. Large-eddy simulation of particle-laden turbulent flows. *Journal of Fluid Mechanics*, 614:207–252, 2008. doi: 10.1017/S0022112008003443.

[10] E. Bou-Zeid, C. Meneveau, and M. Parlange. A scale-dependent Lagrangian dynamic model for large eddy simulation of complex turbulent flows. *Physics of Fluids*, 17(2):1–18, 2005. ISSN 10706631. doi: 10.1063/1.1839152.

[11] P. J. Brandvik, Ø. Johansen, F. Leirvik, U. Farooq, and P. S. Daling. Droplet breakup in subsurface oil releases - Part 1: Experimental study of droplet breakup and effectiveness of dispersant injection. *Marine Pollution Bulletin*, 73(1):319–326, 2013. ISSN 0025326X. doi: 10.1016/j.marpolbul.2013.05.020.

[12] R. V. Calabrese, C. Y. Wang, and N. P. Bryner. Drop breakup in turbulent stirred tank contactors. Part I: Effect of Dispersed-Phase Viscosity. *AIChE Journal*, 32(4):677–681, 1986. ISSN 15475905. doi: 10.1002/aic.690320418.

[13] M. Calaf, C. Meneveau, and J. Meyers. Large eddy simulation study of fully developed wind-turbine array boundary layers. *Physics of Fluids*, 22(1):015110, 2010. doi: 10.1063/1.3291077.

[14] M. Chamecki, C. Meneveau, and M. B. Parlange. A hybrid spectral/finite-volume algorithm for large-eddy simulation of scalars in the atmospheric boundary layer. *Boundary-Layer Meteorology*, 128(3):473–484, 2008. ISSN 00068314. doi: 10.1007/s10546-008-9302-1.

[15] B. W. H. R. Chan, M. S. Dodd, and P. L. Johnson. Formation and dynamics of bubbles in breaking waves : Part II . The evolution of the bubble size distribution and breakup / coalescence statistics. 2018.

[16] W. H. R. Chan, M. S. Dodd, J. Urzay, A. Mani, and P. Moin. On the development of a subgrid-scale model for the generation of micro-bubbles from impacting liquid surfaces. *Centre for Turbulence Research*, pages 149–162, 2016.

[17] E. Chatzi and M. L. James. Analysis of Interactions for Liquid—Liquid Dispersions in Agitated Vessels. *Industrial and Engineering Chemistry Research*, 26(11):2263–2267, 1987. ISSN 15205045. doi: 10.1021/ie00071a016.

[18] B. Chen, D. Yang, C. Meneveau, and M. Chamecki. Numerical study of the effects of chemical dispersant on oil transport from an idealized underwater blowout. *Phys. Rev. Fluids*, 3:083801, Aug 2018. doi: 10.1103/PhysRevFluids.3.083801.

[19] B. Chen, D. Yang, C. Meneveau, and M. Chamecki. ENDLESS: An extended nonperiodic domain large-eddy simulation approach for scalar plumes. *Ocean Modelling*, 101:121–132, 2016. ISSN 14635003. doi: 10.1016/j.ocemod.2016.04.003.

[20] S. Chester, C. Meneveau, and M. B. Parlange. Modeling turbulent flow

over fractal trees with renormalized numerical simulation. *Journal of Computational Physics*, 225(1):427 – 448, 2007. ISSN 0021-9991. doi: https://doi.org/10.1016/j.jcp.2006.12.009.

[21] L. P. Chua and R. A. Antonia. Turbulent Prandtl number in a circular jet. *International Journal of Heat and Mass Transfer*, 33(2):331–339, 1990. ISSN 00179310. doi: 10.1016/0017-9310(90)90102-Z.

[22] L. Cortelezzi and A. R. Karagozian. On the formation of the counter-rotating vortex pair in transverse jets. *Journal of Fluid Mechanics*, 446: 347–373, 2001. ISSN 00221120. doi: 10.1017/S0022112001005894.

[23] C. A. Coulaloglou and L. L. Tavlarides. Description of interaction processes in agitated liquid-liquid dispersions. *Chemical Engineering Science*, 32(11):1289–1297, 1977. ISSN 00092509. doi: 10.1016/0009-2509(77)85023-9.

[24] G. T. Csanady. Turbulent Diffusion of Heavy Particles in the Atmosphere. *Journal of the Atmospheric Sciences*, 20(3):201–208, 05 1963. ISSN 0022-4928. doi: 10.1175/1520-0469(1963)020⟨0201:TDOHPI⟩2.0.CO;2.

[25] G. B. Deane and M. D. Stokes. Air Entrainment Processes and Bubble Size Distributions in the Surf Zone. *Journal of Physical Oceanography*, 29(7):1393–1403, 07 1999. ISSN 0022-3670. doi: 10.1175/1520-0485(1999)029⟨1393:AEPABS⟩2.0.CO;2.

[26] P. B. Dubovskii, V. A. Galkin, and I. W. Stewart. Exact solutions for the coagulation-fragmentation equation. *Journal of Physics A: Mathematical and General*, 25(18):4737–4744, sep 1992. doi: 10.1088/0305-4470/25/18/009.

[27] C. D. Eastwood, L. Armi, and J. C. Lasheras. The breakup of immiscible fluids in turbulent flows. *Journal of Fluid Mechanics*, 502:309–333, 2004. ISSN 0022-1120. doi: 10.1017/S0022112003007730.

[28] S. Elghobashi. On predicting particle-laden turbulent flows. *Applied Scientific Research*, 52:309–329, 1994. doi: 10.1007/BF00936835.

[29] B. Enderle, B. Rauch, F. Grimm, G. Eckel, and M. Aigner. Non-intrusive uncertainty quantification in the simulation of turbulent spray combustion using polynomial chaos expansion: A case study. *Combustion and Flame*, 213:26 – 38, 2020. ISSN 0010-2180. doi: https://doi.org/10.1016/j.combustflame.2019.11.021.

[30] A. Ferrante and S. Elghobashi. On the physical mechanisms of two-way coupling in particle-laden isotropic turbulence. *Physics of Fluids*, 15(2):315–329, 2003. doi: 10.1063/1.1532731.

[31] J. Ferry and S. Balachandar. A fast Eulerian method for disperse two-phase flow. *International Journal of Multiphase Flow*, 27(7):1199–1226, 2001. ISSN 03019322. doi: 10.1016/S0301-9322(00)00069-0.

[32] P. H. Gaskell and A. K. C. Lau. Curvature compensated convective transport: SMART, A new boundedness preserving transport algorithm. *International Journal for Numerical Methods in Fluids*, 8(6):617–641, 1988. ISSN 10970363. doi: 10.1002/fld.1650080602.

[33] M. Germano. Turbulence: the filtering approach. *Journal of Fluid Mechanics*, 238:325–336, 1992. doi: 10.1017/S0022112092001733.

[34] F. Ghasempour, R. Andersson, and B. Andersson. Multidimensional turbulence spectra – statistical analysis of turbulent vortices. *Applied Mathematical Modelling*, 38(17):4226 – 4237, 2014. ISSN 0307-904X. doi: https://doi.org/10.1016/j.apm.2014.03.003.

[35] P. González-Tello, F. Camacho, J. Vicaria, and P. González. A modified nukiyama–tanasawa distribution function and a rosin–rammler model for the particle-size-distribution analysis. *Powder Technology*, 186(3): 278 – 281, 2008. ISSN 0032-5910. doi: https://doi.org/10.1016/j.powtec.2007.12.011.

[36] B. Gopalan, E. Malkiel, and J. Katz. Experimental investigation of turbulent diffusion of slightly buoyant droplets in locally isotropic turbulence. *Phys. Fluids*, 20(9):095102, 2008. doi: 10.1063/1.2969470.

[37] R. P. Hesketh, T. W. Fraser Russell, and A. W. Etchells. Bubble size

in horizontal pipelines. *AIChE Journal*, 33(4):663–667, 1987. ISSN 15475905. doi: 10.1002/aic.690330414.

[38] J. O. Hinze. Fundamentals of the hydrodynamic mechanism of splitting in dispersion processes. *AlChE J.*, 1(3):289–295, 9 1955. ISSN 1547-5905. doi: 10.1002/aic.690010303.

[39] H. Hulburt and S. Katz. Some problems in particle technology. *Chemical Engineering Science*, 19(8):555–574, 1964. ISSN 00092509. doi: 10.1016/0009-2509(64)85047-8.

[40] H. J. Hussein, S. P. Capp, and W. K. George. Velocity measurements in a high-Reynolds number, momentum-conserving, axisymmetric, turbulent jet. *J. Fluid Mech.*, 258(1994):31–75, 1994.

[41] A. L. Igel and S. C. van den Heever. The Importance of the Shape of Cloud Droplet Size Distributions in Shallow Cumulus Clouds. Part I: Bin Microphysics Simulations. *Journal of the Atmospheric Sciences*, pages 15–0382, 2016. ISSN 0022-4928. doi: 10.1175/JAS-D-15-0382.1.

[42] Ø. Johansen, P. J. Brandvik, and U. Farooq. Droplet breakup in subsea oil releases - Part 2: Predictions of droplet size distributions with and without injection of chemical dispersants. *Marine Pollution Bulletin*, 73 (1):327–335, 2013. ISSN 0025326X. doi: 10.1016/j.marpolbul.2013.04.012.

[43] P. Johnson and C. Meneveau. Predicting viscous-range velocity gradient dynamics in large-eddy simulations of turbulence. *Journal of Fluid Mechanics*, 837:80–114, 2018.

[44] M. Karimi and R. Andersson. An exploratory study on fluid particles breakup rate models for the entire spectrum of turbulent energy. *Chemical Engineering Science*, 192:850–863, 2018. ISSN 00092509. doi: 10.1016/j.ces.2018.08.016.

[45] M. Karimi and R. Andersson. Stochastic simulation of droplet breakup in turbulence. *Chemical Engineering Journal*, 380(June 2019):122502, 2020. ISSN 13858947. doi: 10.1016/j.cej.2019.122502.

[46] A. Kastengren, J. Ilavsky, J. P. Viera, R. Payri, D. J. Duke, A. Swantek, F. Z. Tilocco, N. Sovis, and C. F. Powell. Measurements of droplet size in shear-driven atomization using ultra-small angle x-ray scattering. *International Journal of Multiphase Flow*, 92:131–139, 2017. ISSN 03019322. doi: 10.1016/j.ijmultiphaseflow.2017.03.005.

[47] I. M. Kennedy and M. H. Moody. Particle dispersion in a turbulent round jet. *Experimental Thermal and Fluid Science*, 18(1):11–26, 1998. ISSN 08941777. doi: 10.1016/S0894-1777(98)10009-2.

[48] J. Kleissl, V. Kumar, C. Meneveau, and M. B. Parlange. Numerical study of dynamic smagorinsky models in large-eddy simulation of the atmo-

spheric boundary layer: Validation in stable and unstable conditions. *Water Resources Research*, 42(6), 2006. doi: 10.1029/2005WR004685.

[49] A. N. Kolmogorov. On the breakage of drops in a turbulent flow. *Dokl. Akad. Nauk SSSR*, 66:825–828, 1949.

[50] M. Konno, M. Aoki, and S. Saito. Scale effect on breakup process in liquid-liquid agitated tanks. *Journal of Chemical Engineering of Japan*, 16:312–319, 1982.

[51] J. Kumar, M. Peglow, G. Warnecke, S. Heinrich, and L. Mörl. Improved accuracy and convergence of discretized population balance for aggregation: The cell average technique. *Chemical Engineering Science*, 61(10): 3327–3342, 2006. ISSN 00092509. doi: 10.1016/j.ces.2005.12.014.

[52] J. Kumar, M. Peglow, G. Warnecke, S. Heinrich, and L. Mörl. Improved accuracy and convergence of discretized population balance for aggregation: The cell average technique. *Chemical Engineering Science*, 61(10): 3327 – 3342, 2006. ISSN 0009-2509. doi: https://doi.org/10.1016/j.ces.2005.12.014.

[53] S. Kumar and D. Ramkrishna. On the solution of population balance equations by discretization—i. a fixed pivot technique. *Chemical Engineering Science*, 51(8):1311 – 1332, 1996. ISSN 0009-2509. doi: https://doi.org/10.1016/0009-2509(96)88489-2.

[54] J. C. Lasheras, C. Eastwood, C. Martínez-Bazán, and J. L. Montaes. A review of statistical models for the break-up an immiscible fluid immersed into a fully developed turbulent flow. *International Journal of Multiphase Flow*, 28(2):247–278, 2002. ISSN 03019322. doi: 10.1016/S0301-9322(01)00046-5.

[55] F. Laurent, A. Vié, C. Chalons, R. Fox, and M. Massot. A hierarchy of Eulerian models for trajectory crossing in particle-laden turbulent flows over a wide range of Stokes numbers. In C. for Turbulence Research, editor, *Annual Research Briefs 2012*, pages 193–204. Center for Turbulence Research - Stanford University, January 2013. http://ctr.stanford.edu/ResBriefs/2012/.

[56] A. W. Law. Velocity and concentration distributions of round and plane turbulent jets. *Journal of Engineering Mathematics*, 56(1):69–78, 2006. ISSN 00220833. doi: 10.1007/s10665-006-9037-2.

[57] K. Lee and T. Matsoukas. Simultaneous coagulation and break-up using constant-n monte carlo. *Powder Technology*, 110(1):82 – 89, 2000. ISSN 0032-5910. doi: https://doi.org/10.1016/S0032-5910(99)00270-3.

[58] F. Lehr and D. Mewes. A transport equation for the interfacial area density applied to bubble columns. *Chemical Engineering Science*, 56: 1159–1166, 1999.

[59] F. Lehr, M. Millies, and D. Mewes. Bubble-size distributions and flow fields in bubble columns. *AIChE Journal*, 48(11):2426–2443, 2002. ISSN 00011541. doi: 10.1002/aic.690481103.

[60] C. Li, J. Miller, J. Wang, S. S. Koley, and J. Katz. Size Distribution and Dispersion of Droplets Generated by Impingement of Breaking Waves on Oil Slicks. *Journal of Geophysical Research: Oceans*, 122(10):7938–7957, 2017. ISSN 21699291. doi: 10.1002/2017JC013193.

[61] Y. Liao and D. Lucas. A literature review of theoretical models for drop and bubble breakup in turbulent dispersions. *Chemical Engineering Science*, 64(15):3389–3406, 2009. ISSN 00092509. doi: 10.1016/j.ces.2009.04.026.

[62] J. Liu, J. Xu, G. Wang, M. Yang, and L. Guo. [Study advancement of calpain and apoptosis following cerebral ischemia]. *Sheng wu yi xue gong cheng xue za zhi = Journal of biomedical engineering = Shengwu yixue gongchengxue zazhi*, 26(5):1150–1153, 2009. ISSN 10015515.

[63] Y. G. Liu, L. G. You, W. N. Yang, and F. LIU. On the Size Distribution of Cloud Droplets. *Atmospheric Research*, 35(2-4):201–216, 1995.

[64] C. L. Lubbers, G. Brethouwer, and B. J. Boersma. Simulation of the mixing of a passive scalar in a round turbulent jet. *Fluid Dynamics Research*,

28(3):189–208, 2001. ISSN 01695983. doi: 10.1016/S0169-5983(00)00026-5.

[65] D. L. Marchisio and R. O. Fox. Solution of population balance equations using the direct quadrature method of moments. *Journal of Aerosol Science*, 36(1):43 – 73, 2005. ISSN 0021-8502. doi: https://doi.org/10.1016/j.jaerosci.2004.07.009.

[66] D. L. Marchisio, J. T. Pikturna, R. O. Fox, R. D. Vigil, and A. A. Barresi. Quadrature method of moments for population-balance equations. *AIChE Journal*, 49(5):1266–1276, 2003. doi: 10.1002/aic.690490517.

[67] C. Martínez-Bazán, J. L. Montañés, and J. C. Lasheras. On the breakup of an air bubble injected into a fully developed turbulent flow. Part 1. Breakup frequency. *Journal of Fluid Mechanics*, 401:183–207, 1999. ISSN 00221120. doi: 10.1017/S0022112099006692.

[68] C. Martínez-Bazán, J. Rodríguez-Rodríguez, G. B. Deane, J. L. Montaes, and J. C. Lasheras. Considerations on bubble fragmentation models. *Journal of Fluid Mechanics*, 661:159–177, 10 2010. ISSN 00221120. doi: 10.1017/S0022112010003186.

[69] R. McGraw. Description of aerosol dynamics by the quadrature method of moments. *Aerosol Science and Technology*, 27(2):255–265, 1997. doi: 10.1080/02786829708965471.

[70] R. Mittal, R. Ni, and J. H. Seo. The flow physics of COVID-19. *Journal of Fluid Mechanics*, 894:1–14, 2020. ISSN 14697645. doi: 10.1017/jfm.2020.330.

[71] E. Movahednejad, F. Ommi, and S. M. Hosseinalipour. Prediction of droplet size and velocity distribution in droplet formation region of liquid spray. *Entropy*, 12(6):1484–1498, 2010. ISSN 10994300. doi: 10.3390/e12061484.

[72] D. W. Murphy, X. Xue, K. Sampath, and J. Katz. Crude oil jets in cross-flow: Effects of dispersant concentration on plume behavior. *Journal of Geophysical Research: Oceans*, 121(6):4264–4281, 2016. ISSN 21699291. doi: 10.1002/2015JC011574.

[73] G. Narsimhan, J. P. Gupta, and D. Ramkrishna. A model for transitional breakage probability of droplets in agitated lean liquid-liquid dispersions. *Chemical Engineering Science*, 34(2):257–265, 1979. ISSN 00092509. doi: 10.1016/0009-2509(79)87013-X.

[74] G. Narsimhan, D. Ramkrishna, and J. P. Gupta. Analysis of drop size distributions in lean liquid-liquid dispersions. *AIChE Journal*, 26(6): 991–1000, 1980. ISSN 15475905. doi: 10.1002/aic.690260614.

[75] I. D. Nissanka and P. D. Yapa. Calculation of oil droplet size distribution

in an underwater oil well blowout. *Journal of Hydraulic Research*, 54(3): 307–320, 2016. ISSN 00221686. doi: 10.1080/00221686.2016.1144656.

[76] E. North, E. Adams, Z. Schlag, C. Sherwood, R. He, K. Hyun, and S. Socolofsky. Simulating oil droplet dispersal from the deepwater horizon spill with a lagrangian approach. *Washington DC American Geophysical Union Geophysical Monograph Series*, 195:217–226, 01 2011. doi: 10.1029/2011GM001102.

[77] E. W. North, E. E. Adams, A. E. Thessen, Z. Schlag, R. He, S. A. Socolofsky, S. M. Masutani, and S. D. Peckham. The influence of droplet size and biodegradation on the transport of subsurface oil droplets during the Deepwater Horizon spill: A model sensitivity study. *Environmental Research Letters*, 10(2), 2015. ISSN 17489326. doi: 10.1088/1748-9326/10/2/024016.

[78] N. R. Panchapakesan and J. L. Lumley. Turbulence Measurements in Axisymmetric Jets of Air and Helium. Part 2. Helium Jet. *Journal of Fluid Mechanics*, 246:225–247, 1993. ISSN 14697645. doi: 10.1017/S0022112093000102.

[79] J. Pedel, J. N. Thornock, S. T. Smith, and P. J. Smith. Large eddy simulation of polydisperse particles in turbulent coaxial jets using the direct quadrature method of moments. *International Journal of Multiphase*

Flow, 63:23–38, 2014. ISSN 03019322. doi: 10.1016/j.ijmultiphaseflow.2014.03.002.

[80] S. B. Pope. *Turbulent Flows*, volume 12. 2001. ISBN 9780511840531. doi: 10.1088/0957-0233/12/11/705.

[81] M. J. Prince and H. W. Blanch. Bubble Coalescence and Break-up in Air-Sparged Bubble Columns. *AIChE Journal*, 36(10):1485–1499, 1990. ISSN 15475905. doi: 10.1002/aic.690361004.

[82] Y. Qi, A. U. Mohammad Masuk, and R. Ni. Towards a model of bubble breakup in turbulence through experimental constraints. *International Journal of Multiphase Flow*, page 103397, 2020. ISSN 0301-9322. doi: https://doi.org/10.1016/j.ijmultiphaseflow.2020.103397.

[83] D. Ramkrishna. Chapter 4 - the solution of population balance equations. In D. Ramkrishna, editor, *Population Balances*, pages 117 – 195. Academic Press, San Diego, 2000. ISBN 978-0-12-576970-9. doi: https://doi.org/10.1016/B978-012576970-9/50005-9.

[84] E. Ramudu, R. Gelderloos, D. Yang, C. Meneveau, and A. Gnanadesikan. Large eddy simulation of heat entrainment under arctic sea ice. *Journal of Geophysical Research: Oceans*, 123(1):287–304, 2018. doi: 10.1002/2017JC013267.

[85] A. D. Randolph. A population balance for countable entities. *The Canadian Journal of Chemical Engineering*, 42(6):280–281, 1964. ISSN 1939019X. doi: 10.1002/cjce.5450420612.

[86] S. Kumar and D. Ramakrishna. On the solution of population balance equations by discretization -I. A fixed pivot technique. *Chemical Engineering Science*, 51(8):1311–1332, 1996. ISSN 18657109. doi: 10.1515/zna-1951-0407.

[87] F. Salehi, M. J. Cleary, and A. R. Masri. Population balance equation for turbulent polydispersed inertial droplets and particles. *Journal of Fluid Mechanics*, 831:719–742, 2017. ISSN 0022-1120. doi: 10.1017/jfm.2017.653.

[88] F. Salehi, M. J. Cleary, A. R. Masri, and A. Kronenburg. PDF-PBE modelling of polydisperse inertial particles in a turbulent recirculating flow. *International Journal of Multiphase Flow*, 117:42–52, 2019. ISSN 03019322. doi: 10.1016/j.ijmultiphaseflow.2019.04.028.

[89] F. Salehi, M. J. Cleary, A. R. Masri, and A. Kronenburg. Large eddy simulation of polydispersed inertial particles using two-way coupled PDF-PBE. *International Journal of Heat and Fluid Flow*, 83(March):108585, 2020. ISSN 0142727X. doi: 10.1016/j.ijheatfluidflow.2020.108585.

[90] Y. Sato and K. Yamamoto. Lagrangian measurement of fluid-particle

motion in an isotropic turbulent field. *J. Fluid Mech.*, 175:183–199, 1987. doi: 10.1017/S0022112087000351.

[91] N. Seubert, A. Kronenburg, O. T. Stein, Y. Ge, and M. J. Cleary. Large Eddy Simulation-Probability Density Function modelling of nucleation and condensation of DBP droplets in a turbulent jet. pages 1–8, 2012.

[92] F. Sewerin and S. Rigopoulos. An LES-PBE-PDF approach for modeling particle formation in turbulent reacting flows. *Physics of Fluids*, 29(10), 2017. ISSN 10897666. doi: 10.1063/1.5001343.

[93] R. Skartlien, E. Sollum, and H. Schumann. Droplet size distributions in turbulent emulsions: breakup criteria and surfactant effects from direct numerical simulations. *The Journal of chemical physics*, 139(17):174901, 2013. ISSN 1089-7690. doi: 10.1063/1.4827025.

[94] J. Smagorinsky. General Circulation Experiments With the Primitive Equations. *Monthly Weather Review*, 91(3):99–164, 1963. ISSN 0027-0644. doi: 10.1175/1520-0493(1963)091⟨0099:GCEWTP⟩2.3.CO;2.

[95] M. V. Smoluchowski. Drei Vortrage uber Diffusion, Brownsche Bewegung und Koagulation von Kolloidteilchen. *Zeitschrift fur Physik*, 17: 557–585, 1916.

[96] A. Snegirev, L. A, and T. V. Flame suppression by water sprays: flame-

spray interaction regimes and governing criteria. 07 2010. doi: 10.13140/2.1.4947.5521.

[97] J. Solsvik and H. A. Jakobsen. Development of fluid particle breakup and coalescence closure models for the complete energy spectrum of isotropic turbulence. *Industrial & Engineering Chemistry Research*, 55(5):1449–1460, 2016. doi: 10.1021/acs.iecr.5b04077.

[98] J. Solsvik, P. J. Becker, N. Sheibat-Othman, I. Mohallick, R. Farzad, and H. A. Jakobsen. Viscous Drop Breakage in Liquid–Liquid Stirred Dispersions: Population Balance Modeling. *Journal of Dispersion Science and Technology*, 36(4):577–594, 2015. ISSN 15322351. doi: 10.1080/01932691.2014.910471.

[99] J. Solsvik, S. Maaß, and H. A. Jakobsen. Definition of the Single Drop Breakup Event. *Industrial and Engineering Chemistry Research*, 55(10):2872–2882, 2016. ISSN 15205045. doi: 10.1021/acs.iecr.6b00591.

[100] J. Solsvik, V. T. Skjervold, L. Han, H. Luo, and H. A. Jakobsen. A theoretical study on drop breakup modeling in turbulent flows: The inertial subrange versus the entire spectrum of isotropic turbulence. *Chemical Engineering Science*, 149:249 – 265, 2016. ISSN 0009-2509. doi: https://doi.org/10.1016/j.ces.2016.04.037.

[101] L. K. Su and N. T. Clemens. Planar measurements of the full three-

dimensional scalar dissipation rate in gas-phase turbulent flows. *Experiments in Fluids*, 27(6):507–521, 1999. ISSN 07234864. doi: 10.1007/s003480050375.

[102] G. I. Taylor. Diffusion by continuous movements. *Proceedings of the London Mathematical Society*, s2-20(1):196–212, 1922. doi: 10.1112/plms/s2-20.1.196.

[103] Y. H. Tseng, C. Meneveau, and M. B. Parlange. Modeling flow around bluff bodies and predicting urban dispersion using large eddy simulation. *Environmental Science and Technology*, 40(8):2653–2662, 2006. ISSN 0013936X. doi: 10.1021/es051708m.

[104] C. Tsouris and L. L. Tavlarides. Breakage and coalescence models for drops in turbulent dispersions. *AIChE Journal*, 40(3):395–406, 1994. ISSN 15475905. doi: 10.1002/aic.690400303.

[105] M. Vanni. Approximate population balance equations for aggregation–breakage processes. *Journal of Colloid and Interface Science*, 221 (2):143 – 160, 2000. ISSN 0021-9797. doi: https://doi.org/10.1006/jcis.1999.6571.

[106] T. Wang and J. Wang. Numerical simulations of gas-liquid mass transfer in bubble columns with a CFD-PBM coupled model. *Chemical*

Engineering Science, 62(24):7107–7118, 2007. ISSN 00092509. doi: 10.1016/j.ces.2007.08.033.

[107] T. Wang, J. Wang, and Y. Jin. A novel theoretical breakup kernel function for bubbles/droplets in a turbulent flow. *Chemical Engineering Science*, 58(20):4629–4637, 2003. ISSN 00092509. doi: 10.1016/j.ces.2003.07.009.

[108] M. R. Wells and D. E. Stock. The effects of crossing trajectories on the dispersion of particles in a turbulent flow. *Journal of Fluid Mechanics*, 136:31–62, 1983. doi: 10.1017/S0022112083002049.

[109] F. Wu, Yu-Ting Porté-Agel. Simulation of Turbulent Flow Inside and Above Wind Farms: Model Validation and Layout Effects. *Boundary-Layer Meteorology*, 146(2):181–205, 2013. doi: 10.1007/s10546-012-9757-y.

[110] M. Wulkow, A. Gerstlauer, and U. Nieken. Modeling and simulation of crystallization processes using parsival. *Chemical Engineering Science*, 56(7):2575 – 2588, 2001. ISSN 0009-2509. doi: https://doi.org/10.1016/S0009-2509(00)00432-2. Industrial Crystallisation.

[111] X. Xue and J. Katz. Formation of compound droplets during fragmentation of turbulent buoyant oil jet in water. *Journal of Fluid Mechanics*, 878:98–112, 2019. ISSN 14697645. doi: 10.1017/jfm.2019.645.

[112] D. Yang, C. Meneveau, and L. Shen. Effect of downwind swells on offshore wind energy harvesting – A large-eddy simulation study. *Renewable Energy*, 70:11–23, 10 2014. ISSN 0960-1481. doi: 10.1016/J.RENENE.2014.03.069.

[113] D. Yang, B. Chen, M. Chamecki, and C. Meneveau. Oil plumes and dispersion in Langmuir, upper-ocean turbulence: Large-eddy simulations and K-profile parameterization. *Journal of Geophysical Research C: Oceans*, 120(7):4729–4759, 2015. ISSN 21699291. doi: 10.1002/2014JC010542.

[114] D. Yang, B. Chen, S. A. Socolofsky, M. Chamecki, and C. Meneveau. Large-eddy simulation and parameterization of buoyant plume dynamics in stratified flow. *Journal of Fluid Mechanics*, 794:798–833, 2016. ISSN 14697645. doi: 10.1017/jfm.2016.191.

[115] C. Yuan, F. Laurent, and R. Fox. An extended quadrature method of moments for population balance equations. *Journal of Aerosol Science*, 51:1 – 23, 2012. ISSN 0021-8502. doi: https://doi.org/10.1016/j.jaerosci.2012.04.003.

[116] M. Yudine. Physical considerations on heavy-particle diffusion. volume 6 of *Advances in Geophysics*, pages 185 – 191. Elsevier, 1959. doi: https://doi.org/10.1016/S0065-2687(08)60106-5.

[117] H. Zhao and C. Zheng. A population balance-monte carlo method for particle coagulation in spatially inhomogeneous systems. *Computers Fluids*, 71:196 – 207, 2013. ISSN 0045-7930. doi: https://doi.org/10.1016/j.compfluid.2012.09.025.

[118] L. Zhao, M. C. Boufadel, S. A. Socolofsky, E. Adams, T. King, and K. Lee. Evolution of droplets in subsea oil and gas blowouts: Development and validation of the numerical model VDROP-J. *Mar. Pollut. Bull.*, 83(1): 58 – 69, 2014. ISSN 0025-326X. doi: https://doi.org/10.1016/j.marpolbul.2014.04.020.

[119] L. Zhao, J. Torlapati, M. C. Boufadel, T. King, B. Robinson, and K. Lee. VDROP: A comprehensive model for droplet formation of oils and gases in liquids - Incorporation of the interfacial tension and droplet viscosity. *Chemical Engineering Journal*, 253:93–106, 2014. ISSN 13858947. doi: 10.1016/j.cej.2014.04.082.

[120] L. Zhao, F. Shaffer, B. Robinson, T. King, C. D'Ambrose, Z. Pan, F. Gao, R. S. Miller, R. N. Conmy, and M. C. Boufadel. Underwater oil jet: Hydrodynamics and droplet size distribution. *Chemical Engineering Journal*, 299:292–303, 2016. ISSN 13858947. doi: 10.1016/j.cej.2016.04.061.

[121] R. M. Ziff. New solutions to the fragmentation equation. *Journal of*

BIBLIOGRAPHY

Physics A: Mathematical and General, 24(12):2821–2828, jun 1991. doi: 10.1088/0305-4470/24/12/020.

Vita

Aditya Kandaswamy Aiyer was born in Pune, India in 1993. He was awarded the INSPIRE fellowship by the Govt. of India to pursue Physics in the Birla Institute of Technology and Sciences, Goa. He graduated with a Masters in Physics and a Bachelors degree in Mechanical Engineering in 2016. Prior to joining the graduate program at Johns Hopkins University, Aditya worked as a research assistant at the Tata Institute of Fundamental Research (TIFR) where he studied entrainmnet during cloud formation. He received a M.S.E from Johns Hopkins University in 2019.